An investigation of inclusive charmless semileptonic B meson decays with the Belle detector

Antonio Limosani

Submitted in fulfilment of the requirements

of the degree of Doctor of Philosophy

The School of Physics

The University of Melbourne

August 2004

Abstract

An investigation of inclusive charmless semileptonic B meson decays, $B \to X_u e \nu_e$, at the endpoint of the electron momentum spectrum is presented. This analysis is performed on a sample of 29.4 million $B\overline{B}$ pairs that were produced at the $\Upsilon(4S)$ resonance by the KEKB accelerator and collected by the Belle detector.

An analysis of $B \to X_u e \nu_e$ can be used to measure the magnitude of the Cabibbo-Kobayashi-Maskawa mixing matrix element $|V_{ub}|$. $|V_{ub}|$ is a fundamental parameter in the Standard Model of Particle Physics. It constrains the parameters of the Unitarity Triangle. The Unitarity Triangle underpins the understanding of the phenomenon of CP violation within the Standard Model.

The partial branching fractions to this B meson decay mode are determined in the electron momentum spectrum as measured in the rest frame of the $\Upsilon(4S)$ resonance. These are extrapolated to the full branching fractions using spectral fractions calculated from an analysis of the Belle measured $B \to X_s \gamma$ photon energy spectrum. The analysis to determine the spectral fractions is also presented.

The full branching fractions are used to extract $|V_{ub}|$ in multiple momentum intervals. The $|V_{ub}|$ value of minimal uncertainty is extracted in the momentum interval $(2.0 - 2.6)$ GeV/c and found to be:

$$|V_{ub}| = (4.79 \pm 0.72) \times 10^{-3}.$$

This is to certify that

i. this thesis comprises only my original work towards my PhD,

ii. due acknowledgement has been made of all other material used,

iii. this thesis is less than 100,000 words in length, exclusive of tables, bibliographies and appendices.

Antonio Limosani

Acknowledgements

I would like to thank my parents, Mario and Italia Limosani, my brother, Luigi Limosani and my sister, Maria Limosani, for their unconditional love: you are in everything I do. This thesis is dedicated to them and to the memory of my Uncle John Leggiero, who taught me to be selfless with knowledge.

I thank my colleagues in the Melbourne experimental particle physics group, past and present, for useful discussions, ample humour, and friendship. I offer additional thanks to Jasna Dragic who excelled in these areas. I thank my supervisor Martin Sevior for the opportunity to do research with the Belle experiment, for the overall support and for belief in my ability. I am grateful to Tom Browder for suggesting the topic of research, for providing critical assessment and suggestions, and for always keeping pace. I owe a great debt of gratitude to Patrick Koppenburg for performing the world's best measurement of the $B \to X_s\gamma$ photon energy spectrum and for ommunicating in great detail all aspects therein that were essential to my analysis. Many thanks to Tadao Nozaki whose careful probing, instruction and willingness to understand crucial components of my work deepened my understanding no end. Many withstood my presentations in Belle meetings and then gave important feedback that ensured my progress, none more so than the members of the CKM group and regular attendees, namely Toru Iijima, Youngjoon Kwon, Yoshihide Sakai, Kay Kinoshita, Kazuo Abe, Hidekazu Kakuno, and Christoph Schwanda. Others who were called upon and who I thank are Nick Hastings, Glenn Moloney, Bruce Yabsley, Tim Gershon, Brendan Casey, Eric Heenan, Bruce McKellar, Leon Moffitt, Elisabetta Barberio and Geoff Taylor. I have great admiration for the many hundreds of people that makeup the Belle collaboration and KEK-B accelerator team.

Last and most important is that which I can't reasonably state, Lou, my brother, you led, and I followed.

Contents

List of Figures

List of Tables

Chapter 1

Introduction

Early last century symmetries became guiding lights for physicists attempting to form and simplify physical laws. Particle physicists thought that all fundamental interactions were symmetric under the three discrete operations of parity (P), time reversal (T) and charge conjugation (C).

But in the late 1950's Lee and Yang [1] hypothesised that it was not true for weak interactions, and soon after parity and charge conjugation symmetries were found to be violated in weak decays [2–4]. The violations were separately maximal and thus the combined operation, CP, remained an unbroken symmetry. Then in 1964 Christenson, Cronin, Fitch, and Turlay [5] unexpectedly discovered CP violation. Ever since, the subject of CP violation has preoccupied particle physicists.

In 1967 the mystery surrounding CP violation heightened when Sakharov showed that it was a necessary ingredient for theories attempting to explain the matter-anti-matter asymmetry of the universe [6]. Could this broken symmetry be one of the reasons for our very existence? Perhaps, but the amount of CP violation allowed within the Standard Model of particle physics is too small to explain the discrepancy.

The Standard Model of particle physics is a mathematical framework that incorporates physical laws describing all that is known about particles and their interactions. This model emerged from experimental discoveries and theoretical advances in the 1960s-70s. It has been amazingly successful at explaining observed phenomena but many questions still remain. One relates to CP violation; why does it occur? The story of how CP violation is accommodated in the Standard Model is an intriguing one.

In 1963, before the Standard Model and even before the existence of quarks was experimentally verified, Cabibbo investigated strangeness changing decays. He found that quarks did not interact via the weak force as states of definite mass, but rather a down quark interacted as a mixture of down and strange flavour states, described with a mixing angle. This phenomenon is now known as Cabibbo mixing [7].

In 1970 Glashow, Iliopoulis, and Maiani proposed the existence of a fourth quark, the charmed quark, as a partner of the strange, to explain the lack of flavour changing neutral currents [8]. With two quark families Cabibbo mixing was encoded into a mixing matrix, however, described by one mixing angle it could not accommodate CP violation.

In 1972, Kobayashi and Maskawa (KM) noted that the existence of a third quark family would permit two more mixing angles and a phase in the mixing matrix [9]. The latter, if non-zero, would result in CP violation. This is known as the KM mechanism for CP violation.

Subsequent discoveries confirmed the existence of quarks and their arrangement into three families. The mixing matrix subsequently came to be known as the Cabibbo-Kobayashi-Maskawa (CKM) mixing matrix. The Standard Model says nothing of its contents, other than to conserve probability, the matrix must be unitary. Measurements of the CKM parameters are required to verify if this is in fact so. Such measurements will either point to a self-consistent CKM matrix or provide inconsistent representations of CKM parameters. The former would announce another success for the Standard Model, while the latter would present us with a much more intriguing scenario, the presence of new physics effects - perhaps in the form of yet unforeseen fundamental particles, which are predicted to exist in the many extensions to the Standard Model.

The CP violation observed in 1964 occurred in the decay of neutral K mesons (also known as kaons). In 1980 Sanda, Carter and Bigi showed the KM mechanism predicted large CP violating effects in certain B meson decays [10, 11]. This, coupled with a relatively long bottom (b quark) lifetime, ushered in the era of the B-factory.

A B-factory, as the name suggests, produces large numbers of B meson particles. Two such factories, currently in operation at KEK and SLAC, are host to the Belle and BaBar experiments, respectively. Both consist of a particle accelerator complex which collides electrons into their antimatter counterparts, positrons, at an energy best suited to producing B mesons. Both are producing only $B_{u,d}$ type mesons.[1]

That the CKM matrix must be unitary imposes relations amongst its elements, some can be represented as triangles in the complex plane. The sides of these triangles can be directly related to CKM matrix element magnitudes, while the angles are sensitive to CP violation effects. The triangle relating to $B_{u,d}$ meson decays, which has sides all roughly the same size, is known as the *Unitarity Triangle*.

Belle and Babar, which both commenced taking data in 1999, are vigorously pursuing *Unitarity Triangle* measurements. In 2001 both experiments simultaneously reported observation of CP violation in the interference between mixing and decay of neutral B mesons [12, 13]. Their observations, which were in agreement, were consistent with KM expectations and placed severe constraints on one angle of the *Unitarity Triangle*, known as ϕ_1 or β.

Further measurements of B meson decays would go a long way to determine whether the KM mechanism is adequate to account for all instances of CP violation. It is hoped that indications of new physics will be found and that eventually an understanding why CP violation occurs at all will be reached.

This thesis investigates inclusive charmless semileptonic B meson decays, using data collected with

[1] where the subscript denotes the flavour of the quark bound to the b quark in the meson

the Belle detector. The measurement of the fraction of B mesons that decay via this mode can be used to calculate the CKM matrix element $|V_{ub}|$. $|V_{ub}|$ is one of the smallest elements, which makes a precision determination of it very difficult. Currently it's value is known to within about 15%.

This thesis concentrates on determining $|V_{ub}|$ through a study of the electron momentum spectrum, a so-called *endpoint analysis*. While this is currently not generally regarded as the best avenue to precisely determine $|V_{ub}|$, it still offers much insight into the theoretical uncertainties that pervade, although at a reduced level, more recent determinations. Moreover, since the last mature endpoint analysis was reported [14], the significant backgrounds in the analysis have become better understood. Furthermore, necessary to determining $|V_{ub}|$, this thesis also investigates measurements of theoretical parameters that are of consequence in all $|V_{ub}|$ measurements made from inclusive charmless semileptonic B meson decays.

In summary, better measurements of $|V_{ub}|$ are needed to help further constrain the KM parameters and test whether the KM mechanism is truly adequate to describe nature.

Chapter 2

On inclusive charmless semileptonic *B* meson decays

2.1 The Standard Model

The Standard Model summarises the current state of knowledge in particle physics. Written in the language of relativistic quantum field theory, it is a gauge theory based on $SU(3) \otimes SU(2) \otimes U(1)$. It combines the theory of strong interactions, known as Quantum Chromodynamics (QCD), with the unified theory of electroweak interactions.

In the Standard Model particles are classified as either fermions or bosons. A fermion is any particle with half-integer spin while a boson is one with integer spin. The spin, measured in units of angular momentum, is quantised, and is as intrinsic to a particle as mass or charge. The fermions of the Standard Model, which form the fundamental constituents of matter, are the quarks and leptons. The bosons are gauge particles which mediate the interactions.

QCD, based on the $SU(3)$ gauge symmetry, describes the strong interactions of coloured quarks and gluons. There are three colour charge states denoted red, blue and green, and there are eight massless gluon bosons. Quarks, always found bound to other quarks, are confined in mesons (quark-anti-quark pairs) and baryons (quark triplets). QCD dictates that these are colour-charge neutral states. Collectively, mesons and baryons are known as hadrons. The residual colour force between quarks in nucleons is responsible for the strong nuclear force.

The combined theory of electroweak interactions, based on the gauge symmetry $SU(2)_L \otimes U(1)_Y$, describes the weak and electromagnetic interactions. The symmetry is spontaneously broken through the Higgs mechanism to $U(1)_{EM}$, which has the effect of giving mass to the weak gauge bosons, $W^{\pm}$ and Z^0, while leaving the electromagnetic gauge boson, the photon, massless.

There are six flavours of leptons and quarks. The weak interaction distinguishes left handed leptons

Leptons				Quarks			
Flavour	Symbol	Mass GeV/c^2	Electric charge	Flavour	Symbol	Mass GeV/c^2	Electric charge
electron neutrino	ν_e	$< 10^{-8}$	0	up	u	0.003	2/3
electron	e	0.000511	-1	down	d	0.006	-1/3
muon neutrino	ν_μ	< 0.0002	0	charm	c	1.3	2/3
muon	μ	0.106	-1	strange	s	0.1	-1/3
tau neutrino	ν_τ	< 0.02	0	top	t	175	2/3
tau	τ	1.7771	-1	bottom	b	4.3	-1/3

Table 2.1: The fermion families of the Standard Model.

Unified Electroweak spin=1		
Name	Mass GeV/c^2	Charge
γ photon	0	0
W^-	80.4	-1
W^+	80.4	+1
Z^0	91.187	0
Strong (Colour) spin = 1		
Name	Mass GeV/c^2	Charge
g gluon	0	0

Table 2.2: The bosons of the Standard Model.

and quarks into three families consisting of two flavour members each. Within a family the members are arranged according to electromagnetic charge. The families are ordered from heaviest to lightest. All fermions interact via the weak gauge bosons, which in most cases mediate decay of heavier particles to lighter particles.

The arrangement and properties of all the flavoured quarks and leptons are shown in Table 2.1. The gauge boson properties are shown in table 2.2.

2.2 CP violation in the Standard Model

The Standard Model Lagrangian is invariant under the combined action of the discrete operations C, P, and T, each defined as:

C **- Charge conjugation** transforming a particle into it's antiparticle;

P **- Parity inversion** changing the handedness of states, *i.e.* right handed to left handed and vice-versa;

T **- Time inversion** reversing the direction of time.

CPT invariance is manifest in all quantum field theories that obey the general conditions of: satisfying Lorentz invariance; possessing a lowest energy state in its energy spectrum (a vacuum); and micro-causality. CPT invariance demands a particle and its corresponding anti-particle have the same mass and lifetime; so far all observations respect this statement.

CP violation was first observed in the weak decay of a neutral kaon, the K_L. Initially thought to be a pure CP-odd weak-eigenstate, it was found to decay to a CP-even state of two charged pions, $\pi^+\pi^-$. The extent of the violation was small, occurring two in every thousand K_L decays, but was undeniable nonetheless. Within the Standard Model the only possible source of this type of CP violation resides in the charged weak decay of quarks. Specifically, the weak charged current mediating the interaction between quarks is given by

$$J_\mu^{cc} = (\bar{u} \quad \bar{c} \quad \bar{t})\gamma_\mu V_{\text{CKM}} \begin{pmatrix} d \\ s \\ b \end{pmatrix}, \tag{2.1}$$

where V_{CKM} is the Cabibbo-Kobayashi-Maskawa mixing matrix. V_{CKM} transforms quark mass eigenstates from the mass to the weak basis. By convention the matrix acts on the quarks with charge $\frac{-e}{3}$, and is written as

$$V_{\text{CKM}} = \begin{pmatrix} V_{ud} & V_{us} & V_{ub} \\ V_{cd} & V_{cs} & V_{cb} \\ V_{td} & V_{ts} & V_{tb} \end{pmatrix}. \tag{2.2}$$

The CKM matrix elements can be parameterised by three real angles and a phase. The existence of this *irreducible* phase, if non-zero, is the source of time-reversal symmetry, T, and hence CP not being a symmetry of the weak interaction. An infinite number of parameterisations could be chosen, however some are better at exposing the underlying physics than others. All observations are parameterisation independent. The standard parameterisation of the matrix is given by:

$$\hat{V}_{\text{CKM}} = \begin{pmatrix} c_{12}c_{13} & s_{12}c_{13} & s_{13}e^{-i\delta} \\ -s_{12}c_{23} - c_{12}s_{23}s_{13}e^{i\delta} & c_{12}c_{23} - s_{12}s_{23}s_{13}e^{i\delta} & s_{23}c_{13} \\ s_{12}s_{23} - c_{12}c_{23}s_{13}e^{i\delta} & -s_{23}c_{12} - s_{12}c_{23}s_{13}e^{i\delta} & c_{23}c_{13} \end{pmatrix}, \tag{2.3}$$

where $c_{ij} = \cos\theta_{ij}$, $s_{ij} = \sin\theta_{ij}$ where $i, j = 1, 2, 3$ label the quark family and δ is the phase. The c_{ij} and s_{ij} can all be chosen to be positive and δ may vary in the range $0 \leq \delta \leq 2\pi$.

A useful parameterisation of V_{CKM}, proposed by Wolfenstein [15], expresses the CKM matrix elements as an expansion in powers of the sine of the Cabibbo mixing angle, $\lambda \equiv \sin\theta_c$. The matrix is almost diagonal, and its elements get smaller the further they are from the diagonal. It is parameterised by the four Wolfenstein parameters, $(\lambda(\equiv \sin\theta_c) = 0.22, A, \varrho, \eta)$, which are all of order unity. For improved accuracy the following parameter definitions in the original Wolfenstein parameterisation are adopted:

$$s_{12} = \lambda\,; \qquad s_{23} = A\lambda^2\,; \qquad s_{13}e^{-i\delta} = A\lambda^3(\varrho - i\eta), \tag{2.4}$$

which are valid to *all orders* in λ. It follows that

$$\varrho = \frac{s_{13}}{s_{12}s_{23}}\cos\delta, \qquad \eta = \frac{s_{13}}{s_{12}s_{23}}\sin\delta, \tag{2.5}$$

and therefore

$$\hat{V}_{\mathrm{CKM}} = \begin{pmatrix} 1 - \frac{1}{2}\lambda^2 - \frac{1}{8}\lambda^4 & \lambda + \mathcal{O}(\lambda^7) & A\lambda^3(\varrho - i\eta) \\ -\lambda + \frac{1}{2}A^2\lambda^5[1 - 2(\varrho + i\eta)] & 1 - \frac{1}{2}\lambda^2 - \frac{1}{8}\lambda^4(1 + 4A^2) & A\lambda^2 + \mathcal{O}(\lambda^8) \\ A\lambda^3(1 - \overline{\varrho} - i\overline{\eta}) & -A\lambda^2 + \frac{1}{2}A\lambda^4[1 - 2(\varrho + i\eta)] & 1 - \frac{1}{2}A^2\lambda^4 \end{pmatrix}, \tag{2.6}$$

where

$$\overline{\varrho} = \varrho(1 - \frac{\lambda^2}{2}), \qquad \overline{\eta} = \eta(1 - \frac{\lambda^2}{2}). \tag{2.7}$$

The unitarity of V_{CKM}, $VV^\dagger = I$, leads to relations amongst its elements, for example $\sum_i V_{id}V_{is}^* = 0$, $\sum_i V_{is}V_{ib}^* = 0$ and $\sum_i V_{id}V_{ib}^* = 0$. These relations can be drawn as triangles in the complex plane. The triangle formed from the unitarity relation imposed on the first and third columns has special significance since it is one of the few such triangles with sides of roughly the same length ($\mathcal{O}(\lambda^3)$), which is suggestive of large CP violating effects in $B_{u,d}$ meson decays. It is known as the *Unitarity Triangle*. The relation is given by

$$V_{ud}V_{ub}^* + V_{cd}V_{cb}^* + V_{td}V_{tb}^* = 0. \tag{2.8}$$

Figure 2.1 depicts the Unitarity Triangle, rescaled by dividing relation (2.8) by $|V_{cd}V_{cb}^*|$ and choosing a phase convention such that $(V_{cd}V_{cb}^*)$ is real. This fixes two vertices at $(0, 0)$ and $(0, 1)$ with the remaining vertex having coordinates $(\bar{\varrho}, \bar{\eta})$. The angles and side-lengths are given by:

$$\phi_1 \equiv \left[-\frac{V_{cd}V_{cb}^*}{V_{td}V_{tb}^*} \right]; \qquad \phi_2 \equiv \left[-\frac{V_{ud}V_{ub}^*}{V_{td}V_{tb}^*} \right]; \qquad \phi_3 \equiv \left[-\frac{V_{cd}V_{cb}^*}{V_{ud}V_{ub}^*} \right] \equiv \pi - \phi_1 - \phi_2; \tag{2.9}$$

$$R_b \equiv \frac{|V_{ud}V_{ub}^*|}{|V_{cd}V_{cb}^*|} = \sqrt{\overline{\varrho}^2 + \overline{\eta}^2} = (1 - \frac{\lambda^2}{2})\frac{1}{\lambda}\left|\frac{V_{ub}}{V_{cb}}\right|; \tag{2.10}$$

$$R_t \equiv \frac{|V_{td}V_{tb}^*|}{|V_{cd}V_{cb}^*|} = \sqrt{(1 - \overline{\varrho})^2 + \overline{\eta}^2} = \frac{1}{\lambda}\left|\frac{V_{ub}}{V_{cb}}\right|. \tag{2.11}$$

The angles are sensitive to CP asymmetries since they are dependent on the phase. The current measured constraints of the Unitarity Triangle are drawn in figure 2.2. At present the five measurements that restrict

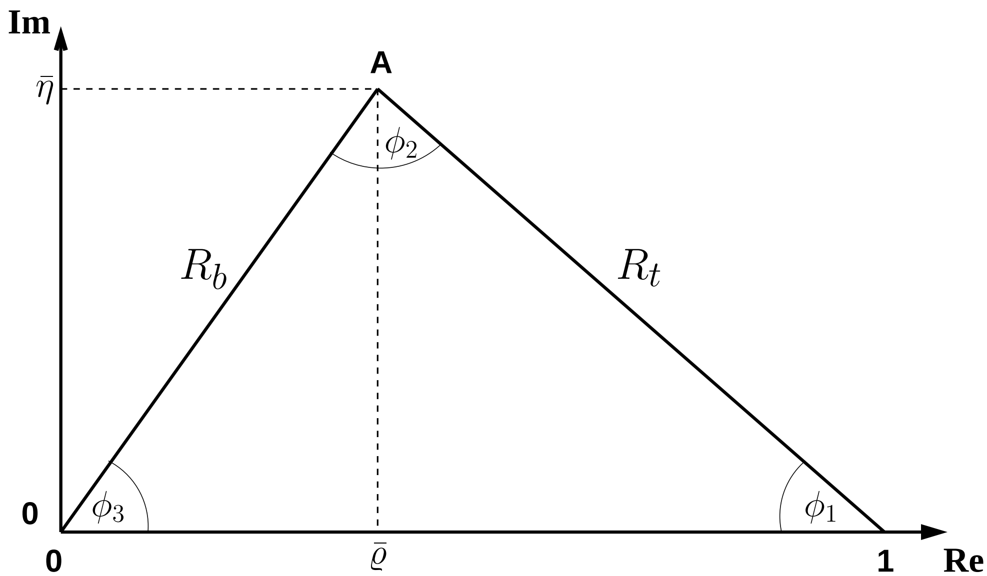

Figure 2.1: The rescaled Unitarity Triangle

the range of $(\bar{\varrho}, \bar{\eta})$ are:

- $|V_{ub}|$, measured from semileptonic B meson decays, which limits the accuracy in determining the sidelength R_b;
- ϵ_K, measured from neutral kaon decays to two pions, which defines a hyperbola about $(1, 0)$;
- Δm_d , measured from $B_d^0 - \overline{B}_d^0$ mixing, which determines sidelength R_t;
- $\Delta m_d/\Delta m_s$, measured from $B_s^0 - \overline{B}_s^0$ and $B_d^0 - \overline{B}_d^0$ mixing, which determines R_t in a different way to that above;
- $a(J/\psi K_s)$, the time dependent CP asymmetry in $B \to J/\psi K_S$, induced in the interference between mixing and decay of neutral B mesons, which determines angle ϕ_1 up to a four-fold ambiguity.

For more information on the constraints of the *Unitarity Triangle* see references [16, 17].

Of interest to this thesis is the sidelength R_b. Each of the inputs to R_b are determined from tree level decays and therefore are, to excellent accuracy, independent of any new physics contributions. One might think it uninteresting to investigate channels which provide little hope of a new physics discovery, however, the significance of R_b lies in its status as a fundamental constant valid in any extension of the Standard Model. Resolving each of the factors in R_b using world averages [17] gives:

$$|V_{ud}| = 0.9738 \pm 0.0005; \qquad |V_{cb}| = (41.3 \pm 1.5) \times 10^{-3}; \tag{2.12}$$

$$|V_{cd}| = 0.224 \pm 0.012; \qquad |V_{ub}| = (3.67 \pm 0.47) \times 10^{-3}, \tag{2.13}$$

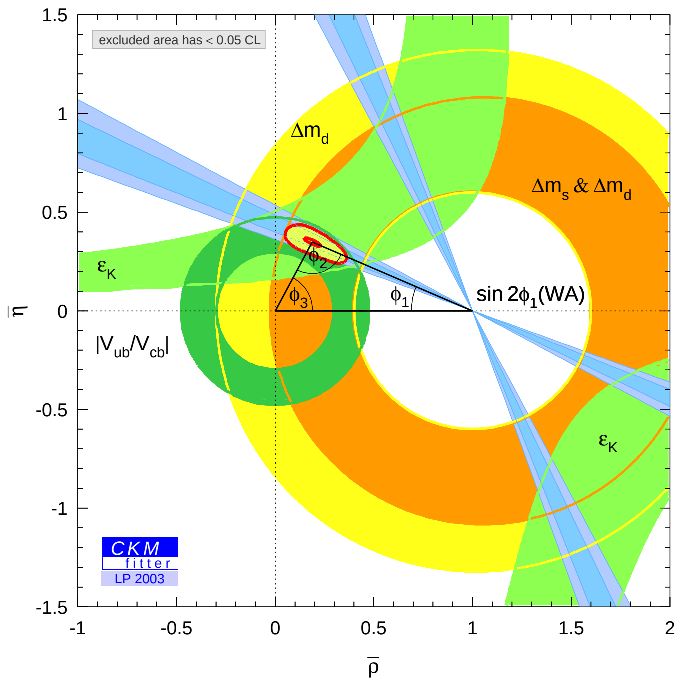

Figure 2.2: Constraints on the Unitarity Triangle in the Improved Wolfenstein parameterisation

which implies

$$R_b = 0.39 \pm 0.06\,. \tag{2.14}$$

The uncertainty in R_b is dominated by that in $|V_{ub}|$.

2.3 Accessing $|V_{ub}|$

By examining the Standard Model charged current describing the weak decay of quarks in equation 2.1, it may be seen that $|V_{ub}|$ is the strength of the b quark coupling to a u quark via a charged weak boson, $W^{\pm}$. The $W^{\pm}$ is virtual and decays to either lepton or quark pairs. The rate of any process that contains the $b \to uW$ transition will depend on $|V_{ub}|$. All things being equal, any measurement of a $b \to uW$ transition would suffice to extract $|V_{ub}|$.

All things aren't equal. A quark in isolation has never been observed. Quarks live only in hadrons, confined to other quarks via the colour force, as described by QCD. The complication arises because the QCD coupling constant is believed to grow as the energy scale is lowered, which leads to the phenomenon of *confinement*.

Perturbative expansions in the strong coupling α_s, which are used to calculate physical quantities such as decay rates, become useless, and thus problems require non-perturbative treatment. Since the $b \to uW$ transition is confined within a hadron, the decay rate is sensitive to the so-called non-perturbative meson dynamics.

Fortunately theorists have been able to discover and exploit properties of the QCD Lagrangian in kinematic regions that allow for meaningful calculations to be made. These techniques are introduced and discussed with relevance to $|V_{ub}|$ in the following subsection.

It's worth mentioning that at higher energies QCD exhibits the property of *asymptotic freedom*. The QCD coupling here is found to be small, which allows calculations to be made through perturbative expansions. Separating the regimes of perturbative and non-perturbative dynamics is the scale denoted as Λ_{QCD}, which is roughly equal to $200\,\mathrm{MeV}$.

2.3.1 Inclusive Charmless Semileptonic B meson decays

A charmless semileptonic B meson decay is one where the b quark within the meson decays into an up flavour quark, u, and a virtual charged weak boson, W, which promptly produces a charged lepton, l, and lepton-neutrino, ν_l. The decay interaction is written as

$$B \to X_u l \nu_l. \tag{2.15}$$

The Feynman diagram of this process is shown in figure 2.3. Accompanying the b quark is the so-called spectator quark, denoted $\bar{q}$. The decay is regarded as inclusive when all possible X_u are considered. The decay is said to be exclusive when X_u is specified, for example $B \to \pi l \nu_l$. A charmed, as opposed to a charmless semileptonic B meson decay, corresponds to the case where the b quark decays to a charmed quark (c) instead.

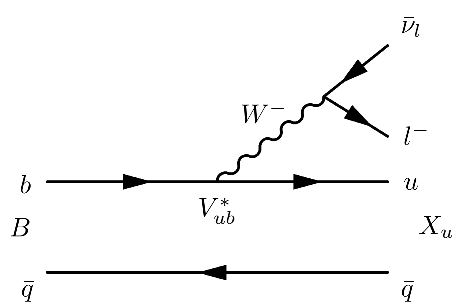

Figure 2.3: Feynman diagram of a charmless semileptonic B meson decay.

The presence of the leptonic component simplifies the theoretical treatment to the point of making $|V_{ub}|$ measurement through the semileptonic channel favourable and feasible compared to that of a purely hadronic B meson decay.

The process of calculating the inclusive rate, $\Gamma(B \to X_u l \nu_l)$ as a function of V_{ub}, is well presented by Manohar and Wise [18]. The steps undertaken are summarised here.

The semileptonic B decay process is well described by the low energy effective weak Hamiltonian[1]

$$H_W = \frac{4G_F}{\sqrt{2}} V_{ub} \bar{u} \gamma^\mu P_L b \bar{l} \gamma_\mu P_L \nu_l, \tag{2.16}$$

where G_F is the Fermi constant and $P_L = \frac{1}{2}(1-\gamma_5)$ projects out the left-handed state. The triple differential decay rate written in terms of the virtual W boson mass squared, q^2, lepton and neutrino energies, E_l and E_{ν_l}, respectively, is then given by

$$\frac{d^3\Gamma(B \to X_u l \nu_l)}{dq^2 dE_l dE_{\nu_l}} = \frac{1}{4} \sum_{X_u} \sum_{\text{spins}} \frac{|\langle X_u l \bar{\nu}_l | H_W | \overline{B} \rangle|^2}{2m_B} (2\pi)^3 \delta^4(p_B - q - p_{X_u}), \tag{2.17}$$

where p_Y denotes the four-momentum of particle, Y. This can be further simplified to

$$\frac{d^3\Gamma(B \to X_u l \nu_l)}{dq^2 dE_l dE_{\nu_l}} = 2G_F^2 |V_{ub}|^2 W_{\alpha\beta} L^{\alpha\beta}, \tag{2.18}$$

where all the physics now resides in the leptonic tensor, $L^{\alpha\beta}$, and hadronic tensor, $W_{\alpha\beta}$. As the name suggests, $L^{\alpha\beta}$ describes the leptonic current produced from the W decay. Since leptons don't feel the strong force and therefore are not subject to non-pertubative problems of the quarks, the expression for $L^{\alpha\beta}$ can be evaluated rather simply. Neglecting lepton mass it is given by

$$L^{\alpha\beta} = 2(p_l^\alpha p_{\nu_l}^\beta + p_l^\beta p_{\nu_l}^\alpha - g^{\alpha\beta} p_l \cdot p_{\nu_l} - i\epsilon^{\eta\beta\lambda\alpha} p_{l\eta} p_{\nu_l \lambda}). \tag{2.19}$$

In contrast, $W_{\alpha\beta}$, which parameterises all strong interaction physics relevant for inclusive semileptonic $\overline{B}$ meson decay is given by

$$W^{\alpha\beta} = \sum_{X_c} (2\pi)^3 \delta^4(p_B - q - p_{X_u}) \frac{1}{m_B} \langle \overline{B}(p_B) | J_L^{\dagger\alpha} | X_c(p_{X_c}) \rangle \langle X_c(p_{X_c}) | J_L^\beta | \overline{B}(p_B) \rangle, \tag{2.20}$$

where $J_L^\alpha = \bar{u}\gamma^\alpha P_L b$. It cannot be so easily simplified, and must be approximated. The first step is to use the Optical Theorem to relate $W_{\alpha\beta}$ to the time-ordered product of currents, $T_{\alpha\beta}$, such that

$$W_{\alpha\beta} = -\frac{1}{\pi} \operatorname{Im} T_{\alpha\beta} = -\frac{1}{\pi} \operatorname{Im} \int d^4x e^{-iq.x} \frac{\langle \overline{B} | T\left[J_{L\alpha}^\dagger(x) J_{L\beta}(0)\right] | \overline{B} \rangle}{2m_B}. \tag{2.21}$$

The second step is the use of the Operator Product Expansion (OPE). Employed in describing weak decays of hadrons, the OPE has the effect of defining two energy regimes; short distance (perturbative) in the coefficient functions, and long distance (non-perturbative) in the matrix elements of the local operators.

Specifically, in momentum space, in the limit of large momenta ($q \gg \Lambda_{\text{QCD}}$) and small separation, the operator product can be expanded in terms of local operators with coefficient functions that depend on q. In

[1] The energies involved are much less than the W mass.

this limit the time ordered product is dominated by short distances, $x \ll \Lambda_{\rm QCD}^{-1}$, and the nonlocal hadronic tensor, $T^{\alpha\beta}$, can be expressed as a sum of local operators.

The mass of the b quark, denoted by m_b, within the B meson, defines the scale of the interaction, $q \sim \mathcal{O}(m_b)$. The coefficient functions are calculable as a perturbative series expansion in $\alpha_s(m_b)$. The local operators are written in the language of Heavy Quark Effective Theory (HQET).

HQET, derived from the QCD Lagrangian in the limit of a heavy quark mass, describes the dynamics of hadrons containing a heavy quark. It provides a valid description of physics at momenta much smaller than m_Q, where Q denotes the heavy quark. The HQET Lagrangian, constructed in inverse powers of m_Q, to first order in $1/m_Q$, is given by

$$\mathcal{L}_{\rm HQET} = \bar{Q}_v(iv \cdot D)Q_v - \bar{Q}_v \frac{D_\perp^2}{2m_Q} Q_v - g\bar{Q}_v \frac{\sigma_{\mu\nu}G^{\mu\nu}}{4m_Q} Q_v, \tag{2.22}$$

where:

$$\begin{aligned} v &= \text{heavy quark four-velocity;} \\ Q_v &= \text{heavy quark field;} \\ m_Q &= \text{heavy quark mass;} \\ G^{\mu\nu} &= \text{Gluon field strength tensor.} \end{aligned}$$

In the limit, $m_Q \to \infty$, the HQET Lagrangian is invariant to the flavour and spin of the heavy quark. The former symmetry arises since quark flavour is mass dependent and the latter since the heavy quark can only interact with the *light degrees of freedom* (light mass quarks and surrounding gluons) via its chromoelectric charge, which is spin independent. Within the context of a B meson, this is the case of a b quark behaving as a static external source of colour, and whose interaction with the light degrees of freedom fully describes the meson dynamics. The $1/m_Q$ terms explicitly break the flavour symmetry, whilst the last term, a magnetic moment interaction, breaks the spin symmetry as well.

In the B rest frame, the b quark is almost on shell with momentum fluctuation, k, which is of order $\Lambda_{\rm QCD}$ around the mass shell, and the b quark momentum is written as

$$p_b = m_b v + k. \tag{2.23}$$

At lowest order in perturbation theory (leading order in α_s), the matrix element of $T_{\alpha\beta}$ between the b quark states is given by

$$\frac{1}{(m_b v - q + k)^2 - m_q^2 + i\epsilon} \bar{b}\gamma_\alpha P_L (m_b \gamma^\mu v_\mu - \gamma^\mu q_\mu + \gamma^\mu k_\mu)\gamma_\beta P_L b. \tag{2.24}$$

Expanding in powers of k gives an expansion in Λ_{QCD}/m_b and therefore the expansion in local operators can be resolved into effects in powers of $1/m_b$. Shown schematically this is [16]:

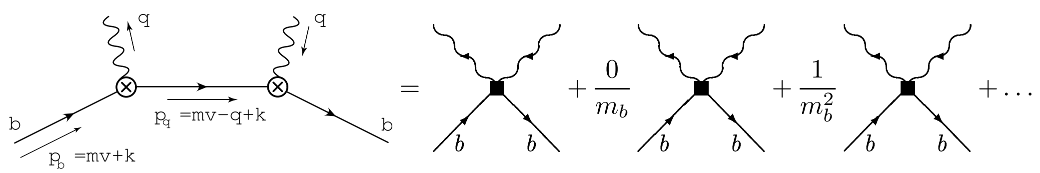

(2.25)

Together with perturbative effects built into the coefficients and parameterised by α_s, the OPE describes a simultaneous expansion in α_s and $1/m_b$. To leading order in α_s the inclusive charmless semileptonic B meson decay rate is given by

$$\Gamma(B \to X_u l \nu_l) = \frac{G_F^2 m_b^5}{192\pi^3} |V_{ub}|^2 \Big[1 + \frac{\lambda_1}{2m_b^2} + \frac{3\lambda_2}{2m_b^2}\Big(2\rho\frac{d}{d\rho} - 3\Big)\Big] f(\rho), \tag{2.26}$$

where

$$f(\rho) = 1 - 8\rho + 8\rho^3 - \rho^4 - 12\rho^2 \ln\rho, \qquad \rho = \frac{m_u^2}{m_b^2}, \tag{2.27}$$

and m_u denotes the u-quark mass. Terms of order $1/m_b$ do not play a role as a consequence of the heavy quark equation of motion. $\lambda_{1,2}$ are non-perturbative parameters that result from the $1/m_b$ terms in the heavy quark Lagrangian. λ_1 is proportional to the kinetic energy, K_b, of the b quark within the B meson, and is given by

$$\lambda_1 = -2m_b K_b. \tag{2.28}$$

λ_2 derives from the magnetic interaction of the heavy quark with the *light degrees of freedom* and can be related to heavy quark meson mass splittings, such that

$$\lambda_2 = \frac{m_{B^*}^2 - m_B^2}{4}. \tag{2.29}$$

To leading order in α_s and $1/m_b$ the rate simply corresponds to that of a free b quark decay. For $B \to X_u l \nu_l$ decay it is reasonable to set $m_u = 0$, and therefore in the limit $\rho \to 0$

$$\Gamma(B \to X_u l \nu_l) = \frac{G_F^2 m_b^5}{192\pi^3} |V_{ub}|^2 \Big[1 + \frac{\lambda_1}{2m_b^2} - \frac{9\lambda_2}{2m_b^2}\Big]. \tag{2.30}$$

The crucial factor in this expression is the dependence on the b quark mass. Using references [19–22] the Large Electron-Positron collider (LEP) $|V_{ub}|$ working group give

$$|V_{ub}| = 0.00445 \times \big(1 \pm 0.052|_{m_b} \pm 0.020|_{\lambda_{1,2}}\big) \left(\frac{\mathcal{B}(B \to X_u l \nu)}{0.002}\right)^{\frac{1}{2}} \left(\frac{1.55\ \mathrm{ps}}{\tau_B}\right)^{\frac{1}{2}}, \tag{2.31}$$

where τ_B is the lifetime of the B meson, the larger of the uncertainties derives from the b quark mass, as measured in the *kinetic* scheme ($m_b^{\mathrm{kin}} = (4.58 \pm 0.09)\,\mathrm{GeV}/c^2$ has been assumed). The calculation includes perturbative and non-perturbative corrections to order α_s^2 and $1/m_b^3$ respectively.

The *quark-hadron duality* assumption underlies the OPE, it presumes the equivalence of rates calculated at the quark level with those at the hadron level. For the full rate Bigi and Uraltsev estimate the effect of possible discrepancy to be below the half percent level [23]. Gibbons estimates a net uncertainty of 4% on total rate via a comparison of inclusive and exclusive $|V_{cb}|$ measurements [24]. In general, the uncertainty is yet to be incorporated into the $|V_{ub}|$ extraction formula.

The lepton energy spectrum

A measurement of the full semileptonic rate will give $|V_{ub}|$ to a precision of about 6%. Unfortunately the full rate is out of reach of current experiments. Problems arising from the large $B \to X_c l \nu_l$ background, which has a rate roughly 60 times that of $B \to X_u l \nu_l$, restricts analysis to limited regions of phase space where a measurement is feasible.

The electron energy is the kinematic variable of interest to this work.[2]

In the rest frame of a charmed semileptonic B meson decay, the electron energy kinematic endpoint, $E_l^{\max}$, is dependent on the mass of the lowest lying charmed meson, the D-meson, and is given by[3]

$$E_l^{\max} = \frac{M_B}{2}\left(1 - \left(\frac{M_D}{M_B}\right)^2\right) = 2.32\,\mathrm{GeV}, \tag{2.32}$$

where M_B and M_D are the masses of the B and D mesons respectively. The energy endpoint for charmless semileptonic decay, likewise dependent on the lowest mass X_u meson, the π meson, reaches beyond that above to $2.64\,\mathrm{GeV}$. The region spanned between the charmed and charmless decay kinematic endpoints is known as the *endpoint region*, as depicted in figure 2.4. Often the use of the term *endpoint region* may also imply regions that include momenta below the endpoint.

Measuring the yield of leptons above the endpoint provides the partial rate. In reality the knowledge of the charmed background is adequate enough, to a point, for sufficiently accurate measurements of the partial rate to be made in regions that include energies below the endpoint. Extrapolating from the partial to the full rate requires knowledge of the shape of the energy spectrum, $\frac{d\Gamma}{dE_l}$.

In calculating the full rate in the previous section, no mention was made of the intermediate differential rates necessary to go from equation 2.18 to 2.26. The differential rate for $B \to X_u e \nu_e$ as a function of the scaled energy, $y(\equiv 2E_e/m_b)$, is an expansion both in $\Lambda_{\mathrm{QCD}}/m_b$ and $\Lambda_{\mathrm{QCD}}/[m_b(1-y)]$, and is given

[2] Measurement of the electron momentum spectrum is performed rather than the energy spectrum. Due to the negligible mass of the electron they are practically indistinguishable.

[3] Neglecting lepton mass.

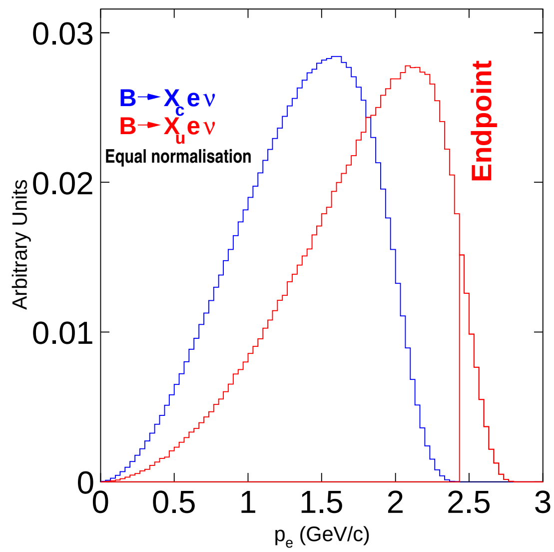

Figure 2.4: The endpoint region, as measured in the $\Upsilon(4S)$ rest frame.

by [18]

$$\begin{aligned}\frac{d\Gamma}{dy} &= \frac{G_F^2 m_b^5}{192\pi^3}|V_{ub}|^2\Bigg\{\left[2(3-2y)y^2-6y^2\rho-\frac{6y^2\rho^2}{(1-y)^2}+\frac{2(3-y)y^2\rho^3}{(1-y)^3}\right]\\ &\quad -\frac{2\lambda_1}{m_b^2}\left[-\frac{5}{3}y^3-\frac{y^3(5-2y)\rho^2}{(1-y)^4}+\frac{2y^3(10-5y+y^2)\rho^3}{3(1-y)^5}\right]\\ &\quad -\frac{2\lambda_2}{m_b^2}\left[-\frac{(6y^2+5y)}{3}+\frac{2y^2(3-2y)\rho}{(1-y)^2}+\frac{3y^2(2-y)\rho^2}{(1-y)^3}-\frac{5y^2(6-4y+y^2)\rho^3}{3(1-y)^4}\right]\Bigg\}\end{aligned} \tag{2.33}$$

Unfortunately $\frac{d\Gamma}{dy}$ becomes singular in the endpoint region and the neglected higher order terms in the HQET become important as their contributions are of $\mathcal{O}(\Lambda_{\rm QCD}/[m_b(1-y)])^n$, which are comparable to one. To account for these effects a re-summation of the leading endpoint singularities is performed, resulting in, at leading order in twist [4], to a shape function that encodes the non-perturbative dynamics.

In general, restricted kinematic regions that do not suffer from breakdown of the OPE sample hadronic final states with

$$m_X^2 \gg E_X\Lambda_{\rm QCD} \gg \Lambda_{\rm QCD}^2, \tag{2.34}$$

where E_X and M_X are the energy and invariant mass of the final hadronic state. Therefore the low M_X

[4]The terms appearing in the HQET Lagrangian can be ordered according to twist. The twist is the spin subtracted from the dimension. For example, the quark fields, q, have a twist of one, as does the gluon field strength tensor, $G_{\mu\nu}$, while the covariant derivative has a twist of zero.

Parameter	q	$G_{\mu\nu}$	D^μ
Dimension	3/2	2	1
Spin	1/2	1	1
Twist	1	1	0

region, which does not satisfy this criteria, also requires re-summation, and therefore needs to be described with a shape function.

The shape function $F(k_+)$ describes the motion of the b quark inside the B meson, known as the *Fermi motion*. Here

$$k^\mu = p_b^\mu - m_b v^\mu \tag{2.35}$$

and

$$k_+ = k^0 + k_{\|}, \tag{2.36}$$

where k^μ is the residual momentum of the b quark. The longitudinal and transverse spatial components, $k_{\|}$ and $k_\perp$, respectively, are defined relative to $m_b v^\mu - q^\mu$, which roughly corresponds to the direction of the recoiling u-quark. At this order, the so-called "jiggling" from $k_\perp$ is ignored.

De Fazio and Neubert [25] describe the method for migrating from the parton to the hadron level as a convolution of the parton-level spectra with the shape function, whereby the scaled energy variable, y, has been transformed to y_k through the substitution of m_b with $(m_b + k_+)$, while the boundaries have been shifted from the quark to the hadron level, thus giving the lepton energy spectrum in the B-meson rest frame as

$$\frac{\mathrm{d}\Gamma}{\mathrm{d}E_l} = 2\int_{2E_l - m_b}^{M_B - m_b} \mathrm{d}k_+ \, \frac{F(k_+)}{m_b + k_+} \, \frac{\mathrm{d}\Gamma}{\mathrm{d}y}(y_k)\,, \qquad 0 \le E_l \le \frac{M_B}{2}, \tag{2.37}$$

Unfortunately the form of the shape function is not determined from theory. It's moments, A_n, are given by forward matrix elements of leading-twist, higher-dimension operators in HQET, defined as[5]

$$A_n = \int dk_+ k_+^n F(k_+) = \langle B(v)|\bar{h}_v (iD_+)^n h_v |B(v)\rangle. \tag{2.38}$$

The first few moments, calculated using the HQET equation of motion, are given by:

$$A_0 = 1; \qquad A_1 = 0; \qquad A_2 = \frac{\mu_\pi^2}{3}. \tag{2.39}$$

The leading twist non-perturbative effects, encoded in the shape function, are universal to all $b \to u, d, s$ quark transition processes, for example the photon energy spectrum in $B \to X_s \gamma$ decays is likewise sensitive to the *Fermi motion*. An analogous expression to equation 2.37 holds for the photon energy in $B \to X_s\gamma$. All that is required is an exchange of labels, lepton to photon, $l \to \gamma$, as well as the substitution of the $b \to u l \nu_l$ parton-level spectrum with that of $b \to s\gamma$.

The idea is to use the photon energy spectrum to extract information about the *Fermi motion* and apply it to the calculation of the $B \to X_u l \nu_l$ energy spectrum [25, 27, 28]. This would then give the spectral fractions needed to extrapolate partial rate measurements to the full phase space. The CLEO collaboration,

[5] See reference [26] for detailed information on the shape function and its role in the calculation of the $B \to X_u l \nu_l$ lepton energy spectrum.

using several models for the shape function form presented in the literature, extracted the shape function parameters from a fit to their photon energy spectrum as measured in data [29] and calculated spectral fractions for their V_{ub} endpoint analysis [14, 30]. Of course, this method has its limitations, since differences between $B \to X_s\gamma$ and $B \to X_u l\nu_l$ exist at subleading orders in the expansion. Following the CLEO analysis these were first studied by Leibovich, Ligeti and Wise [31], the following discussion is derived from their work. The subleading twist corrections to both $B \to X_s\gamma$ and $B \to X_u l\nu_l$ come from three sources:

(i) forward scattering matrix element of any dimension 4 operator $\langle B(v)|\bar{b}_v iD^\alpha b_v|B(v)\rangle$, does not vanish but includes corrections, due to higher order terms in the HQET Lagrangian;

(ii) corrections to the spinor relation between the b-quark field in QCD and HQET;

(iii) corrections to the leading contribution of the one-gluon matrix element (the case of a gluon being coupled to the internal quark line in the left-most diagram shown in equation 2.25.)

In the expression for $d\Gamma/dy$ these effects are formally of $\mathcal{O}(\Lambda_{\mathrm{QCD}}/m_b)^2$ and include all terms proportional to $\lambda_2\delta(1-y)$. For each effect the relevant higher dimensional terms in the OPE can be re-summed into a subleading shape function. The function relating to (i) is insensitive to the heavy quark spin and universal to $B \to X_s\gamma$ and $B \to X_u l\nu_l$, and therefore can be absorbed into the definition of the leading twist shape function. Of the remaining shape functions, which are sensitive to the heavy quark spin, that from source (iii) is most important, since the respective factors at which it enters the OPE in $B \to X_s\gamma$ and $B \to X_u l\nu_l$ differs by 4 ($3/2$ in $B \to X_s\gamma$ and $11/2$ in $B \to X_u l\nu_l$). Corrections to the endpoint rate from this subleading shape function range from -10% to -40% as the lower momentum cutoff is increased from $2.0\,\mathrm{GeV}$ to $2.4\,\mathrm{GeV}$. Information from $B \to X_s\gamma$ can only mask a third of the effect.

An effect that is absent from $B \to X_s\gamma$, but of particular importance to the endpoint region in $B \to X_u l\nu_l$, are weak annihilation (WA) effects, which although entering at order Λ^2_{QCD}/m_b^2 in the OPE are enhanced by a numerical factor ($16\pi^2$). This effect resulting from four-quark operators, which are dimension-6, in the OPE, give a contribution to the endpoint of

$$-\frac{G_F^2 m_b^2|V_{ub}|^2}{12\pi} f_B^2 m_B (B_1 - B_2)\delta(1-y), \tag{2.40}$$

where f_B is the B meson decay constant and $B_{1,2}$ denote the matrix elements of the four-quark $V-A$ (vector - axial-vector) and $S-P$ (scalar - pseudoscalar) operators, O_{V-A} and O_{S-P} respectively, between B meson states, given by

$$\frac{1}{2}\langle B|O_{V-A}|B\rangle = \frac{f_B^2 m_B}{8} B_1, \quad \frac{1}{2}\langle B|O_{S-P}|B\rangle = \frac{f_B^2 m_B}{8} B_2. \tag{2.41}$$

If factorisation is valid, then $B_1 - B_2$ vanishes, for both charged ($B_{1,2} = 1$) and neutral ($B_{1,2} = 0$) B

mesons. A violation at the 10% level leads to an adjustment in the full rate of about 3%, which at the endpoint ($p_{\mathrm{cm}} > 2.2\,\mathrm{GeV}/c$) translates to a potential correction of $\pm 20\%$. Evidently, too large to ignore.

Unfortunately the quark-hadron duality concerns discussed in reference to the full rate, Γ, also contribute an uncertainty in the evaluation of $d\Gamma/dy$. The problem is of even greater concern here since the averaging over the resonances in the X_u system, which helps to validate the duality assumption, is severely limited in the endpoint region, as the region is believed to be dominated by the lowest mass X_u mesons (π and ρ). The B boost in the rest frame of the $\Upsilon(4S)$ provides some smearing which may help to alleviate the problem by populating the region with higher mass charmless mesons. The more of the spectrum that is sampled, the less of a problem it is thought to become. However, in general the uncertainty is unquantifiable.

The procedure for calculating spectral fractions and associated theoretical uncertainties will be discussed in more detail in chapter 6, where similar fits to those reported by CLEO are performed with the Belle measured photon energy spectrum.

2.4 Summary

The goal of an endpoint analysis of inclusive charmless B meson decays is the measurement of the CKM matrix element $|V_{ub}|$. As detailed in this chapter this requires much theoretical input.

Experimentally one proceeds from a measurement of the partial branching ratio in electron energy and extrapolates to the full branching ratio. Here there is a reliance on the information about the *Fermi motion*, which though better constrained from measurements of the photon energy spectrum, introduces significant uncertainty. This process is discussed in detail in chapter 6, where an attempt to assess it is made. After extrapolation, the full branching ratio is input into the V_{ub} extraction formula, which is given in equation 2.31. Here the effect of the dependence in the b quark mass occurs to the fifth power, and as such it's uncertainty is more dominant than that of the HQET-related parameters $\lambda_{1,2}$.

Chapter 3

The Belle experiment

The Belle experiment is run by a collaboration of more than 350 physicists from 54 institutes spanning 10 countries. It is conducted at the High Energy Accelerator Research Organisation (of Japan), known as KEK, which is located in Tsukuba, Japan. Its main goal is the study of CP asymmetry in B meson decays.

The many millions of B mesons needed for the study are produced by KEKB, one of only two aptly named B factories currently in operation. The other, PEP-II, is part of the Stanford Linear Accelerator Center (SLAC) and resides at Menlo Park, USA. Both collide electrons with positrons at asymmetric energies, providing a centre of mass energy best suited to producing the $\Upsilon(4S)$ resonance. The $\Upsilon(4S)$ resonance is a vector meson $b\bar{b}$ state.

The $\Upsilon(4S)$ decays via the strong force almost instantly to a $B\overline{B}$ meson pair. The colliding beam energy asymmetry causes the $\Upsilon(4S)$ to have a non-zero velocity in the laboratory frame. This boost is needed for the study of time-dependent CP asymmetries. Data from B meson decays at KEKB is gathered by the Belle detector, which surrounds the electron-positron (e^-e^+) collision point.

The KEKB accelerator commissioning began in December 1998, six months thereafter the Belle detector started logging data produced from B meson decays.

This chapter briefly describes the remarkable KEKB-Belle experimental apparatus, which makes the work of thesis possible.

3.1 The KEKB accelerator and storage ring

KEKB is a ring accelerator measuring 3 kilometres in circumference colliding electrons and positrons at a centre of mass energy of $10.58\,\mathrm{GeV}$. Electrons with energy $8.0\,\mathrm{GeV}$ and positrons with energy $3.5\,\mathrm{GeV}$ are stored in the High Energy Ring (HER) and Low Energy Ring (LER) respectively. The two rings continuously collide bunches of particles at the Interaction Point (IP). The IP is located in Tsukuba Hall - site of the Belle detector, see figure 3.1.

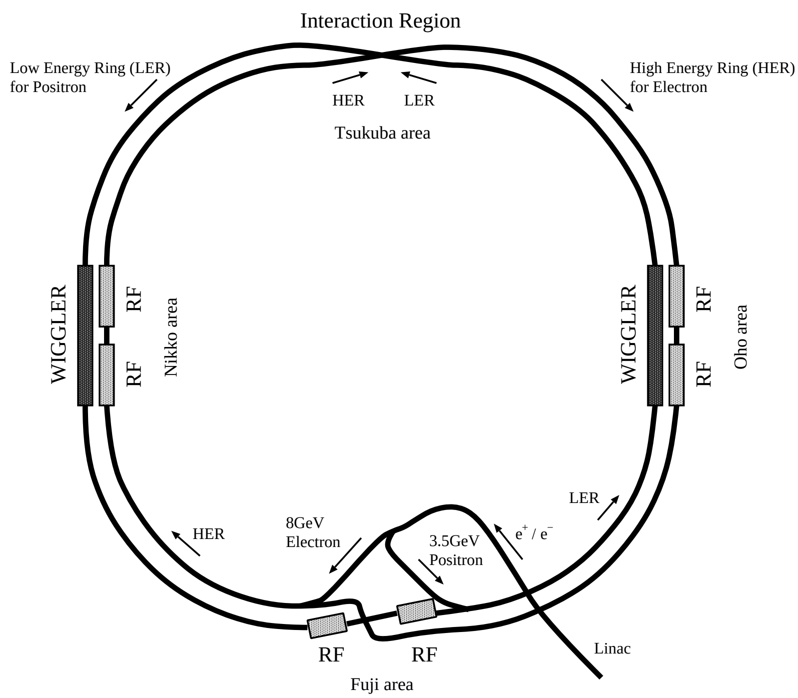

Figure 3.1: Configuration of the KEKB storage ring.

At the IP, electrons and positrons can annihilate to produce pure energy, which is available for matter production. Even though the centre of mass energy is tailored for $\Upsilon(4S)$ resonance production as illustrated in figure 3.2, only one in every seventy e^+e^- interactions produces an $\Upsilon(4S)$. Other processes that occur include Bhabha scattering, tau and muon pair production, lighter quark pair production and two-photon events.

Once created, the $\Upsilon(4S)$, moving in the laboratory frame with a boost $\beta\gamma = 0.425$, decays to B meson pairs with a branching fraction exceeding 96%. The rate of production, R, is defined as the interaction cross section, σ, multiplied by the luminosity, $\mathcal{L}$, measured in units of cm^2 and $\mathrm{cm}^{-2}\mathrm{s}^{-1}$ respectively.

$$R = \sigma\mathcal{L} \tag{3.1}$$

The interaction cross section for $\Upsilon(4S)$ production at the $\Upsilon(4S)$ resonance energy is

$$\sigma(e^+e^- \to b\bar{b}) = 1.1\,\mathrm{nb}, \tag{3.2}$$

where the unit barn, $\mathrm{b} \equiv 10^{-24}\mathrm{cm}^2$. The luminosity is a measure of the beam-colliding accelerator performance, and is given by

$$\mathcal{L} = fn\frac{N_1 N_2}{A}, \tag{3.3}$$

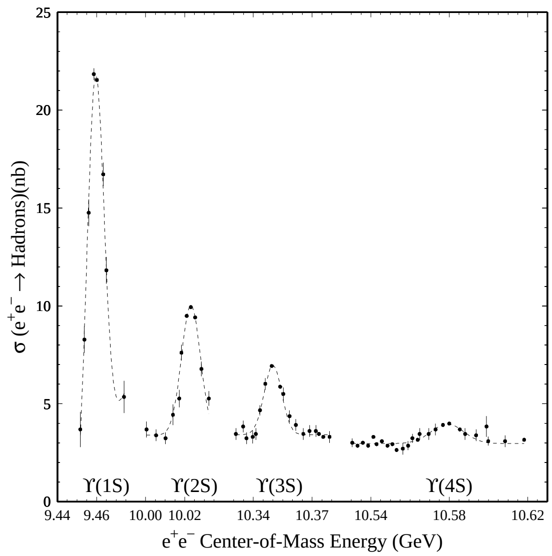

Figure 3.2: Cross section of Υ production in e^+e^- collisions.

where n bunches of N_1 and N_2 particles in opposing beams with overlapping area, A, meet f times per second. At KEKB the expression is re-parameterised as

$$\mathcal{L} = 2.17 \times 10^{34} \xi (1 + r) \frac{EI}{\beta_y^*}_{\pm}, \tag{3.4}$$

where:

ξ	$=$	beam–beam tune shift;
r	$=$	aspect ratio of the beam shape;
		where 1 corresponds to a circular beam and 0 to a flat beam;
E	$=$	beam energy in GeV;
I	$=$	the current stored in amps;
β_y^*	$=$	the vertical beta function at the IP in cm;

and the $\pm$ subscript implies that the current and energy parameters may be taken either from the High Energy Ring (HER) or Low Energy Ring (LER). To reduce background synchrotron radiation the beams collide at a finite crossing angle of $22\,\mathrm{mrad}$. The design specifications of KEKB are listed in table 3.1.

The KEKB accelerator team has already surpassed the design goal luminosity of $10^{34}\,\mathrm{cm}^{-2}\mathrm{s}^{-1}$. The current maximum, a world best[1], stands at $1.30\times10^{34}\,\mathrm{cm}^{-2}\mathrm{s}^{-1}$. $\mathcal{L}$ is an instantaneous quantity so therefore is not representative of the number of $\Upsilon(4S)$ decays recorded. At the time of writing the accumulated integrated luminosity amounted to over $200\,\mathrm{fb}^{-1}$. Equivalent to more than 220 million B meson pair

[1] As of May 20, 2004.

decays, it is the largest sample of its kind in the world.

		LER	HER	
Energy	E	3.5	8.0	GeV
Circumference	C	3016.26		m
Luminosity	$\mathcal{L}$	1×10^{34}		$\mathrm{cm}^{-2}\mathrm{s}^{-1}$
Crossing angle	θ_x	± 11		mrad
Tune shifts	ξ_x/ξ_y	$0.039/0.052$		
Beta function at IP	β_x^*/β_y^*	$0.33/0.01$		m
Beam current	I	2.6	1.1	A
Natural bunch length	σ_z	0.4		cm
Energy spread	σ_E/E	7.1×10^{-4}	6.7×10^{-4}	
Bunch spacing	s_B	0.59		m
Particles per bunch	N	3.3×10^{10}	1.4×10^{10}	
Emittance	$\varepsilon_x/\varepsilon_y$	$1.8 \times 10^{-8}/3.6 \times 10^{-10}$		m
Synchrotron tune	ν_s	$0.01 \sim 0.02$		
Betatron tune	ν_x/ν_y	$45.52/45.08$	$47.52/46.08$	
Momentum compaction factor	α_p	$1 \times 10^{-4} \sim 2 \times 10^{-4}$		
Energy loss per turn	U_0	$0.81^\dagger/1.5^\ddagger$	3.5	MeV
RF voltage	V_c	$5 \sim 10$	$10 \sim 20$	MV
RF frequency	f_{RF}	508.887		MHz
Harmonic number	h	5120		
Longitudinal damping time	τ_ε	$43^\dagger/23^\ddagger$	23	ms
Total beam power	P_b	$2.7^\dagger/4.5^\ddagger$	4.0	MW
Radiation power	P_{SR}	$2.1^\dagger/4.0^\ddagger$	3.8	MW
HOM power	P_{HOM}	0.57	0.15	MW
Bending radius	ρ	16.3	104.5	m
Length of bending magnet	l_B	0.915	5.86	m

†: without wigglers, ‡: with wigglers

Table 3.1: KEKB accelerator design parameters (from [32]).

3.2 The Belle detector

The Belle detector is configured within a $1.5\ \mathrm{T}$ superconducting solenoid and iron structure. It is located at the interaction region of the KEKB beams, and consists of seven sub-detectors, the; silicon vertex detector (SVD); central wire drift chamber (CDC); aerogel Čerenkov counters (ACC); time of flight counters (TOF); and an array of CsI(Tl) crystals (ECL); a pair of BGO crystal arrays (EFC); and multiple levels of resistive plate counters (KLM). The Belle detector is depicted in figure 3.3 on the facing page.

The SVD measures B meson decay vertices and aids the CDC in providing charged particle tracking. Specific ionisation energy loss measurements made with the CDC are combined with light yield readings from the ACC and time of flight information from the TOF to provide charged kaon and pion identification. Calorimetry and electromagnetic shower measurements, crucial for electron identification and photon

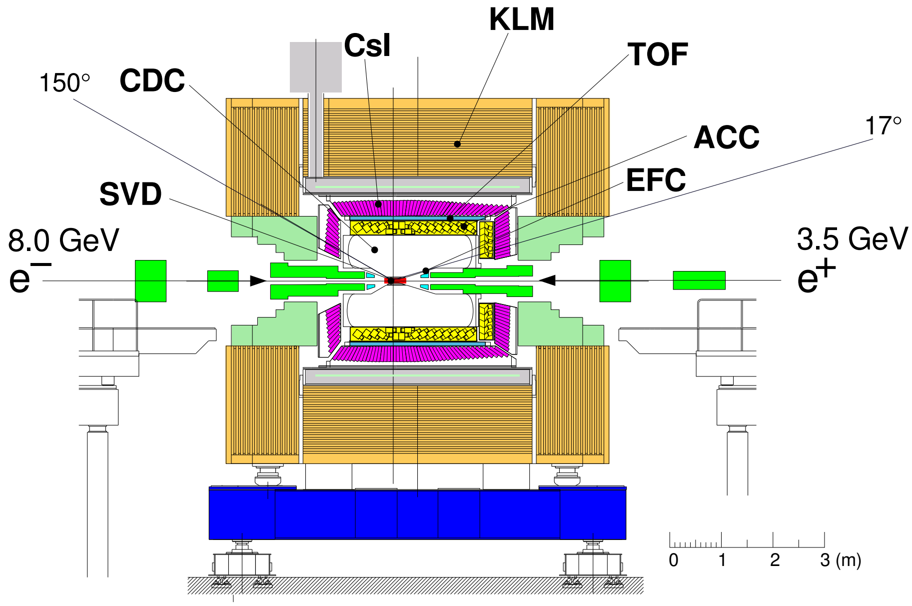

Figure 3.3: Side view of the Belle detector.

detection, are performed by the ECL and EFC. The KLM is used to identify muons and detect K_L mesons. The following subsections describe the Belle sub-detectors. The Belle detector is described in much detail elsewhere [33].

Depending on the context, Cartesian, spherical, and cylindrical coordinate systems are used in the description of the sub-detector components. For reference the z axis is defined as the direction of the magnetic field within the solenoid, which is anti-parallel to the positron beam. The x and y axes are aligned horizontally and vertically respectively, and correspond to a right-handed coordinate system. The polar angle, θ, is subtended from the positive z axis. The azimuthal angle, ϕ, subtended from the positive x axis, lies in the xy plane. The radius, defined in a cylindrical coordinate system, is measured from the origin in the xy plane, $r = \sqrt{x^2 + y^2}$. The origin is defined as the position of the nominal IP.

3.2.1 Beam Pipe

The beam pipe encloses the interaction point and maintains the accelerator vacuum. The determination of a B decay z-vertex is limited by multiple Coulomb scattering in the beam pipe and the distance from the IP to the Silicon Vertex Detector (SVD). Limiting the beam pipe proximity to the IP is the beam-induced heating in the pipe from which the SVD must be shielded.

These considerations are balanced to provide a central double-wall beryllium beam pipe extending from $z = -4.6$ cm to $z = 10.1$ cm with an inner radius of $r = 20$ mm. Helium gas is cycled through the gap between the inner and outer walls to provide cooling and its low Z minimises Coulomb interactions. The beam pipe is shown in figure 3.4.

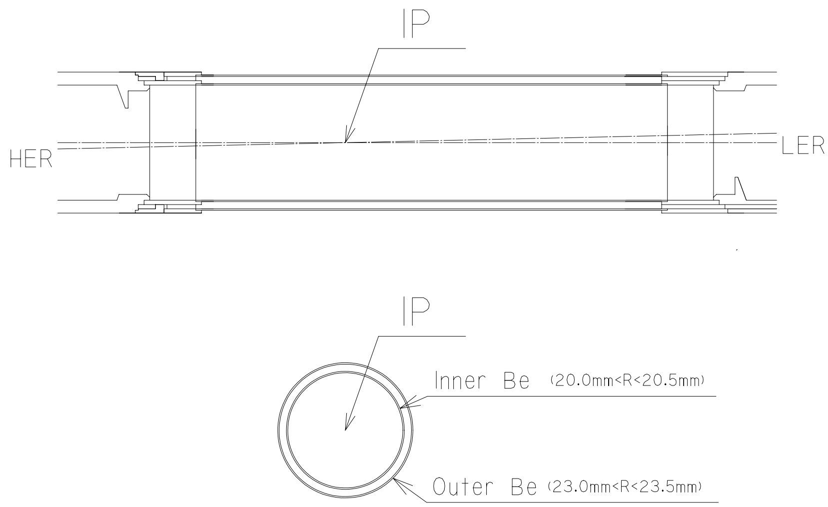

Figure 3.4: The cross section of the beryllium beam pipe at the IP.

3.2.2 Silicon Vertex Detector (SVD)

The $\Upsilon(4S)$ Lorentz boost in the laboratory frame allows measurement of the B meson decay vertices. The separation of the two B meson vertices, given the known boost, translates into a time difference between neutral B meson decays that is necessary for the measurement of time dependent CP violation in mixing. The SVD is able to resolve vertices to within a precision of $100\ \mu\mathrm{m}$.

The SVD works by registering the event of a charged particle passing through a Double Sided Silicon Detector (DSSD). At Belle this occurrence is known as a SVD hit. The SVD uses S6936 type DSSDs, fabricated by Hamamatsu Photonics.

The DSSD is essentially a *pn* junction, operated under reverse bias to reach full depletion. A charged particle passing through the junction liberates electrons from the valence band into the conduction band creating electron-hole (e^-h^+) pairs. The free e^-h^+ pairs instigate current in p$^+$ and n$^+$ strips situated along the surface of the bulk on opposing sides of the DSSD. The DSSD operation is depicted in figure 3.5.

Within the SVD the p$^+$ strips, with a pitch of $25\ \mu\mathrm{m}$, are aligned along the beam axis to measure the azimuthal angle, ϕ. The n$^+$ strips, with a pitch of $42\ \mu\mathrm{m}$, are aligned perpendicular to the beam axis to measure z.

A DSSD measures $57.5 \times 33.5 \times 0.3\ \mathrm{mm}^3$ and consists of 1280 sense strips and 640 readout pads on each side. Only every second sense strip is readout. The current on the strips is readout using a hybrid card. Either one or two DSSD's connected to a hybrid form a short or long half ladder (HL) respectively. Two half ladders connected together with the hybrids at the ends form a full ladder. Full ladders are arranged in

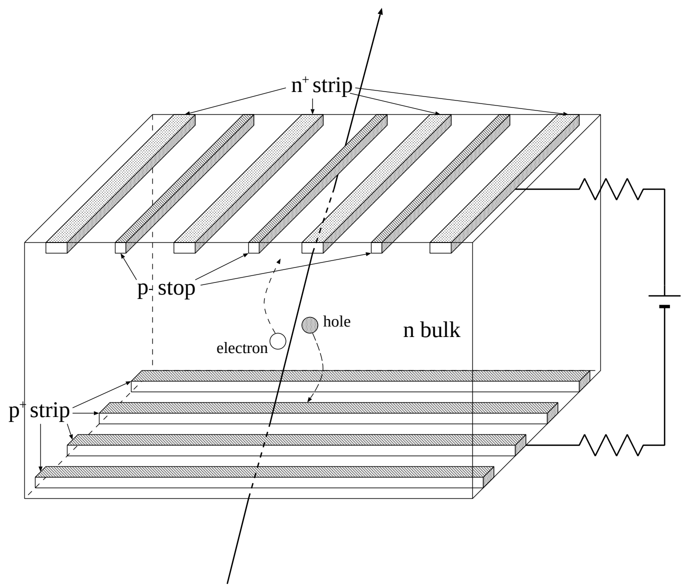

Figure 3.5: Schematic view of a Double Sided Silicon Detector.

cylindrical layers. The SVD consists of three such layers placed concentrically around the beam axis.

The inner layer, positioned at $r = 30$ mm, is made of 8 full ladders, where each is made from two short HLs. The middle layer, positioned at $r = 45.5$ mm, is made up of 10 full ladders, where each is made from a short and long HL. The outer layer positioned at $r = 60.5$ mm, is made up of 14 full ladders, where each is made from two long HLs.

The overall polar angle acceptance is $23° < \theta < 139°$, corresponding to 86% of the full solid angle. The SVD is shown in figure 3.6. Further detail on the SVD can be found in [34].

3.2.3 Central Drift Chamber (CDC)

The Central Drift Chamber (CDC) is designed to measure a charged particle's trajectory, known as it's track, as well as its specific ionisation energy loss, dE/dx. The track enables measurement of the particle's momentum while dE/dx is useful for identifying the particle's type. The CDC provides important trigger information.

The structure of the CDC is shown in figure 3.7. It consists of three geometrical sections, referred to as the cathode, the conical-shaped inner and toroidal-shaped outer. The CDC extends from a radius of 77 mm to 880 mm. It consists of 32 axial layers, 18 small angle stereo layers, and 3 cathode strip layers. Axial layers measure the $r - \phi$ position. Stereo layers, inclined at a small angle to the beam pipe, in conjunction with axial layers, measure the z position. The CDC covers a polar angle region of $17° \leq \theta \leq 150°$. The spatial resolution in $r - \phi$ is 130 μm, and is better than 2 mm in the z direction.

The CDC contains a total of 8400 drift cells. A drift cell is the functional unit of the CDC. It consists

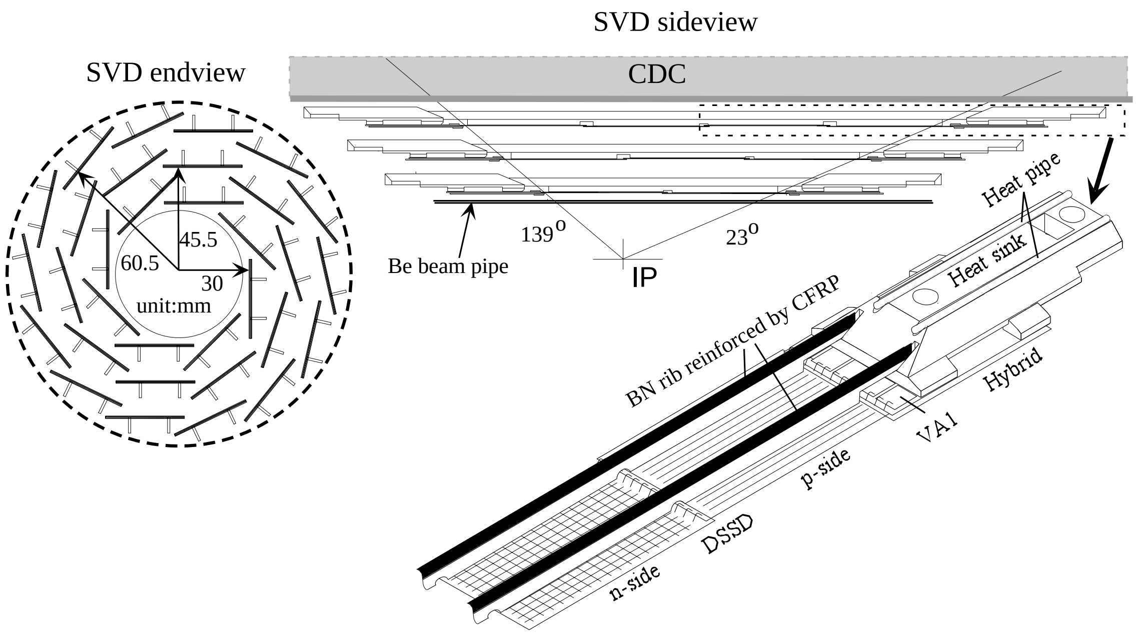

Figure 3.6: The Silicon Vertex Detector detector configuration.

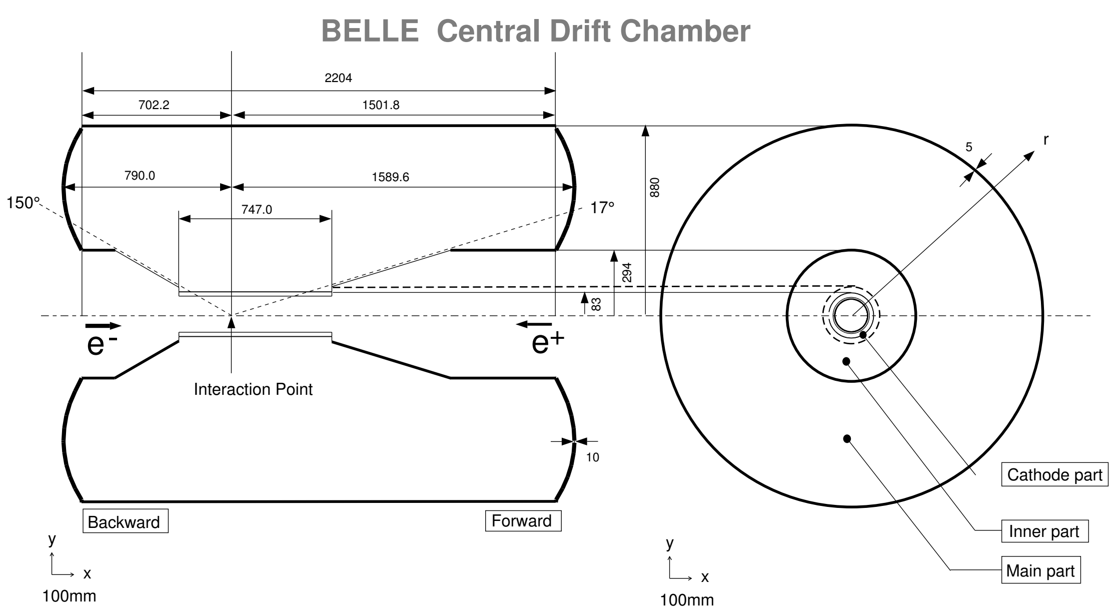

Figure 3.7: The Central Drift Chamber.

of a positively biased sense wire surrounded by six negatively biased field wires strung along the beam direction. The cells are immersed in a Helium-Ethane gas mixture of ratio 1:1.

The Helium-Ethane gas mixture has a relatively long radiation length of $640\,\mathrm{m}$, which minimises multiple Coulomb scattering's that affect the momentum resolution. The ethane component increases the electron density, which improves the ionisation energy loss measurement resolution.

A charged particle traversing the cell ionises the gas along its path. The ionised electrons and positive ions are attracted to the anode and cathode sense wires respectively. Their drift instigates further ionisation resulting in electron and positive ion avalanches. The avalanches induce current in the sense wire, a so-called CDC hit.

The time taken for the ionisation column to form is used to determine the distance between the ionising track and the sense wire. Track positions with respect to the sense wire are determined using a track segment finder which sorts hits into tracks. A helix, which describes the path of charged particle in a constant magnetic field, is fitted to the track. The helix parameters combined with the magnetic field strength determine the charged particle's momentum. The transverse momentum resolution, measured from cosmic ray data is

$$\frac{\sigma_{p_T}}{p_T} = \sqrt{(0.20 p_T)^2 + (0.29/\beta)^2}\%, \tag{3.5}$$

where p_T is in units of GeV/c and β is the velocity in units of the speed of light.

The hit amplitude recorded on the sense wire is used to determine the total energy of ionisation, and therefore a charged particle's energy loss due to ionisation, dE/dx, in the drift cell. Since the energy loss depends on a particle's velocity at a given momentum, dE/dx will vary according to particle mass, as shown in figure 3.8. The ionisation energy loss is measured for each CDC hit and measurements along the trajectory are combined to calculate the truncated mean, $\langle dE/dx\rangle$, of the track.

The $\langle dE/dx\rangle$ resolution, measured in a sample of pions from K_S decays, is 7.8%. The CDC can be used to distinguish pions from kaons of momenta up to $0.8\ \mathrm{GeV}/c$ with a 3σ separation. The CDC is described in detail elsewhere [35].

3.2.4 Aerogel Čerenkov Counter (ACC)

The silica Aerogel Čerenkov Counter (ACC) plays a crucial role in discriminating charged pions from kaons. When a particle travels faster than the speed of light in the medium in which it is traversing it will emit Čerenkov light. The light emitted appears in the form of a coherent wavefront at a fixed angle with respect to the trajectory.

For a given particle momenta and refractive index, n, of the medium it is traversing, the threshold energy for emitting Čerenkov photons is proportional to the particle's velocity. Selecting media with appropriate refractive indices allows for K/π discrimination. The ACC augments the other detector subsystems by performing excellent K/π separation for momenta between 2.5 and 3.5 GeV/c, and is also able to provide

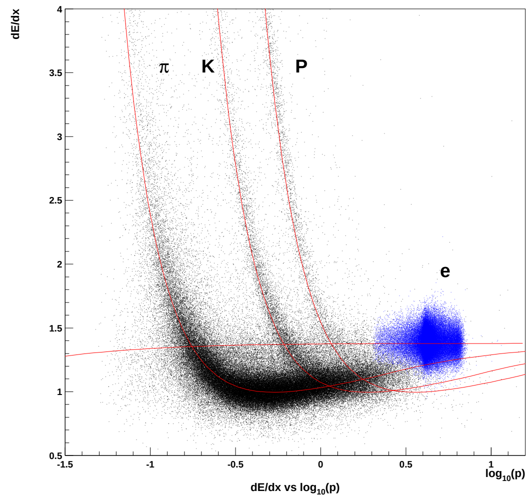

Figure 3.8: Truncated mean of dE/dx versus momentum. The points are measurements taken during accelerator operations, and the lines are the expected distributions for each particle type. p is measured in GeV/c.

useful information for momenta as low as 1.5 GeV/c and as high as 4.0 GeV/c.

The ACC is divided into barrel and forward endcap regions. It spans a polar angle region of $17° \leq \theta \leq 127°$. The barrel contains 960 counter modules segmented into 60 cells in the ϕ direction. The forward endcap contains 228 counter modules arranged into 5 concentric layers. Depending on the polar angle, the refractive index ranges from $n = 1.01$ to 1.03. The ACC is shown in figure 3.9.

To detect the light output, each counter is affixed to either one or two fine mesh-type photo-multiplier tubes (FM-PMT). Three different sizes of FM-PMT are used, with radii of 1, 1.25, and 1.5 inches. The choice, dependent on the refractive index, is motivated by the need for uniform response to $\beta \simeq 1$ velocity particles. A barrel and an endcap module are depicted in figure 3.10.

The pulse heights for each FM-PMT have been calibrated using μ-pair events. The average number of photoelectrons, $\langle N_{pe} \rangle$, is plotted for both barrel and endcap counters in figure 3.11. The light yield in units of photoelectrons ranges from 10 to 20 for the barrel ACC and from 25 to 30 for the end-cap ACC, which is high enough for K/π separation.

Since pions are the most ubiquitous particles in hadronic events, the ACC's performance is measured by it's ability to identify kaons amongst pions - for which the ACC can provide good K/π separation with a kaon efficiency of 73% and a pion-to-kaon fake rate of 7% [36], as demonstrated in figure 3.12. The ACC is described in detail elsewhere [37].

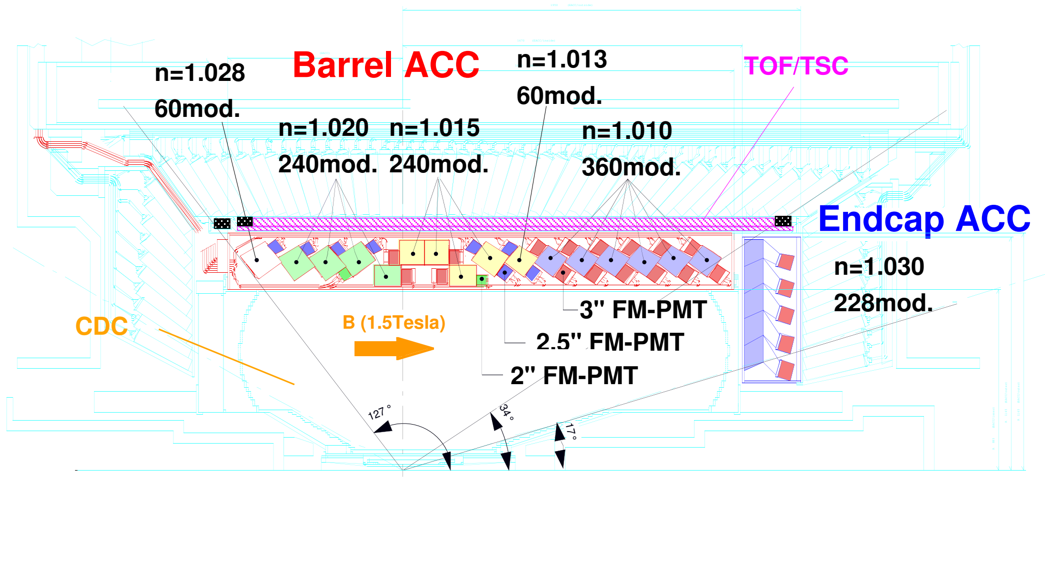

Figure 3.9: The configuration of the Aerogel Čerenkov Counter.

3.2.5 Time of Flight counter (TOF)

The Time of Flight counter (TOF) is used to measure the velocity of charged particles in an intermediate momentum range of $0.8\,\mathrm{GeV}/c$ to $1.2\ \mathrm{GeV}/c$. The velocity is measured by the particle's time of flight and the flight length. The latter is provided by the CDC's measurement of the track helix parameters. The velocity combined with the momentum (as provided by the CDC) determines the particle's mass and therefore type.

The TOF works on the principle of scintillation - the property of certain chemical compounds to emit short light pulses after excitation by the passage of charged particles or by photons of high energy. Scintillation is characterised by the light yield. The TOF measures the time of flight between a particle originating at the IP and passing through the scintillator.

The TOF system consists of 64 modules concentrically arranged at a radius of $1.2\ \mathrm{m}$. A module is made up of two trapezoid-ally shaped time-of-flight counters and one Trigger Scintillation Counter (TSC) separated by a radial gap of $1.5\ \mathrm{cm}$, as shown in figure 3.13. Scintillation light from a counter is collected by a fine-mesh-dynode photo-multiplier tube (FM-PMT). Two FM-PMTs are used for a TOF counter while only one is used for a TSC counter.

Time intervals are measured to within a precision of $100\ \mathrm{ps}$. The kaon-pion separation is plotted as a function of momentum in figure 3.14(a) on page 34, it shows better than 3σ separation for momenta below $1.0\ \mathrm{GeV}/c$. The mass distribution, shown in figure 3.14(b) on page 34, measured from hadronic events,

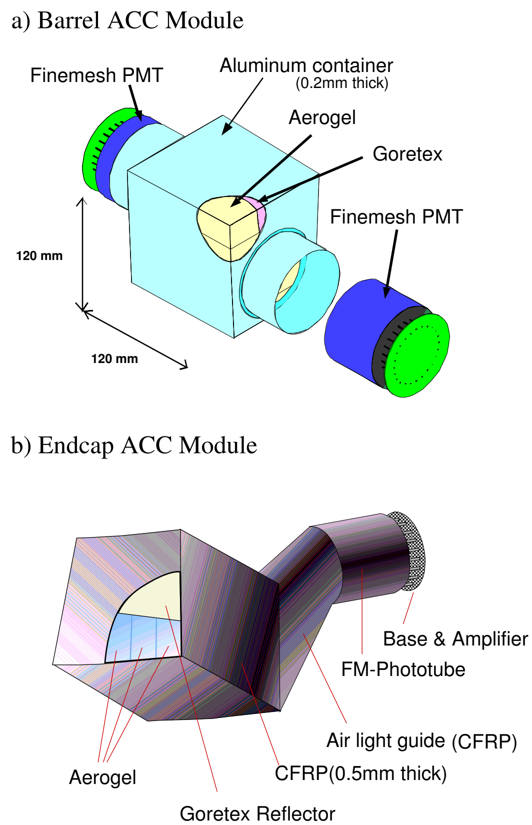

Figure 3.10: Schematic drawing of a typical ACC counter module: (a) barrel and (b) end-cap ACC.

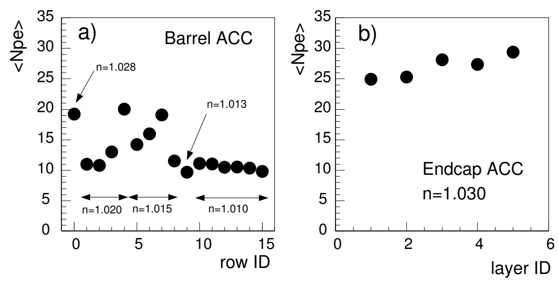

Figure 3.11: Average number of photoelectrons, $\langle N_{pe} \rangle$, for (a) each counter row in the barrel ACC and (b) each layer in the end-cap ACC.

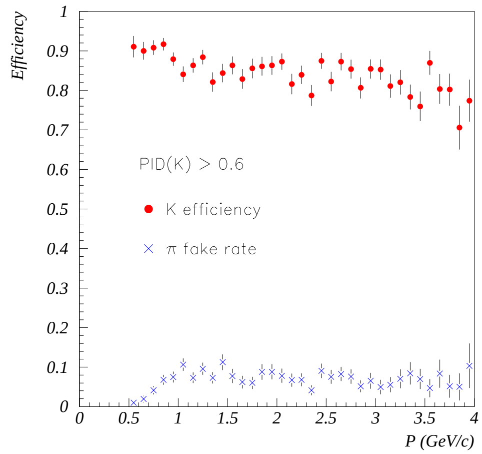

Figure 3.12: Kaon efficiency and pion fake rate, measured with $D^{*+} \to D^0(K\pi) + \pi^+$ decays, for the barrel region of the ACC.

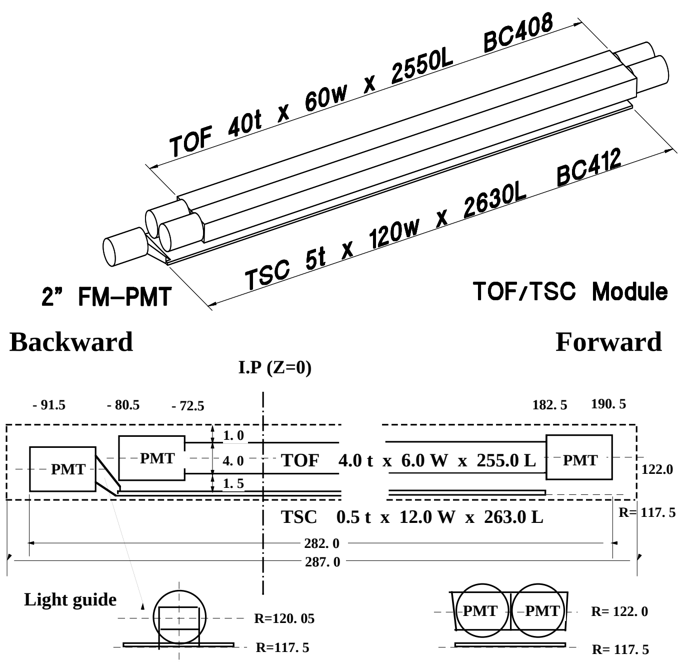

Figure 3.13: Dimensions of a TOF/TSC module.

shows a comparison of real data with Monte Carlo simulated with a timing resolution of $100\ \mathrm{ps}$. Clear peaks are evident for pions, kaons and protons. The TOF is described in detail elsewhere [38].

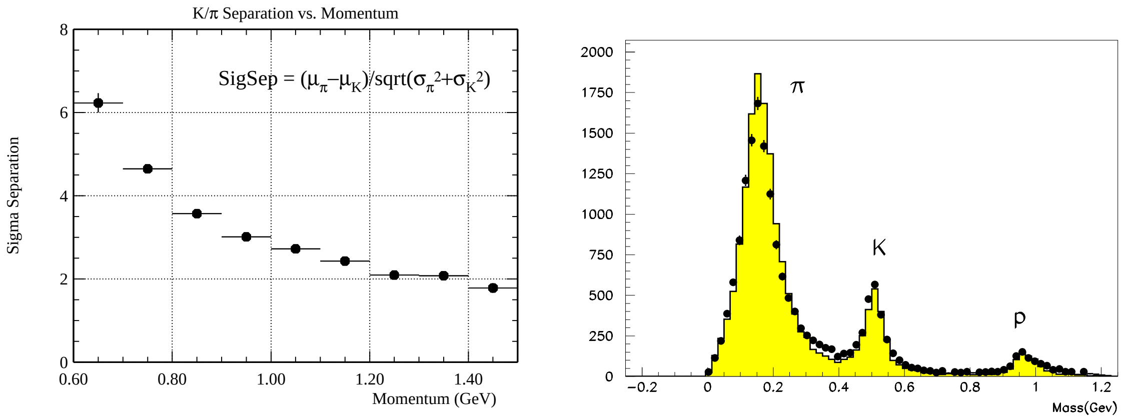

(a) K/π separation performance of the TOF as a function of momentum.

(b) Mass distribution from TOF measurements for particle momenta below $1.2\ \mathrm{GeV}/c$.

Figure 3.14: Time of Flight counter performance.

3.2.6 Electromagnetic Calorimeter (ECL)

The Electromagnetic Calorimeter (ECL) is designed to measure the energy and position of photons and electrons produced in Belle. It is crucial for electron identification and $\pi^0 \to \gamma\gamma$ reconstruction.

High energy electrons and photons entering the calorimeter instigate an electromagnetic shower through subsequent bremsstrahlung and electron pair production processes. A lateral shower shape ensues from Coulomb scattering. Eventually all of the incident energy appears as ionisation or excitation (light) in the absorbing material.

The ECL consists of a highly segmented array of 8,736 Cesium Iodide crystals doped with Thallium (CsI(Tl)). The Thallium shifts the excitation light into the visible spectrum. The light is detected by a pair of PIN photodiodes placed at the rear of each crystal.

The crystals are arranged into three sections: the backward endcap; the barrel; and the forward endcap. The barrel, positioned at an inner radius of $1.25\ \mathrm{m}$, is $3.0\ \mathrm{m}$ long, and spans the polar angle region, $32.2° \leq \theta \leq 128.7°$. The annular shaped forward endcap is situated at $z = +2.0\ \mathrm{m}$, and spans a polar angle region of $12.0° \leq \theta \leq 31.4°$. The likewise annular shaped endcap is situated at $z = -1.0\ \mathrm{m}$, and spans a polar angle region of $130.7° \leq \theta \leq 155.7°$. The ECL configuration is shown in figure 3.15 on the next page.

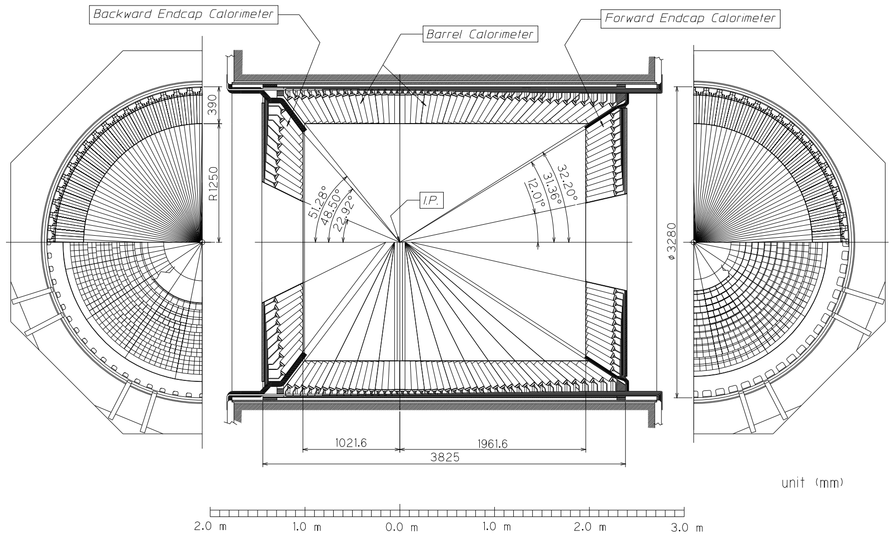

Figure 3.15: The Electromagnetic Calorimeter.

A crystal is typically $30\ \mathrm{cm}$ long, equivalent to 16.2 radiation lengths (X_0) for electrons and photons, and is chosen to minimise energy resolution deterioration at high energies due to the fluctuation of shower leakage at the back of the crystal. Furthermore, the crystals are designed such that a photon entering a particular crystal at its centre will deposit 80% of its energy in that crystal. A typical crystal in the barrel has a forward and backward face measuring $55\ \mathrm{mm} \times 55\ \mathrm{mm}$ and $65\ \mathrm{mm} \times 65\ \mathrm{mm}$ respectively. In the forward and backward endcaps the profiles vary from $44.5\ \mathrm{mm}$ to $70.8\ \mathrm{mm}$ and from $54\ \mathrm{mm}$ to $82\ \mathrm{mm}$ respectively. Each crystal possesses a tower like structure. In the barrel they are tilted at an angle of approximately $1.3°$ in the θ and ϕ directions to prevent particles escaping through gaps between crystals.

The ECL performs well over an energy range of $0.02 < E_\gamma/\mathrm{GeV} < 5.40$. It provides a measured energy resolution of

$$\left(\frac{\sigma_E}{E}\right) = \sqrt{1.34^2 + \left(\frac{0.066}{E}\right)^2 + \left(\frac{0.81}{E^{1/4}}\right)^2}\%, \tag{3.6}$$

and position resolution of

$$\sigma_{\mathrm{pos}} = \frac{0.5\ \mathrm{cm}}{\sqrt{E}}, \tag{3.7}$$

where E is measured in GeV. The ECL helps to distinguish pions from electrons since pions deposit much less of their energy in the crystal than do electrons, as illustrated in Figure 3.16 on the following page. The plot also shows the difference between the response of negatively and positively charged pions that is a direct result of their different nuclear cross sections. The rate of mis-identifting a pion as an electron is found to be less than 1% for momenta above $2\,\mathrm{GeV}/c$.

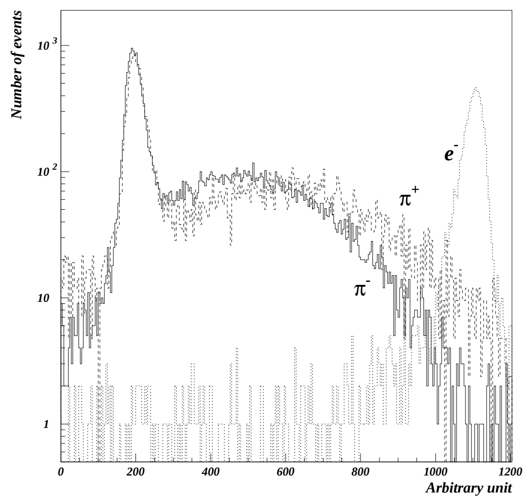

Figure 3.16: Distribution of the energy deposit by electrons (dotted line), by positive pions (dashed line) and by negative pions (solid line) at $1\,\mathrm{GeV}/c$.

3.2.7 K_L/μ Detector (KLM)

The K_L and μ detector (KLM) system was designed to identify K_L mesons and muons with high efficiency for momenta greater than $600\,\mathrm{MeV}/c$. Before reaching the KLM a K_L originating at the IP will typically traverse one interaction length,[2] most of which (0.8) is due to the ECL. When a K_L interacts with matter it produces a shower of ionising particles. The KLM instigates these showers by providing a minimum of 3.9 interaction lengths. The shower location determines the K_L flight direction. Fluctuations in the shower size prevent any useful measurement of the energy.

In contrast, muons of sufficient energy will pass all the way through the KLM since they do not feel the strong interaction or suffer Bremsstrahlung radiation loss. Therefore, any track matched with a particle penetrating several layers of the KLM is most likely a muon. Moreover, muons can be distinguished from charged hadrons, particularly $\pi^{\pm}$ and $K^{\pm}$, since on average they suffer smaller deflections.

The KLM consists of alternating layers of charged particle detectors and $4.7\,\mathrm{cm}$ thick iron plates. The barrel region is octagonally shaped and is made of 15 detector layers and 14 iron layers. The forward and backward endcaps contain 14 detector layers each.

A detector layer is a super layer of two glass-electrode Resitive Plate Counters (RPC) modules interspersed between high voltage biased plates, insulators and external pickup strips as shown in figure 3.17. Figures 3.18(a) and 3.18(b) show barrel and endcap RPCs respectively.

An ionising particle traversing the gas filled gap in the single layer RPC initiates a streamer in the gas

[2] The interaction length is the mean free path of the particle before undergoing an inelastic interaction.

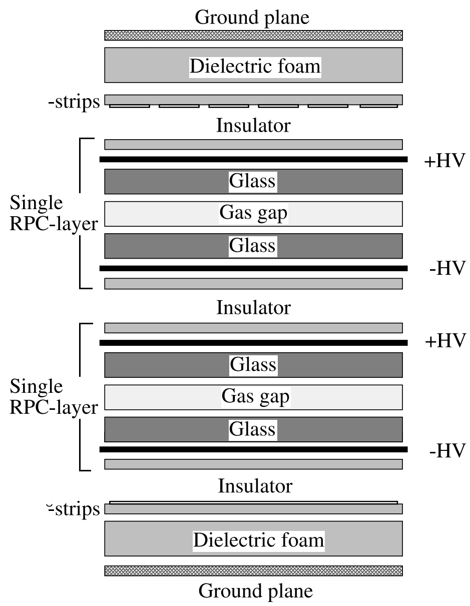

Figure 3.17: Cross section of a KLM superlayer.

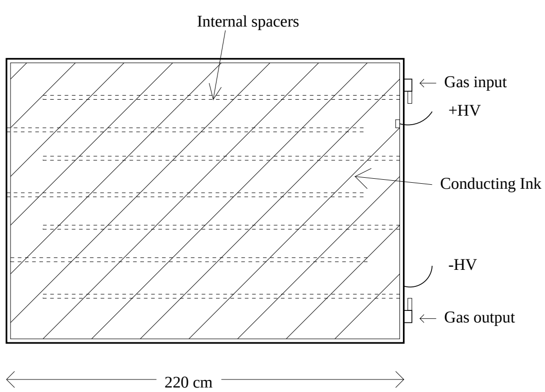

(a) Barrel RPC.

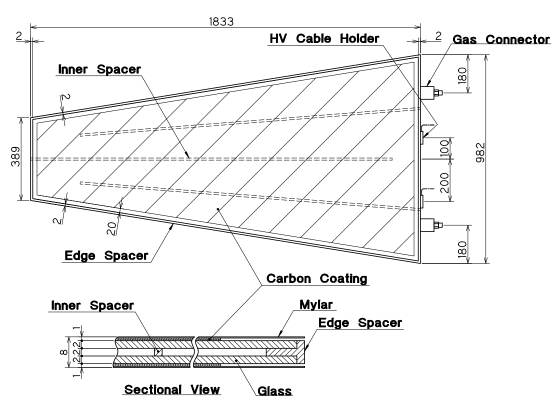

(b) Endcap RPC.

Figure 3.18: KLM RPCs.

that results in a local discharge of the plates. The discharge induces a signal on the external orthogonal pickup strips located above and below the pair of RPCs.

The pickup strips, typically $5\ \mathrm{cm}$ wide, provide $\phi - z$ and $\theta - \phi$ information in the barrel and endcap regions respectively. The barrel and endcaps contain 240 and 122 RPC modules each respectively. The polar angular coverage is $20^\circ < \theta < 155^\circ$. The KLM angular resolution from the IP is better than $10\,\mathrm{mrad}$. For momenta above $1.5\ \mathrm{GeV}/c$ the muon identification efficiency is greater than 90% with a mis-identification rate of less than 5%. The KLM is described in detail elsewhere [39].

3.2.8 Solenoid Magnet

A superconducting solenoid provides a magnetic field of $1.5\ \mathrm{T}$ in a cylindrical volume $3.4\ \mathrm{m}$ in diameter and $4.4\ \mathrm{m}$ in length. The solenoid encases all the sub-detectors up to the KLM. The iron structure of the Belle detector serves as the return path of magnetic flux and an absorber material for the KLM. The solenoid details are shown in table 3.2. The results of the magnetic field mapping made with accelerator final-focus quadrapole magnets located within the solenoid, QCS-R and QCS-L are shown in Fig 3.19.

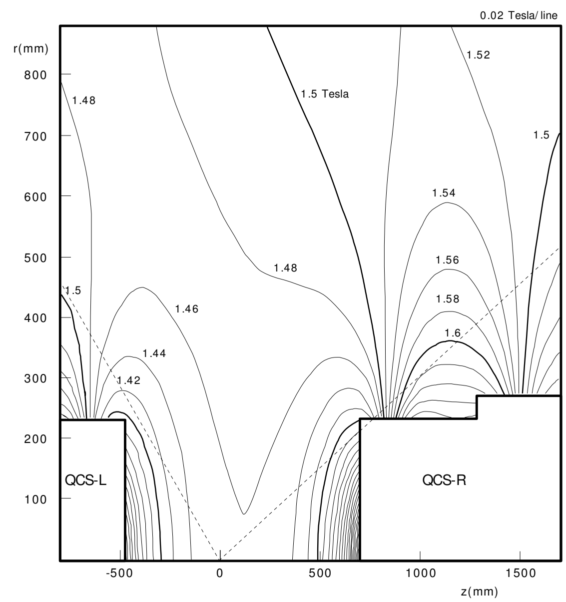

Figure 3.19: Contour plot of the measured magnetic field in the Belle detector.

3.2.9 Extreme Forward Calorimeter (EFC)

The Extreme Forward Calorimeter (EFC) extends the range of electron and photon calorimetry to the extreme forward and backward regions, defined as $6.4^\circ < \theta < 11.5^\circ$ and $163.3^\circ < \theta < 171.2^\circ$ respectively. The EFC is placed on the front faces of the KEKB accelerator compensation solenoid magnet cryostats,

Cryostat		
	Inner Radius	1.70 m
	Outer Radius	2.00 m
Central field		1.5 T
Length		4.41 m
Coil		
	Effective radius	1.8 m
	Length	3.92 m
	Superconductor	NbTi/Cu
	Nominal current	4400 A
	Inductance	3.6 H
	Stored energy	35 MJ
	Typical charging time	0.5 h

Table 3.2: Parameters of the solenoid coil.

surrounding the beam pipe. It shields the CDC from beam related backgrounds and synchrotron radiation. The EFC is also used as a beam monitor and luminosity meter for KEKB control.

The EFC is constructed from crystals of Bismuth Germanate (BGO), which was chosen for its ability to withstand radiation doses at the megarad level whilst still providing good energy resolution. The detector is segmented into 32 azimuthal and 5 polar sections for both backward and forward cones.

Each crystal is tower shaped and is aligned to point towards the IP. The arrangement is illustrated in Fig 3.20.

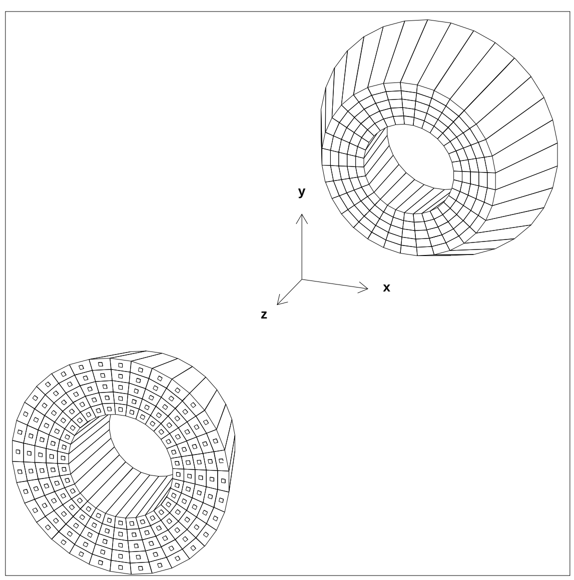

Figure 3.20: An isometric view of the BGO crystals of the forward and backward EFC detectors.

3.3 Trigger and Data Acquisition System

The trigger as its name suggests, triggers acquisition and storage of data from the Belle detector. The trigger decision is based on the need to keep physics events of interest while minimising the many uninteresting beam-related background events.

At an instantaneous luminosity of $10^{34}\mathrm{cm}^{-2}\mathrm{s}^{-1}$ the trigger rate for physics events of interest is around 100 Hz and the typical operating rate is 350 Hz. The Belle trigger can handle rates as high as 500 Hz.

Physics of interest includes hadronic, Bhabha, μ-pair, τ-pair and two photon events. Beam related backgrounds result from interactions of spent electrons and positrons with the beam pipe and the residual gas molecules therein. Since beam backgrounds depend on the accelerator operating conditions, their levels cannot be well estimated, so the trigger is designed to cope with large levels of backgrounds. In order to or not to trigger on these varying event characteristics, information is utilised from each of the sub-detectors.

The trigger is arranged into four levels, denoted as level 0, 1, 3 and 4 respectively.[3]

The level 0 trigger (L0) is a prompt timing signal from the TOF which forces the SVD into the HOLD state.

The level 1 trigger (L1) is implemented in hardware. It is made up of sub-detector triggers which feed the Global Decision Logic (GDL). The GDL sources information from all sub-detectors bar the SVD. All triggers, processed in parallel, are used by the GDL to characterise the event type. The CDC provides $r-\phi$ and $r-z$ track trigger signals. The TOF trigger system provides an event timing signal and delivers information on the hit multiplicity and topology. The ECL provides two complementary triggers based on total energy deposition and cluster multiplicity, each sensitive to different types of hadronic events. The KLM provides a high efficiency trigger for muon tracks. When available the trigger timing is provided by the TOF, otherwise the ECL is used. The Level 1 trigger configuration is depicted in Fig. 3.21 on the next page. To keep hadronic events the GDL typically relies on three main trigger classes; multi-tracks, energy sums and isolated cluster counts. Each provide more than 96% efficiency for hadronic events individually, combined the efficiency is 99.5%.

The level 3 trigger (L3) is implemented in software in an online computer farm. Using an ultra-fast track finder it requires at least one track with an impact parameter in z less than $5.0\ \mathrm{cm}$ and the total energy deposit in the ECL to be greater than $3.0\ \mathrm{GeV}$. The trigger has the effect of retaining physics events of interest with a 99% efficiency while reducing overall event rates by $50 \sim 60$%.

The level 4 trigger (L4) is implemented in software and performed in an offline computer farm just prior to full event reconstruction. Any one of the four conditions listed below can enact the trigger.

- Certain L1 trigger bits are set. These are saved for use by sub-detector groups;

[3] A level 2 trigger is not implemented at Belle.

- A total ECL energy deposit of less than $4\,\mathrm{GeV}/c$. To reduce background from cosmic rays, this is vetoed by events with coincident KLM and ECL hits as encoded in L1 trigger information;
- At least one track with an impact parameter in r and $|z|$ less than $1.0\,\mathrm{cm}$ and $4.0\,\mathrm{cm}$ respectively, and $p_T > 300\,\mathrm{MeV}$;
- 1% of events not satisfying any of the above criteria are used for monitoring purposes.

The criteria retain hadronic events with an efficiency of 99.8% while reducing the total event trigger rate by around 73%.

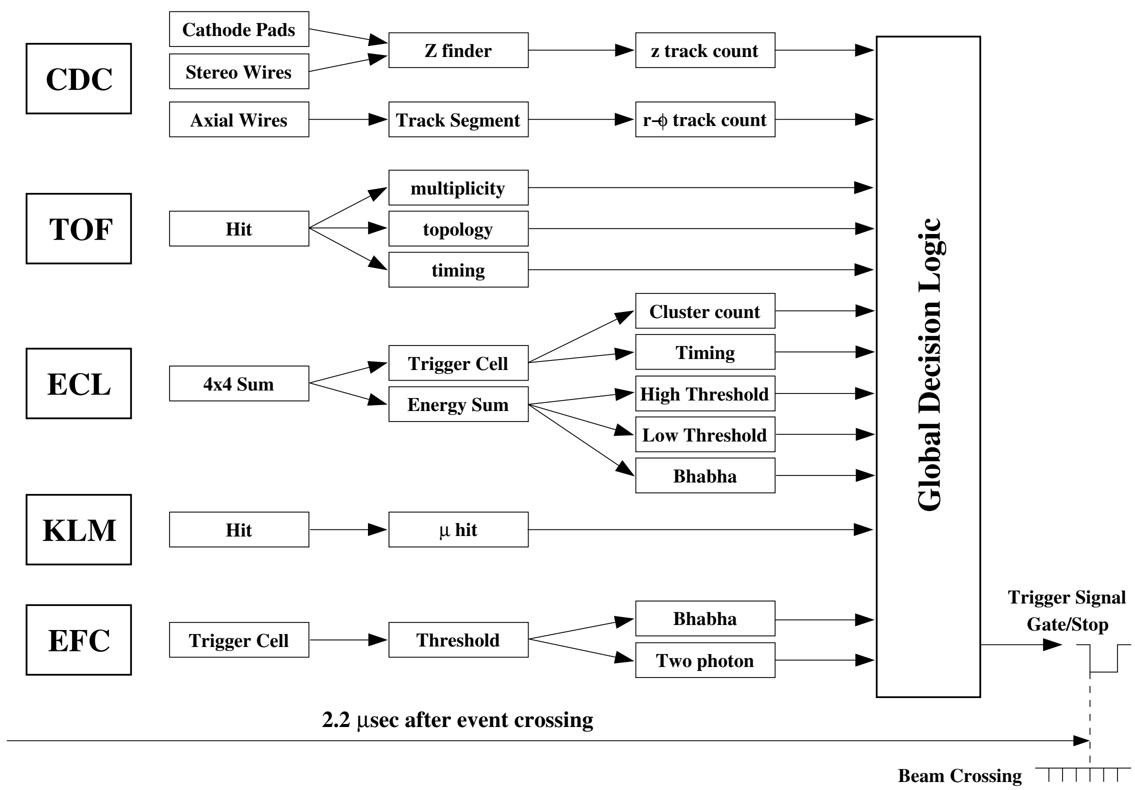

Figure 3.21: The Level-1 trigger system.

The Data Acquistion (DAQ) system is designed to have a deadtime of less than 10% at a trigger rate of 500 Hz. The system is shown in figure 3.22. The data from each sub-detector is readout upon receiving the L1 trigger. The data are combined into a signal event record by the event builder. The event records are processed by an online computer farm which changes the event record into an offline format after which it is filtered through the L3 trigger. A fraction of these events are fed to the data monitoring system which updates histograms that can be checked offline by expert operators. All of the data is then sent to the KEK computer centre where it is written to tapes and stored in a tape-library. A hadronic event typically occupies

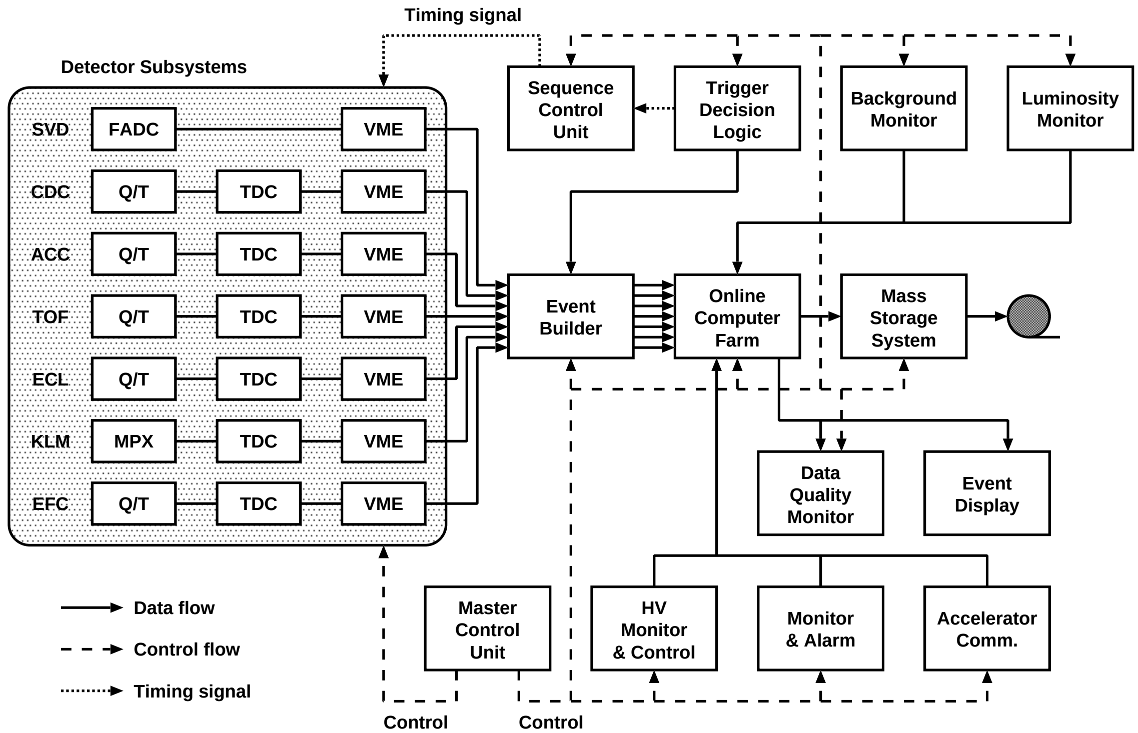

Figure 3.22: The Belle DAQ system.

30 kBytes of storage space, corresponding to a maximum data transfer rate of 15 MBytes per second when operating at the maximum trigger rate (500 Hz).

After data is written to tape it is eventually processed by an offline computer farm which filters events through the L4 trigger. Here the data undergoes full event reconstruction, whereby it is translated into a Data Summary Tape (DST) format. A DST is made up of higher level data structures which contain objects of interest to physicists, for example 4-vectors of position and momentum.

Further analysis filters events into hadronic, Bhabha, τ-pair, μ-pair and two-photon event skims. The skims are saved into mini data summary tape (MDST) files. The MDST is a subset of the DST, which contains the data needed for physics analyses.

3.4 Simulation

Simulation requires two key components: an event generator; and the detector response simulator. An event generator creates a list of particles created from e^+e^- interactions as well as from subsequent decays of unstable particles. This list includes the position and momentum four vectors of the particles at the time of their creation.

Belle employs the `QQ98` [40] event generator to generate $\Upsilon(4S)$ decay events. `QQ98` generates and decays particles according to a decay table. The decay table specifies the decay models, modes, branching fractions, lifetimes etc. of all possible particles involved in the decay of the $\Upsilon(4S)$ and subsequent decays. This sequence is commonly referred to as a decay chain. The information in the table is composed from world averages. Hadronic continuum events, namely $e^+e^- \to q\bar{q}$ interactions where $q = (u, d, s, c)$ is the quark flavour, are generated using JETSET [41] which is based on the LUND string fragmentation model [42].

The Belle collaboration also uses the event generator, `EvtGen`[43]. One advantage it offers over `QQ98` is that decay amplitudes instead of probabilities are used for the simulation of decays. The framework uses the amplitude for each branch in the decay tree to simulate the entire decay chain.

The generated list of particles are passed to modules which propagate and simulate the particle interactions with the detector. These engage `GEANT`[44] to model the geometry of the detector and particle interactions with matter. Collectively all the detector simulator modules are known as GSIM (as in `GEANT`-based simulator). GSIM is continually updated with information gathered from studies of the detector response to real data as well with measured experimental conditions, such as the beam dependant IP.

`QQ98` and GSIM both make use of random number generation to choose among possible outcomes and as such the data produced is referred to as Monte Carlo data, or MC for short.

This work uses events generated by both `QQ98` and `EvtGen`. Where appropriate the details of their use is discussed.

Chapter 4

Reconstruction

4.1 Preliminaries

This analysis investigates the momentum spectrum of electrons and positrons to measure the rate of inclusive charmless semileptonic B meson decays. From this point references to 'electrons' includes both electrons and positrons.

An inclusive analysis, such as this one, benefits from high statistics but suffers from large backgrounds. Typically, the selection criteria are chosen to minimise the error in the signal yield. However, this approach does not translate to a $|V_{ub}|$ measurement with minimal uncertainty since theoretical uncertainties play a major role as well. Nowhere is this more relevant than in deciding which momentum interval to use to extract $|V_{ub}|$.

Measurements of $|V_{ub}|$ in multiple momentum intervals are advantageous since they detail the behaviour of all the uncertainties as a function of the momentum and provide consistency checks. A measurement in an interval that avoids the charmed background encounters a large theoretical uncertainty. Measurement in an interval below the kinematic endpoint suffers from less theoretical uncertainty, but at the cost of larger experimental uncertainty.

The CLEO endpoint analysis extracted $|V_{ub}|$ values in five momentum intervals, beginning at a lower cutoff of $2.0\,\mathrm{GeV}/c$ and going up to $2.4\,\mathrm{GeV}/c$ in steps of $0.1\,\mathrm{GeV}/c$, with the higher cutoff fixed at $2.6\,\mathrm{GeV}/c$ [14]. The $|V_{ub}|$ value they quote was measured in the interval, $2.2 < p_{\mathrm{cm}}/\mathrm{GeV}/c < 2.6$, and was a compromise between the two extremes of theoretical and experimental uncertainties. Similarly, multiple measurements are performed in this analysis. This analysis repeats the approach adopted by CLEO, but includes an additional momentum interval for study, $1.9 < p_{\mathrm{cm}}/\mathrm{GeV}/c < 2.6$. The "cm" refers to the centre of mass system, which is equivalent to the rest frame of the $\Upsilon(4S)$.

This chapter describes the data set used, the criteria for selecting signal electron candidates, and the resultant signal reconstruction efficiency. Based on CLEO's measurement, the selection criteria are optimised for the momentum interval $2.2 < p_{\mathrm{cm}}/\mathrm{GeV}/c < 2.6$, although they are expected to perform equally well for other intervals. Hereafter this interval is referred to as the signal region.

4.2 Data Set

4.2.1 Experimental data

The analysis is performed on data collected by the Belle detector from January 2000 to July 2002. During this period Belle accumulated $78.13\,\mathrm{fb}^{-1}$ and $8.83\,\mathrm{fb}^{-1}$ integrated luminosity samples taken at (ON), and 60 MeV below (OFF), the $\Upsilon(4S)$ resonance energy, respectively. The rate at which this data set was collected is shown in figure 4.1.

At Belle, data can be further subdivided into experiment and run numbers. Experiments, denoted by odd numbers, differ, reflecting slight changes in accelerator conditions made over time. Within an experiment, a run represents an interval of smooth data acquisition. Ideally one run corresponds to a single beam fill. However, if any DAQ errors interrupt data taking there may be more than one run per fill.

This analysis uses:

- a subset of the ON sample, inclusive of experiment 13 run 1200 through to experiment 17, amounting to $27.9\,\mathrm{fb}^{-1}$ of integrated luminosity; and

- the full OFF sample of experiments 7 to 19 inclusive, amounting to $8.83\,\mathrm{fb}^{-1}$ of integrated luminosity.

The ON and OFF data subsets were originally chosen on the basis of consistency in detector and accelerator conditions, which was monitored using the di-muon to di-electron event ratio (Figure 4.2). The OFF data subset was later extended to a large data subset to take advantage of the increase in statistics of the full OFF resonance data sample (inclusive of experiment 7 to experiment 19), since the OFF sample limits our statistical sensitivity. While accelerator conditions vary between experiments and runs, they do not do so to such an extent as to invalidate the practice of using ON and OFF data from different experiments. Using a larger ON resonance sample was considered but was deemed unnecessary since the CLEO analysis showed[14] that the experimental uncertainties in the momentum bins that would benefit from more ON data were dominated by systematic uncertainties. The effects of the chosen data sample will be revisited later.

4.2.2 Monte Carlo data

Monte Carlo (MC) simulated signal and background events are essential for the choice and optimisation of cuts. The signal MC is also used to measure the signal reconstruction efficiency. The Belle collaboration generates large amounts of MC data of several types with variations to account for different experimental

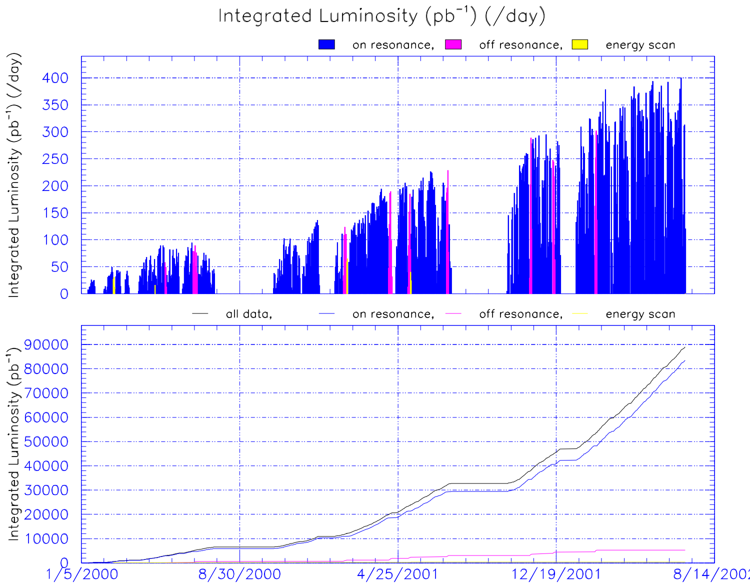

Figure 4.1: Integrated luminosity: per day (top) and as a function of day (bottom).

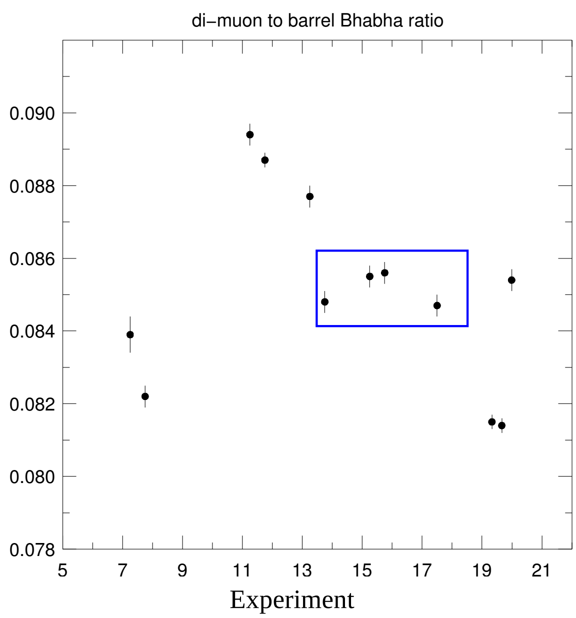

Figure 4.2: Ratio of di-muon to di-electron events as a function experiment number and run range. The blue box highlights the experiment and run range chosen for the feasibility study (mentioned in the text), it highlights consistency in the performance of the accelerator and detector.

conditions. Aside from collaboration wide samples, users also have some capacity to produce relatively small samples suited to their individual analyses.

Signal Monte Carlo

A very large $B \to X_u l\nu_l$ MC sample was produced by Belle for studies of charmless semileptonic B meson decays. These decays were created by the `EvtGen` event generator [43]. In any given event in the sample only one of the two B mesons will decay via $B \to X_u l\nu$ (signal). The sample incorporates world average branching ratios for $B \to \pi l\nu_l$, $B \to \rho l\nu_l$ and the total inclusive rate, $B \to X_u l\nu_l$ [17]. The sample consists almost entirely of ISGW2 [45] modelled exclusive charmless semileptonic B meson decays. A small inclusive component, conforming to the De Fazio and Neubert prescription (DFN) [25], is included to account for the slight deficit in the sum of exclusive rates compared with the full inclusive rate.

ISGW2 is a model describing the dynamics of semileptonic B meson decay to exclusive meson states. The hadronic matrix element can be parameterised into an expression involving the available four-vectors in the decay and form factors (functions of Lorentz scalars). For the case of a pseudoscalar light meson, M, in the decay $\bar{B} \to M l\nu_l$, the hadronic matrix element takes the Lorentz covariant form

$$H_\mu = \langle M|\bar{u}P_L b|\bar{B}\rangle = f_+(q^2)(p_B + p_H)_\mu + f_-(q^2)(p_B - p_H)_\mu, \tag{4.1}$$

where $f_\pm$ are the form factors, and q^2 is the squared mass of the virtual W boson. Three independent form factors, typically denoted: $A_1(q^2)$; $A_2(q^2)$; and $V(q^2)$, are needed for a vector meson final state, since the meson's polarisation four-vector is available to construct additional terms. The ISGW2 authors compute normalisation and functional forms of the form factors by modelling the meson as a quark pair located in a Coulomb plus linear interaction potential. Estimated meson wave functions allow the form factor normalisation and slope to be computed at the point of zero-recoil, $q^2 = q^2_{\max}$. Values at lower q^2 are extrapolated from $q^2_{\max}$ assuming an exponential form.

ISGW2 form factors are only computed for mesons with masses less than $1.7\,\mathrm{GeV}/c^2$, therefore, in neglecting possible contributions from higher mass states it does not provide a complete description of the full $B \to X_u l\nu_l$ rate. However, it is believed to be adequate for the high momentum regions since these are dominated by the lighter mass meson states.

Inclusive $B \to X_u l\nu$ decays are simulated based on the De Fazio and Neubert prescription[25], which is described in section 2.3.1. They derive an expression for the triple differential decay correct to next-to-leading order ($\mathcal{O}(\alpha_s)$) that includes the effect of the b-quark's *Fermi motion*. The *Fermi motion* is encoded into the shape function, which is parameterised by the b-quark pole mass, m_b, and the average momentum squared of the b-quark inside the B meson, μ_π^2. The exponential model is assumed for the shape function. The parameters are set as $m_b = 4.80\,\mathrm{GeV}/c^2$ and $\mu_\pi^2 = 0.30\,\mathrm{GeV}^2/c^2$, which are derived from CLEO measurements of inclusive $B \to X_c l\nu$ recoil mass and $B \to X_s\gamma$ photon energy spectra moments[29, 46], but the evaluation differs from that of CLEO in that terms proportional to $1/m_b^3$ and α_s^2 have been removed from the relation between measured observables and the parameters m_b and μ_π^2.

A mainly inclusive hybrid sample was also generated for study in this analysis. It contains the ISGW2 modelled $B \to \pi l \nu_l$ decay and a large inclusive component, implemented in the same way as described above with $m_b = 4.80\,\mathrm{GeV}/c^2$ and $\mu_\pi^2 = 0.30\,\mathrm{GeV}^2/c^2$. Further, four similar samples are generated with $(m_b/(\mathrm{GeV}/c^2), \mu_\pi^2/(\mathrm{GeV}^2/c^2)) = \{(4.92, 0.30), (4.78, 0.30), (4.80, 0.19), (4.80, 0.41)\}$, which, by incorporating upward and downward fluctuations in the parameters as determined by their uncertainties, are used to investigate model dependence in the efficiency.

Electron momentum spectra for each of the signal MC sets are shown in figure 4.3.[1]

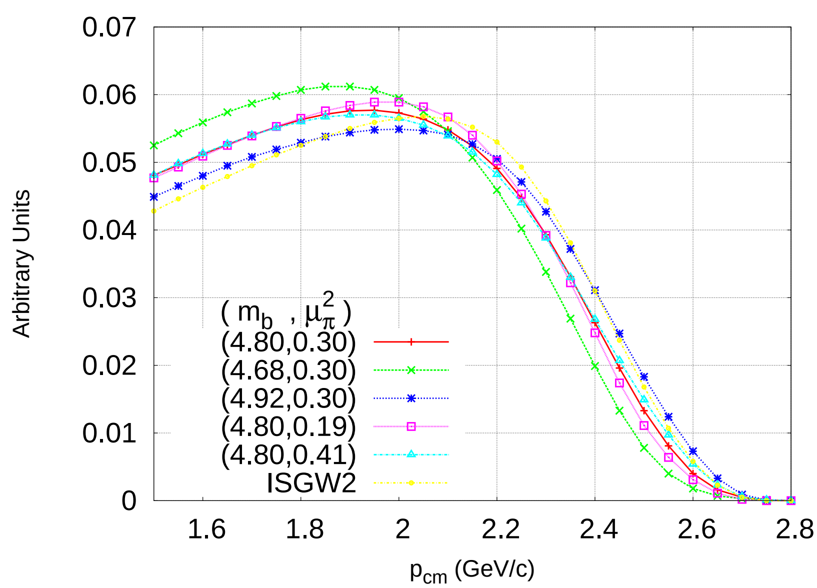

Figure 4.3: Electron momentum spectrum for signal MC sets.

Background Monte Carlo

The Belle collaboration using `QQ98` generates large MC event samples that are split into four different types [40]:

mixed $e^+e^- \to \Upsilon(4S) \to B^0\overline{B}^0$, which includes the effect of neutral B meson mixing;

charged $e^+e^- \to \Upsilon(4S) \to B^+B^-$;

charm $e^+e^- \to c\bar{c}$;

[1]The presence of the $B \to \pi l \nu_l$ is implied in the mainly inclusive samples. Likewise the presence of the small inclusive component is implied in the mainly ISGW2 modelled exclusive sample, hereafter, referred to as the “ISGW2” sample.

uds $e^+e^- \to u\bar{u}, d\bar{d}, s\bar{s}$.

These samples include experiment and run dependent beam-related backgrounds derived from randomly triggered events in the data. The mixed and charged samples, which do not contain any signal decays, contain all the $B\overline{B}$ backgrounds, namely charmed semileptonic B meson decays, secondary electrons from charmed mesons and tau leptons, and electron fakes from hadrons. The mixed and charged samples are used to calculate the $B\overline{B}$ background. The "mixed" and "charged" samples are appropriately combined to form the $B\overline{B}$ MC sample. The "charm" and "uds" samples are likewise appropriately combined to form the hadronic continuum MC sample.

4.2.3 ON to OFF sample scaling

Continuum background is evaluated using the OFF resonance data set. Yields derived from the OFF sample are scaled to match expectation in the ON sample. The scale factor, denoted α, is given by the ON to OFF ratio of integrated luminosity corrected for the cross section, σ, which is inversely proportional to the centre of mass energy squared, s, such that

$$\alpha = \frac{\mathcal{L}_{\rm on}}{\mathcal{L}_{\rm off}} \frac{s_{\rm off}}{s_{\rm on}} = \frac{\mathcal{L}_{\rm on}}{\mathcal{L}_{\rm off}} \left(\frac{10.52}{10.58}\right)^2 . \tag{4.2}$$

Since the number of detected fermion pairs from e^+e^- interactions is proportional to the integrated luminosity multiplied by the cross section, α can also be determined as

$$\alpha = \frac{N_{\rm ON}(f\bar{f})}{N_{\rm OFF}(f\bar{f})}. \tag{4.3}$$

The yield of Bhabha events detected in the barrel is used to calculate

$$\alpha = 3.005 \pm 0.002 \pm 0.015.$$

The efficiency for detecting fermion pairs is implicitly included in equation 4.3. The ON and OFF sample mismatch may affect the α measurement since experiment and run dependent factors in the efficiency will not precisely cancel in the ratio.

This problem cannot be altogether avoided even if the ON and OFF samples are matched, since at Belle only a small fraction of the time (one ninth of the runtime) is spent collecting OFF resonance data, and small changes in the running conditions do occur. A systematic uncertainty is assigned through a comparison of α calculated from Bhabha and di-muon detection events.

Since di-muon events are triggered by different criteria than Bhabha events, their respective detector responses, and therefore efficiencies, are independent. Consequently ON and OFF sample mismatch effects if evident are not expected to be the same in α measurements made separately with di-muons and Bhabha events. The difference of scale factors is found to be 0.2%, half of which is taken as the systematic uncertainty in α.

An additional 0.4% systematic uncertainty is assigned based on an offline luminosity measurement study performed by Belle collaborators[47]. The study considered effects on the Bhabha event selection deriving from: the ECL trigger; ECL and CDC selection criteria; and the inner material of the detector. Full numerical details of the α measurement are given in table 4.1.

Ratio ON/OFF measurement		
$\alpha = \frac{N(on)}{N(off)}(e^+e^-)$		
Statistical error		
$\mathrm{stat}(e^+e^-) = \mathrm{prescale} \times \sqrt{N/\mathrm{prescale}}$		
Systematic error		
$\delta(\alpha) = \frac{1}{2}\left(\frac{N(on)}{N(off)}(e^+e^-) - \frac{N(on)}{N(off)}(\mu^+\mu^-)\right)$		
$\oplus\, 0.4\%$ (see text[47])		
Data	Exp 13r1200+15+17 N_{on}	Exp 7-19 N_{off}
$e^+e^- \to e^+e^-$	184127950	61284110
$e^+e^- \to \mu^+\mu^-$	15548117	5183503
prescale = 50		

Table 4.1: Calculating α, the scaling factor for the ON to OFF data samples.

At momenta above $2.8\,\mathrm{GeV}/c$ there are no sources of electrons from $\Upsilon(4S)$ decay chains. Thus the ratio of yields above $2.8\,\mathrm{GeV}/c$ provides a cross check of the ON to OFF luminosity ratio measurement. The ON to OFF ratio of electron yields for $2.8 - 4.5\,\mathrm{GeV}/c$ gives $\alpha = 55622/18492 = 3.0079$, which is in agreement with the above measurement.

4.3 Hadronic event selection

The `HadronB`[48] skim has become the standard for B meson and hadronic continuum physics analyses at Belle. It has an efficiency of 99.1% for $\Upsilon(4S)$, 80% for hadronic continuum ($e^+e^- \to u\bar{u}, d\bar{d}, s\bar{s}, c\bar{c}$), and less than 5% for non-hadronic continuum events. The latter include $e^+e^- \to e^+e^-(\gamma), \mu^+\mu^-, \tau^+\tau^-$, 2γ and beam background interactions. The `HadronB` criteria are designed to remove non-hadronic events. These backgrounds have lower track multiplicity than $\Upsilon(4S)$ decays, and therefore each track possesses a large fraction of the available centre of mass energy and so collectively they tend to be collimated. Thus high-momentum back-to-back tracks are frequently encountered in these backgrounds. Particles from these backgrounds are also often out of the detector acceptance region, so there is little visible energy.

The hadronic event selection variables are calculated using reconstructed tracks and ECL clusters. The reconstructed tracks used have $p_T > 100\,\mathrm{MeV}/c$, and impact parameters from the nominal IP of $dr < 2.0$ cm and $|dz| < 4.0$ cm. ECL clusters with energy $E > 100\,\mathrm{MeV}$, and those not matched to CDC tracks define photon candidates within the CDC acceptance ($17° \leq \theta \leq 150°$). The tracks and photon candidates are boosted into the $\Upsilon(4S)$ rest frame with pion and zero mass assumptions respectively. In the following, the square of the total centre of mass energy is denoted by s.

The `HadronB` criteria are:

- The number of charged tracks,
$$N_{\mathrm{TRACK}} \geq 3; \tag{4.4}$$

- The total visible energy defined as the sum of track and photon energies
$$E_{\mathrm{VISIBLE}} \geq 0.20\sqrt{s}; \tag{4.5}$$

- The sum of track and photon momentum projected onto the z–axis
$$\left|\sum p_z c\right| \leq 0.5\sqrt{s}; \tag{4.6}$$

- The primary event vertex, determined from all tracks, must be positioned within a cylindrical surface defined by
$$r < 1.5 \text{ cm and } |z| < 3.5 \text{ cm} \tag{4.7}$$
and centred at the nominal IP;

- The sum of the cluster energies in the ECL within the CDC acceptance
$$0.1 \leq E_{\mathrm{SUM}}^{\mathrm{CDC}}/\sqrt{s} \leq 0.80; \tag{4.8}$$

- The number of ECL clusters in the barrel region of the detector ($-0.7 \leq \cos\theta \leq 0.9$)
$$N_{\mathrm{CLUSTER}} > 1; \tag{4.9}$$

- The energy sum of clusters within the ECL, and the Heavy Jet Mass, M_{jet}
$$E_{\mathrm{SUM}}^{\mathrm{ECL}}/\sqrt{s} > 0.18 \quad \text{or} \quad M_{\mathrm{JET}} > 1.8\ \mathrm{GeV}/c^2. \tag{4.10}$$

M_{JET} is the maximum of the invariant masses of summed track and photon four-momenta calculated separately in two hemispheres. The hemispheres are divided by the plane perpendicular to the thrust axis of the event. M_{JET} is essentially the τ invariant mass in τ-pair events. The M_{JET} requirement keeps a continuum event not consistent with a τ-pair event;

- If $M_{\mathrm{JET}} \leq 1.8\ \mathrm{GeV}/c^2$ then

$$M_{\mathrm{JET}} > 0.25 E_{\mathrm{VIS}}; \tag{4.11}$$

- The average cluster energy calculated from clusters within the ECL,

$$E_{\mathrm{SUM}}^{\mathrm{ECL}} / N_{\mathrm{CLUSTER}}^{\mathrm{ECL}} < 1\ \mathrm{GeV}. \tag{4.12}$$

The motivation for these cut choices is described in detail elsewhere [48]. The resultant cross sections and efficiencies for various processes after the application of `HadronB` criteria are shown in table 4.2.

Process $e^+e^- \rightarrow$	$B\overline{B}$	$q\bar{q}$	$\tau^+\tau^-$	$e^+e^-(\gamma)$	$\gamma\gamma$
$\epsilon(\%)$	99.1	79.5	4.9	0.002	0.4
$\sigma(\mathrm{nb})$	1.09	2.62	0.05	0.001	0.04

Table 4.2: Cross sections and efficiencies for various processes subject to the `HadronB` selection criteria.

4.4 The number of $B\overline{B}$ events

At Belle the number of $B\overline{B}$ events is calculated using

$$N_{B\bar{B}} = N_{\mathrm{ON}} - \frac{\epsilon_{\mathrm{ON}}}{\epsilon_{\mathrm{OFF}}} \alpha N_{\mathrm{OFF}}, \tag{4.13}$$

where α is the ON to OFF luminosity scaling variable, $\epsilon_{\mathrm{ON(OFF)}}$ is the `HadronB` skim efficiency for continuum events at ON(OFF) resonance energy [48]. The latter has been calculated using hadronic continuum samples generated at both ON and OFF resonance energies, and is given by

$$\frac{\epsilon_{\mathrm{ON}}}{\epsilon_{\mathrm{OFF}}} = 0.9958. \tag{4.14}$$

The ON resonance data sample analysed has

$$N_{B\overline{B}} = 29,388,453 \pm 381,999(1.3\%),$$

where the statistical and systematic errors have been added in quadrature. The statistical error amounts to 0.3%. The systematic error comprises of three components: scaling α $\pm 1.1\%$; beam gas background -0.1%; and $\epsilon_{\mathrm{ON(OFF)}}$ $\pm 0.5\%$; in all $\pm 1.2\%$.

4.5 Selection criteria

4.5.1 Pre–selection

Prior to the task of analysis it is necessary to reduce the data set to a manageable size. There are many events that pass `HadronB` cuts which are not of interest for the purposes of this analysis, namely those without electrons and events from continuum.

To reduce background from continuum events only events where the second normalised Fox-Wolfram moment meets the condition

$$R_2 < 0.5, \tag{4.15}$$

are selected. Here $R_2 \equiv H_2/H_0$, with

$$H_l = \sum_{i,j} |\vec{p_i}||\vec{p_j}| P_l(\cos\phi_{ij}), \tag{4.16}$$

where the indices i and j run over the tracks and neutral clusters (particles) produced in the event, ϕ_{ij} is the angle between particles i and j, and $P_l(x)$ is the Legendre polynomial of order l [49]. R_2 is a measure of event topology. Continuum events tend to be collimated along a signal axis, and on average have high R_2 values, whereas $B\overline{B}$ events tend to be more spherical and therefore have lower R_2 values.

Events are required to have at least one charged track consistent with an electron hypothesis ($\mathcal{L}_e > 0.8$, as described later in section 4.5.3), and the momentum of the track, must satisfy

$$p_{\mathrm{cm}} > 1.3\,\mathrm{GeV}/c. \tag{4.17}$$

This range includes lower and upper sideband momentum regions necessary for background studies.

After requiring events containing an electron candidate the non-hadronic continuum background was found to be reduced to roughly 36% of the continuum background. This was much larger than most other B-meson analyses. Therefore, the tighter hadronic skim criteria implemented for the `HadronC` sample were used. The more stringent cuts are:

$$E_{\mathrm{VISIBLE}} > 0.50\sqrt{s}; \tag{4.18}$$

$$\left|\sum p_z c\right| < 0.30\sqrt{s}; \tag{4.19}$$

$$N_{\mathrm{TRACK}} \geq 5. \tag{4.20}$$

The fraction of events remaining for MC and data after pre-selection are given in table 4.3.

Sample	Event fraction (%)
ON sample	1.99
MC $B\overline{B}$	3.86
MC charm	0.82
MC uds	0.18

Table 4.3: Remaining event fractions after applying pre–selection cuts in data and MC.

4.5.2 Track selection

Charged tracks are detected primarily by the CDC (as described in section 3.2.3). Axial wire hits provide $r - \phi$ coordinates while stereo wire hits measure the z coordinate. Hits in the CDC and SVD were fitted to particle tracks by assuming particles follow a helical trajectory. A helix is described by 5 parameters:

- the radius of curvature, which is proportional the transverse momentum;
- the pitch, which is proportional to the longitudinal momentum;
- and the pivot point coordinates, these define the point of closest approach to the detector origin.

The helix model neglects magnetic field non-uniformities, energy loss due to ionisation and multiple scattering. These effects along with SVD hit information are incorporated into a re-calculation of track parameters through the use of a Kalman filter algorithm. The addition of SVD hit information improves the pivot point measurement. Tracks are extrapolated all the way to the KLM using a Runge-Kutta method.

To further compensate for non-uniform magnetic field effects, which are most evident in the very forward and backward regions of the detector as demonstrated in figure 3.19, correction factors are applied to the measured momentum. These are calculated from comparisons of measured and true invariant mass peak positions of well known particles [50].

Poorly reconstructed tracks are rejected by imposing cuts on the track impact parameters denoted dr_{IP} and dz_{IP}. They are the r and z distance to the measured IP at the track's closest approach to the IP. Distributions of dr_{IP} and dz_{IP} in ON resonance data are shown in figures 4.4(a) and 4.4(b). The distributions reflect the width of the beam profile, B meson flight length and the resolution of the reconstructed track. All tracks to be considered as electron candidates must satisfy:

$$dr_{\mathrm{IP}} < 0.05 \text{ cm}; \tag{4.21}$$

and

$$|dz_{\mathrm{IP}}| < 2.0 \text{ cm}. \tag{4.22}$$

These cuts favour tracks originating from B-meson decays over those from secondary decays.

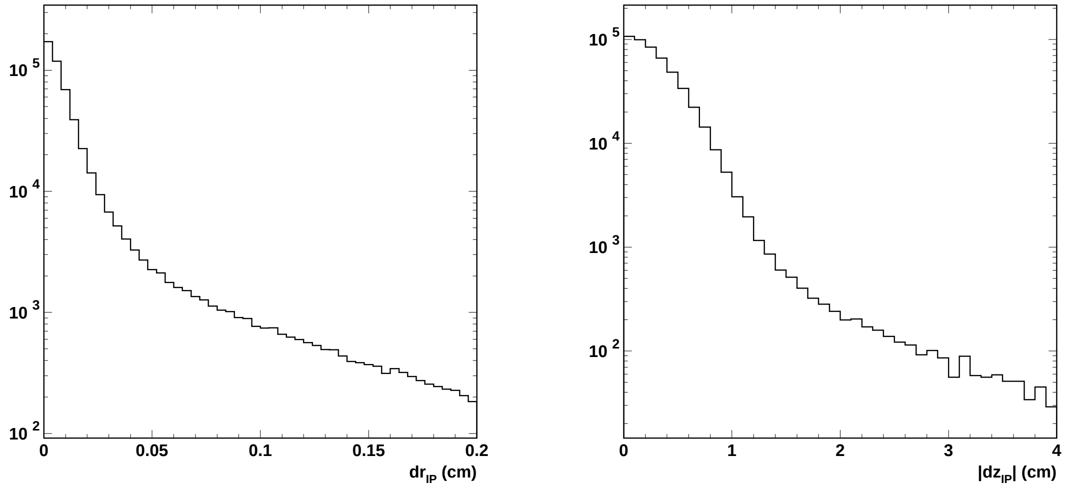

(a) dr_{IP} distribution for charged tracks.

(b) $|dz_{\mathrm{IP}}|$ distribution for charged tracks.

Figure 4.4: Charged track impact parameter distributions in experiment 15 ON resonance data for tracks that are consistent with an electron hypothesis and with $p_{\mathrm{cm}} > 1.5\,\mathrm{GeV}/c$.

4.5.3 Electron identification

Electrons in Belle are identified using five discriminating variables that utilise information from the CDC, ACC and ECL subdetector systems. The five variables are as follows:

Track to Cluster Matching χ^2 The projected electron track is required to match the position of a ECL cluster. The matching condition is decided by measuring a chi-square, defined as

$$\chi^2 = \frac{(\Delta\theta)^2}{\sigma^2_{\Delta\theta}} + \frac{(\Delta\phi)^2}{\sigma^2_{\Delta\phi}}, \tag{4.23}$$

where $\Delta\phi$ and $\Delta\theta$ are the angular separations between the centre of the cluster and projected track position. Both $\sigma_{\Delta\phi}$ and $\sigma_{\Delta\theta}$ are the resolutions determined from electron samples in data. A track-cluster match is found if $\chi^2 < 50$. If multiple tracks satisfy this requirement then the match with the lowest χ^2 is declared the matching track. The position resolution for electrons is better than that for hadrons, as demonstrated in figure 4.5(a).

E/p is the ratio of energy measured by the ECL and momentum measured by the CDC. Electrons, on average, deposit all of their energy in the calorimeter. In contrast, hadrons deposit only a small fraction of their energy, and this fraction fluctuates greatly. Consequently, E/p will tend towards one for electrons but will be less than one for hadrons, as demonstrated in figure 4.5(b).

E9/E25 is the ratio of energy deposited in a cluster in 3×3 crystals, E_9, and 5x5 crystals, E_{25}, about the centre of the shower. Electrons and hadrons shower differently in both longitudinal and transverse directions in the crystals since hadrons typically instigate more than one shower. The differences are demonstrated in figure 4.5(c), the peak of pions evident at 1 represents high momentum pions acting as minimum ionising particles.

dE/dx is the rate of energy loss due ionisation along a charged track's trajectory through the CDC. Described in section 3.2.3, for highly relativistic particles ($\beta \approx 1$), dE/dx depends logarithmically on the Lorentz factor, γ, of the particle, and therefore its mass. It provides excellent separation between electrons and pions for momenta greater than $0.5\,\mathrm{GeV}/c$, as shown in figure 4.5c.

ACC light yield $\langle N_{pe} \rangle$ is quantified by the yield of photoelectrons or lack thereof resulting from Čerenkov light. The threshold for electrons is a few MeV/c whilst that for pions is in the range $0.5\,\mathrm{GeV}/c$ – $1\,\mathrm{GeV}/c$. Thus discrimination between pions and electrons is only possible for particle momenta below $1\,\mathrm{GeV}/c$, and therefore is of no consequence to the track candidates considered for this analysis.

Probability density functions (PDF) characteristic of electrons and non-electrons (pions) are formed for each discriminating variable. These are constructed from data of electrons from Bhabha events and pions from K_s decays. A PDF is calculated for each of 10×6 bins in lab momentum and polar angle region respectively. An electron (pion) likelihood function is calculated as the product of the electron (pion) PDFs for each variable, $\mathcal{L}_i^{e(\pi)}$. The overall likelihood used for identification of an electron is then defined as

$$\mathcal{L}_e = \frac{\prod_{i=1}^{5} \mathcal{L}_i^e}{\prod_{i=1}^{5} \mathcal{L}_i^e + \prod_{i=1}^{5} \mathcal{L}_i^\pi}, \tag{4.24}$$

where the products are over the five discriminating variables. $\mathcal{L}_e$ is plotted in figure 4.6 for both electrons and pions. The likelihood is not a probability. Correlations between variables cause minor peaking of electron and non-electron hypothesis particles at 0 and 1 respectively.

Having passed the track quality and momentum cuts a charged track is classified as an electron candidate if

$$\mathcal{L}_e > 0.8. \tag{4.25}$$

In addition, since electron identification in the MC is found to agree best with data for electrons that shower in the barrel region of the ECL (discussed later in section 4.6.2), and due to heavy reliance on MC in the

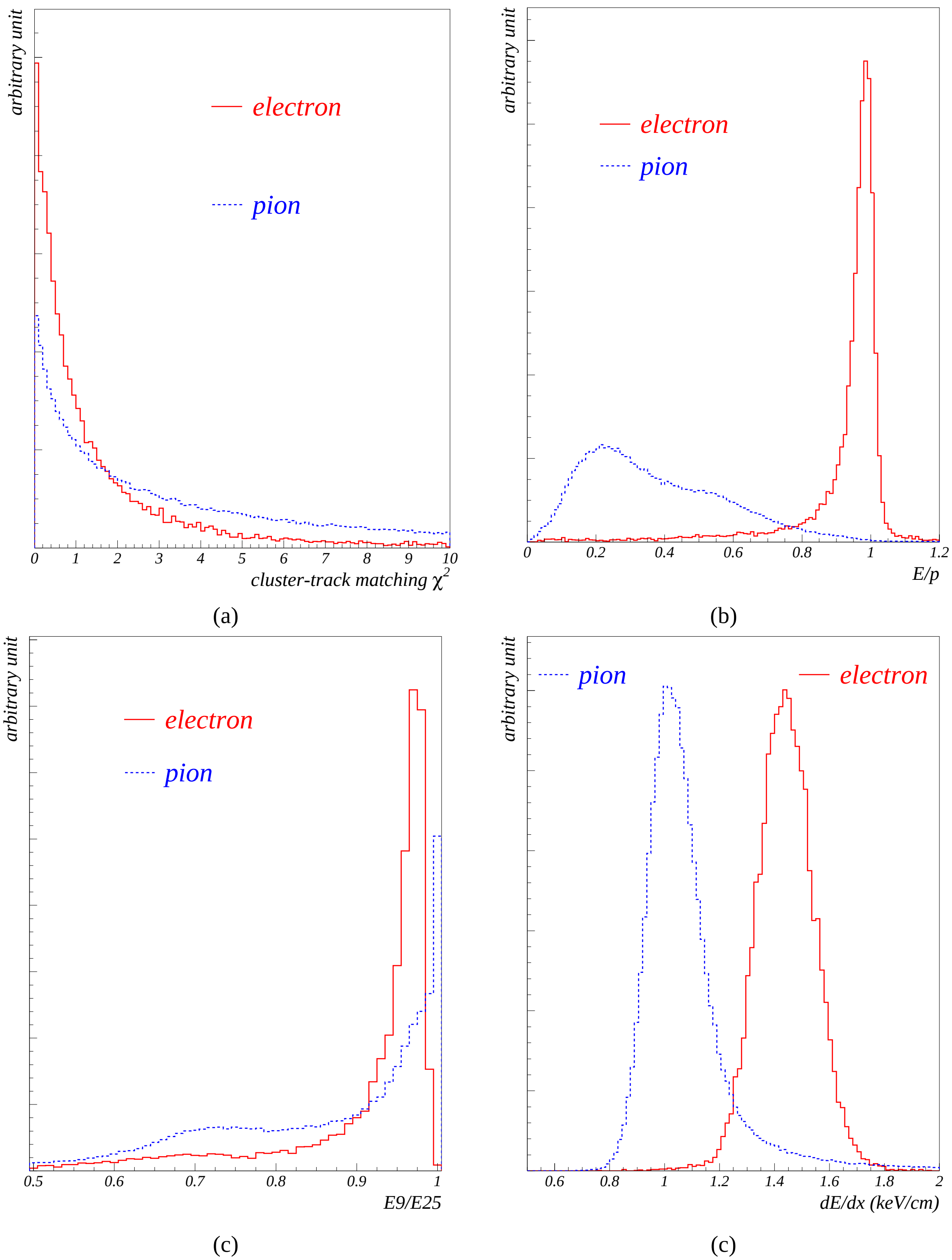

Figure 4.5: (a) The track to cluster matching, χ^2, (b) Ratio of energy deposition to track momentum, E/p, (c) Transverse energy shape, E_9/E_{25}, and (d) Rate of ionisation energy loss, $\frac{dE}{dx}$, for electrons (solid line) and pions (broken line).

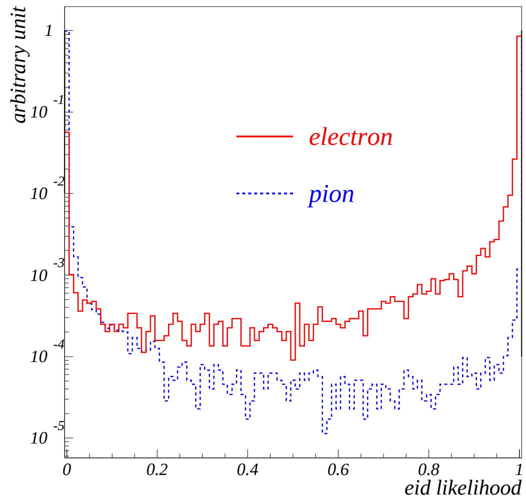

Figure 4.6: The electron likelihood, $\mathcal{L}_e$, for electrons (solid line) and pions (broken line).

analysis, candidates must also be within acceptance of the barrel,

$$-0.626 < \cos\theta < 0.846. \tag{4.26}$$

4.5.4 Continuum suppression

Continuum events are a significant background in this analysis. Unlike the background from $B \to X_c l \nu_l$ decays it cannot be avoided with a cut on the momentum. In the region $2.2 < p_{\rm cm}/{\rm GeV}/c < 2.6$ the signal to background is about 1 to 7 after pre-selection.

Eventually scaled OFF resonance data is subtracted from the ON resonance data to reveal distributions representative of data just from $B\overline{B}$ events. The statistical uncertainty will depend on the amount of OFF resonance data as well as on the level of the continuum background before subtraction. Therefore it is necessary to reduce the continuum background as much as possible.

Continuum backgrounds can be classified into two categories:

Hadronic continuum consisting $e^+e^- \to q\bar{q}$ where $q = (u, d, s, c)$;

QED related continuum mainly consisting of:

- two-photon events, $e^+e^- \to e^+e^-\gamma^*\gamma^* \to e^+e^-$ hadrons;
- radiative bhabha events, $e^+e^- \to e^+e^-\gamma$;
- τ-pair events, $e^+e^- \to \tau^+\tau^-$.

Photon conversion and π^0-Dalitz decay veto

The continuum produces many photons and neutral pions, whose subsequent decays respectively, through photon conversion, $\gamma \to e^+e^-$ and Dalitz decay, $\pi^0 \to e^+e^-\gamma$, provide background candidate electrons. To suppress this contribution, the invariant mass of the electron candidate paired with an oppositely charged track that is consistent with an electron hypothesis, $\mathcal{L}_e > 0.8$, and meets `HadronB` track requirements (if so found), must satisfy

$$|m_{e^+e^-}| > 0.1\,\mathrm{GeV}/c^2. \tag{4.27}$$

Figure 4.7 shows the $m_{e^+e^-}$ distributions in hadronic continuum MC for mass regions of interest, where the MC generator information has been used to identify the π^0 or photon mother of the candidate electron. The veto reduces hadronic and QED-related continuum by 5% and 30% respectively. The signal inefficiency is less than 0.1%. The leakage, defined as the fraction of electrons for which the veto is ineffective, is estimated to be 57% and 68% for γ and π^0 decays respectively.

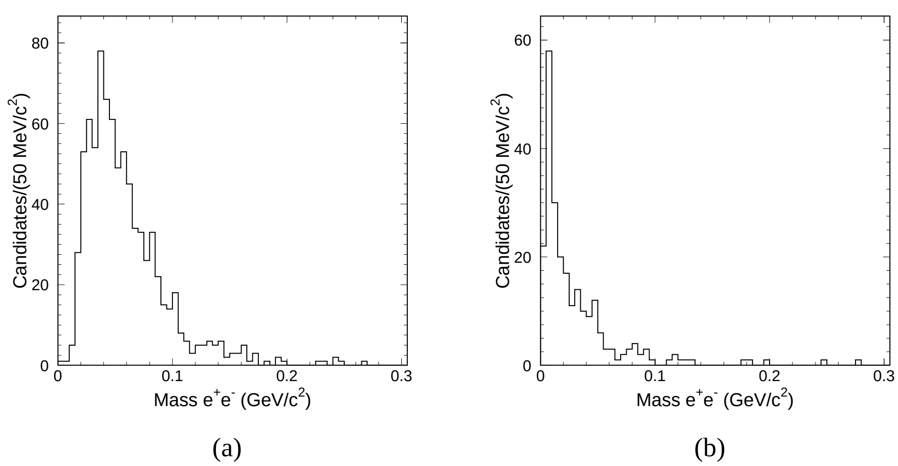

Figure 4.7: Hadronic continuum MC $m_{e^+e^-}$ distributions for generator identified (a) photon conversions and (b) π^0-Dalitz decays. The electron candidates satisfy $p_{\mathrm{cm}} > 1.5\,\mathrm{GeV}/c$ and the impact parameter cuts.

Virtual calorimeter

For signal events, the little energy available to B's in the collision rest frame ensures that their decay products have a higher probability of being evenly distributed throughout space. In contrast, continuum quark pairs hadronise and produce particles collimated into back-to-back jets, hence these events tend to be highly directional. The effect is more pronounced for the light quarks (u, d, s) than for the heavier charm quark (c).

Since the dynamics of the hadronic part of $B \to X_u e\nu$ are not well established it is important that selection requirements retain acceptance over a wide range of q^2 in order to minimise model dependence. The R_2 variable, a measure of event topology, which is well suited to discriminate background from signal, is not used because it has been found to disproportionately favour signal events with high q^2 (the squared mass of the virtual W boson) over those with low q^2. Low q^2 events mimic the continuum background topology since in these events the hadronic system, X_u, recoils hard against the lepton pair. For this reason, only a loose cut on R_2 was applied at the pre-selection level.

The effort to minimise the q^2 bias has also meant that cuts on the magnitude of missing momentum and its direction with respect to the candidate electron have not been used, even though they are amongst the best available suppressors of continuum background. These were used in an earlier CLEO endpoint analysis [51]. The recent CLEO analysis employed an adjusted virtual calorimeter type variable to recover acceptance at low q^2 while still providing overall good background suppression.

This analysis uses a similar virtual calorimeter type variable, denoted $\mathcal{F}_{\text{flow}}$. $\mathcal{F}_{\text{flow}}$ is a Fisher discriminant [52] of a set of "energy flow" variables formed by grouping detected particles in bins of 0.05 in $\cos\theta$ (cones), where θ is the particle angle with respect to the candidate electron in centre of mass frame, and taking the energy sum in each bin. The cones are depicted in figure 4.8. The detected particles are formed from tracks and clusters in much the same way the `HadronB` event selection variables were calculated. Though instead of assuming a pion mass for charged tracks, particle identification information is used to assign a mass hypothesis.

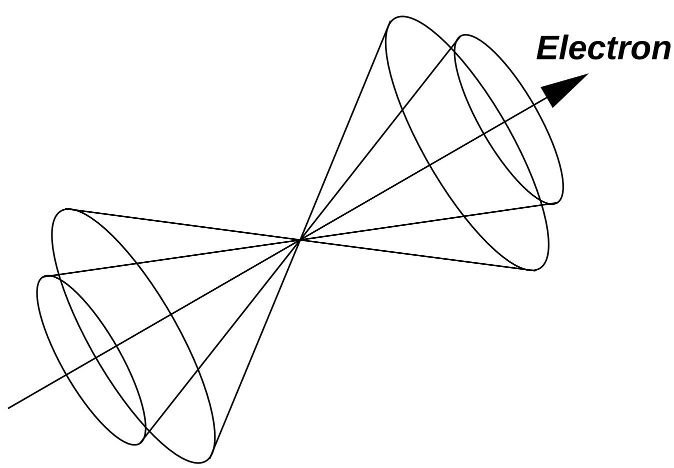

Figure 4.8: Energy flow into cones that are centred on the electron direction.

Energy flow into the i^{th} cone is defined as

$$E_{\text{FLOW}-i} = \sum_{j-tracks} E_j(\cos\theta_i < \cos\theta_j < \cos\theta_{i+1}) + \sum_{j-photons} E_j(\cos\theta_i < \cos\theta_j < \cos\theta_{i+1}), \tag{4.28}$$

where

$$\cos\theta_i = 1 - (i-1) \times 0.05, \qquad i = 1, 2, \ldots, 39.$$

Following the CLEO analysis, the energy flow in the backward direction $-1.00 < \cos\theta < -0.95$ was not used, as it was found to have a disproportionate effect in the low q^2 region [30]. The Fisher discriminant is defined as;

$$\mathcal{F}_{\text{flow}} = \sum_i \alpha_i E_{\text{FLOW}-i}, \tag{4.29}$$

where the coefficients are given by

$$\alpha_i = \sum_j (U^B_{ij} + U^S_{ij})^{-1}(\mu^B_j + \mu^S_j), \tag{4.30}$$

and $\mu^{S(B)}$ and $U^{S(B)}$ are the "energy flow" variable mean and covariance matrices for signal (continuum) events respectively. The coefficients define a hyper-plane in "energy flow" variable space and provide the best linear separation between continuum and signal events. They were calculated using signal and continuum Monte Carlo samples. Distributions of $\mathcal{F}_{\text{flow}}$ are shown in figure 4.9.

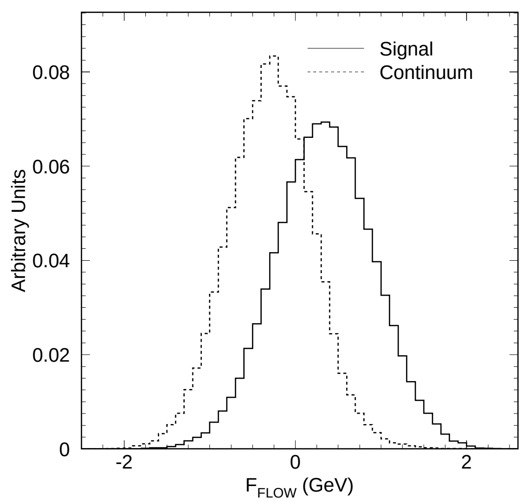

Figure 4.9: Signal and continuum $\mathcal{F}_{\text{flow}}$ distributions.

Tagging a rare B meson decay

In addition to suppression based on event topology, a b flavour tagging variable was implemented. The variable, $kl1$, is defined as

$$kl1 = Q(e)(N(K^+) - N(K^-)), \tag{4.31}$$

where $Q(e)$ is the charge of the electron candidate and $N(K^+)$ and $N(K^-)$ are the number of positively and negatively charged kaons identified in the event, respectively. A $B \to X_u l \nu_l$ decay will produce no net strangeness, however the decay of the associated B meson from the $\Upsilon(4S)$ resonance decay will on average produce a net strangeness through a $b \to c \to s$ quark transition since these are favoured processes. Moreover, the sign of the strangeness will be inversely correlated to the charge of the candidate electron. Continuum processes are strangeness symmetric and therefore no correlation exists. The signal $\Upsilon(4S)$ event properties are demonstrated in figure 4.10. Furthermore, no correlation is evident in non signal type B decays.

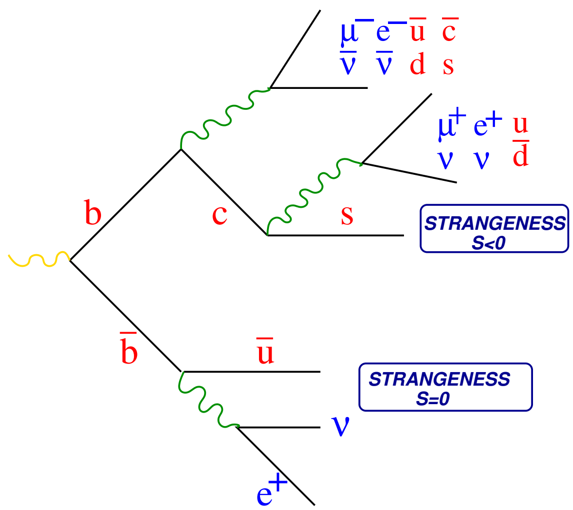

Figure 4.10: The rare b tag.

Calculating the difference in number of positively and negatively charged kaons is a way of calculating the strangeness. Information from neutral kaons cannot be used since these can only be evidenced through detection of K_L and K_S which give no strangeness information.

At Belle charged kaons and pions are identified by combining K/π probabilities of specific ionisation energy loss measurements made with the CDC, dE/dx, with light yield readings from the ACC and time of flight information from the TOF to form a $K(\pi)$ likelihood, $\mathcal{R}_{K(\pi)}$[53, 54]. Discrimination between kaons and pions is decided through the likelihood ratio

$$\mathcal{R}_{K\pi} = \frac{\mathcal{L}_K}{\mathcal{L}_K + \mathcal{L}_\pi}. \tag{4.32}$$

The average kaon identification efficiency and fake rate between $0.5 < p_{\text{lab}}/\text{GeV}/c < 4.0$ are $(88.0 \pm 0.1)\%$ and $(8.5 \pm 0.1)\%$ respectively. These are measured using fully reconstructed $D^{*\pm} \to D(\to K^\mp \pi^\pm)\pi^\pm_{\text{slow}}$ decays whereby kaons and pions are tagged by the charge of the slow pion, π_{slow}. Tracks with

$$\mathcal{R}_{K\pi} > 0.60 \tag{4.33}$$

are identified as kaon candidates.

MC signal and hadronic continuum $kl1$ distributions are plotted in figure 4.11. The asymmetry in signal events is apparent, while little or none is evident in continuum events.

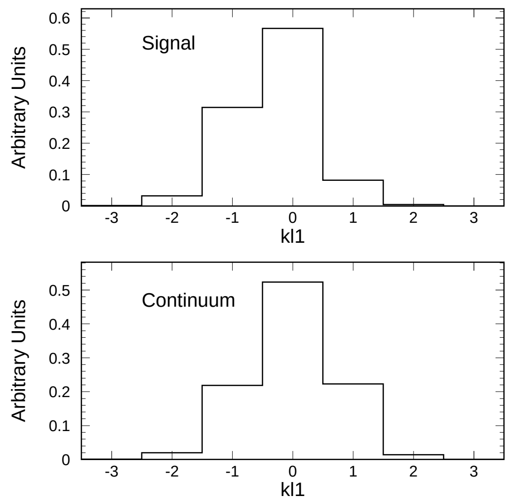

Figure 4.11: Distributions of $kl1$ for signal (above) and continuum (below) MC events.

The event thrust axis

Most QED related backgrounds derive from either a radiative Bhabha interaction ($e^+e^- \to e^+e^-\gamma$) coupled with beam backgrounds or a two photon event ($e^+e^- \to e^+e^-\gamma^*\gamma^* \to e^+e^-\text{hadrons}$). In these events a beam particle will scatter within the detector acceptance region while the other will escape down the beam pipe. Since the escaped particle will carry away some of the energy its existence can be inferred from missing momentum pointing in the beam direction. The missing momentum is calculated as the difference between the momentum of the beams and the sum of the observed track and cluster momenta as measured in the laboratory frame.

The detector acceptance for electrons was determined as a function of the cosine of the missing momentum polar angle (z-direction cosine), $\cos\theta_{\text{miss}}$, in both OFF data and hadronic continuum MC. Distributions representative of QED-related continuum events were constructed by subtracting hadronic continuum distributions from those in OFF data - hereafter referred to as the pseudo QED-related continuum sample. Furthermore a sideband region, defined by $1.7 < p_{\text{cm}}/\text{GeV}/c < 1.9$, was chosen to avoid using OFF data that is later subtracted from ON data to reveal the signal.

The $\cos\theta^{\rm cm}_{\rm miss}$ distribution for events with electron and positron candidates is shown in figure 4.12. The distributions peak at -1 and +1 for electron and positron candidates respectively, which is indicative of beam positrons and electrons escaping down the beam pipe. The evident asymmetry in the yields at the edges is due to the asymmetric nature of the detector.

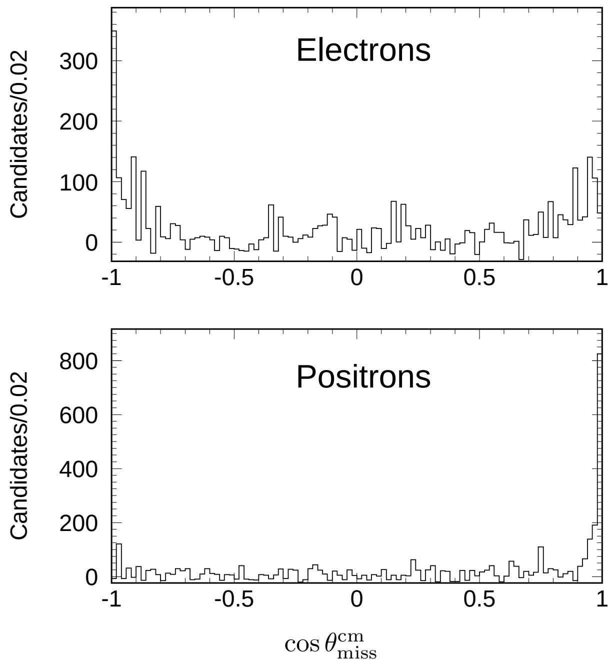

Figure 4.12: Distributions of $\cos\theta^{\rm cm}_{\rm miss}$ for electron (above) and positron (below) candidates.

Rather than imposing cuts on $\cos\theta^{\rm cm}_{\rm miss}$, as was done in previous analyses, the missing momentum was used in the calculation of the event thrust axis. The thrust axis of an event is the direction, $\vec{n}$, that maximises

$$\sum_i \frac{|\vec{n}\cdot\vec{p_i}|}{|\vec{p_i}|}, \tag{4.34}$$

where p_i is the momentum of the $i^{\rm th}$ track or cluster as measured in the centre of mass frame. The z-direction cosine of the thrust axis, $\cos\theta_{\rm Thrust-A}$, which has been calculated with the inclusion of the missing momentum, was found to suppress QED related continuum background just as effectively as a cut on $\cos\theta^{\rm cm}_{\rm miss}$ (since they are strongly correlated) but did a slightly better job of minimising the q^2 bias, as demonstrated in figure 4.13, even though the respective signal efficiencies were comparable.

The MC signal and QED related sample $\cos\theta_{\rm Thrust-A}$ sideband distributions are shown in figure 4.14 where clear discrimination is evident. It is not well understood why the signal distribution should be asymmetric although it may be due to the asymmetry of the detector.

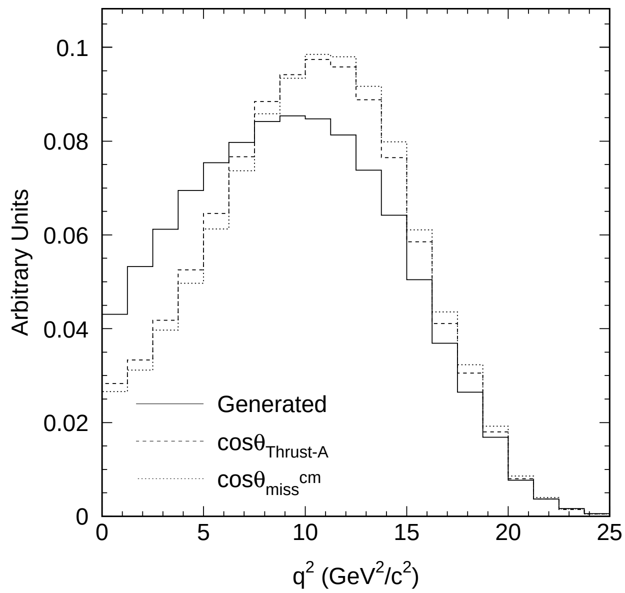

Figure 4.13: Normalised q^2 spectra; before detector acceptance (solid line), with a $\cos\theta_{\mathrm{Thrust-A}} < 0.75$ cut (dashed line) and with a $|\cos\theta^{\mathrm{cm}}_{\mathrm{miss}}| < 0.85$ cut (dotted line).

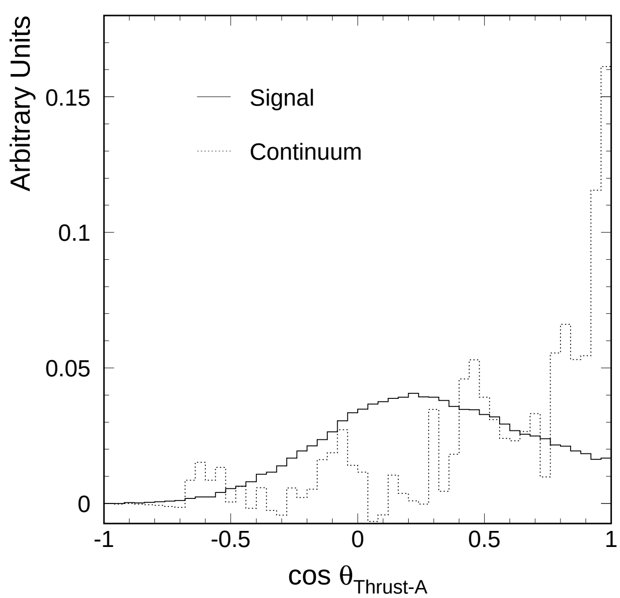

Figure 4.14: Distributions of $\cos\theta_{\mathrm{Thrust-A}}$ for signal MC events (solid line) and pseudo QED related continuum events (dotted line).

4.5.5 Optimising cuts on $\mathcal{F}_{\text{flow}}$, $kl1$ and $\cos\theta_{\text{Thrust-A}}$

To arrive at the eventual signal yield the continuum background will be subtracted using scaled OFF resonance data. Therefore, the cut positions should be chosen to minimise the statistical uncertainty in the eventual signal yield derived from this subtraction.

If T and B denote the total number of electrons in the ON and OFF data samples respectively, then the number of signal electrons in the ON sample, S, is given by

$$S = T - \alpha B, \tag{4.35}$$

where α is the OFF data scale factor(as described in section 4.2.3). The fractional error squared is then given by[2]

$$\left(\frac{\Delta S}{S}\right)^2 = \frac{(S + \alpha B) + \alpha^2 B}{S^2}. \tag{4.36}$$

Since the cut variable distributions for hadronic and QED related continuum events are different, the backgrounds are treated separately, such that

$$B = B_{q\bar{q}} + B_{\text{QED}}, \tag{4.37}$$

thereby giving

$$\frac{\Delta S^2}{S^2} = \frac{1}{S} + \frac{\alpha(1+\alpha)B_{q\bar{q}}}{S^2} + \frac{\alpha(1+\alpha)B_{QED}}{S^2}. \tag{4.38}$$

The fractional error is minimised by minimising each of its parts. Since the hadronic component is the greater of the two continuum contributions, the $\mathcal{F}_{\text{flow}}$ and $kl1$ cuts were chosen to minimise $\frac{\alpha(1+\alpha)B_{q\bar{q}}}{S^2}$, hereafter referred to as $F_{q\bar{q}}$. Accordingly the $\cos\theta_{\text{Thrust-A}}$ cut was chosen to minimise $\frac{1}{S} + \frac{\alpha(1+\alpha)B_{QED}}{S^2}$, hereafter referred to as F_{QED}. The $1/S$ term is part of F_{QED} instead of $F_{q\bar{q}}$ because $B_{q\bar{q}}$ is much larger than B_{QED}.

To determine $F_{q\bar{q}}$, S and $B_{q\bar{q}}$ were calculated using the ISWG2 signal and continuum MC samples that contained $100,000$ and $50,000$ events in the signal region respectively. The samples were simulated to match experiment 15 run-time conditions. S and $B_{q\bar{q}}$ were appropriately scaled to the expectation for $N_{B\bar{B}}$ equivalent to that of the ON resonance data sample. An inclusive branching fraction of $\mathcal{B}(B \to X_u e \nu_e) = 1.77 \times 10^{-3}$ was assumed based on the CLEO measurement in the same signal region[14]. In determining F_{QED}, S and B_{QED} were calculated in the sideband region from the signal MC and pseudo QED-related continuum background samples.

For improved signal efficiency the placing of a cut on the $kl1$ variable was avoided by instead making the cut on $\mathcal{F}_{\text{flow}}$ dependent on $kl1$ ($\mathcal{F}_{\text{flow}}(kl1)$). Specifically three cases of $kl1$ were examined: $kl1 < 0$;

[2] The term including the uncertainty in α is negligible.

$kl1 = 0$; and $kl1 > 0$. The optimal $\mathcal{F}_{\text{flow}}$ ($kl1$) cut was found to be:

$$kl1 < 0 \quad - \quad \mathcal{F}_{\text{Flow}} > 0.50; \tag{4.39}$$

$$kl1 = 0 \quad - \quad \mathcal{F}_{\text{Flow}} > 0.60; \tag{4.40}$$

$$kl1 > 0 \quad - \quad \mathcal{F}_{\text{Flow}} > 1.10. \tag{4.41}$$

This cut has a signal efficiency of 32%, with hadronic and QED related continuum background suppression factors of about 33 and 2, respectively. The difference in the suppression factors exemplify the differences between hadronic and QED related continuum backgrounds in the $\mathcal{F}_{\text{flow}}$ cut variable, and therefore validate the procedure for separating the backgrounds in the cut optimisation procedure.

The optimal $\cos\theta_{\text{Thrust}-\text{A}}$ cut was found to be:

$$\cos\theta_{\text{Thrust}-\text{A}} < 0.75. \tag{4.42}$$

This cut has a signal efficiency of 90%, with hadronic and QED related continuum background suppression factors of about 2 and 1.2, respectively. The continuum suppression variable distributions as well as the cut positions are shown in figure 4.15.

4.5.6 Physics vetoes for $B\overline{B}$ backgrounds

The same variable used to veto candidates from π^0-Dalitz decay and photon conversions, $m_{e^+e^-}$, was also used to reduce the background from $J/\psi \to e^+e^-$ and $\psi(2S) \to e^+e^-$ decays. Figure 4.16 shows the $B\overline{B}$ MC distributions for $m_{e^+e^-}$ in the J/ψ and $\psi(2S)$ mass region for events which have passed the analysis cuts, and where the generator information has been used to identify the mother particle of the candidate electron. The long tail to the left of the mass peak is a result of the electrons suffering bremsstrahlung energy loss. The mass peaks are well modelled by a `CRYSTAL BALL` line shape[3]. Vetoes are placed from -7σ and $+3\sigma$ around the peak, where $\sigma = 0.01\,\text{GeV}/c^2$, and are given by:

- $J/\psi \to e^+e^-$ veto

$$-0.07 < \frac{m_{e^+e^-} - m_{J/\psi}}{\text{GeV}/c^2} < 0.03; \tag{4.44}$$

- $\psi(2S) \to e^+e^-$ veto

$$-0.07 < \frac{m_{e^+e^-} - m_{\psi(2S)}}{\text{GeV}/c^2} < 0.03. \tag{4.45}$$

[3]The `CRYSTAL BALL` (CB) line shape is given by

$$f_{\text{CB}}(x) = \begin{cases} N\exp(-(x-\mu)^2/(2\sigma^2)) & , x \geq \mu - \alpha\sigma \\ N\exp(-\alpha^2/2)\left(\frac{n\sigma}{\alpha}\right)^n \left(\mu - x - \alpha\sigma + \frac{n}{\alpha}\sigma\right)^{-n} & , x < \mu - \alpha\sigma \end{cases} \tag{4.43}$$

where N is a normalisation constant, μ is the peak position, σ is the resolution, n and α are empirical parameters.

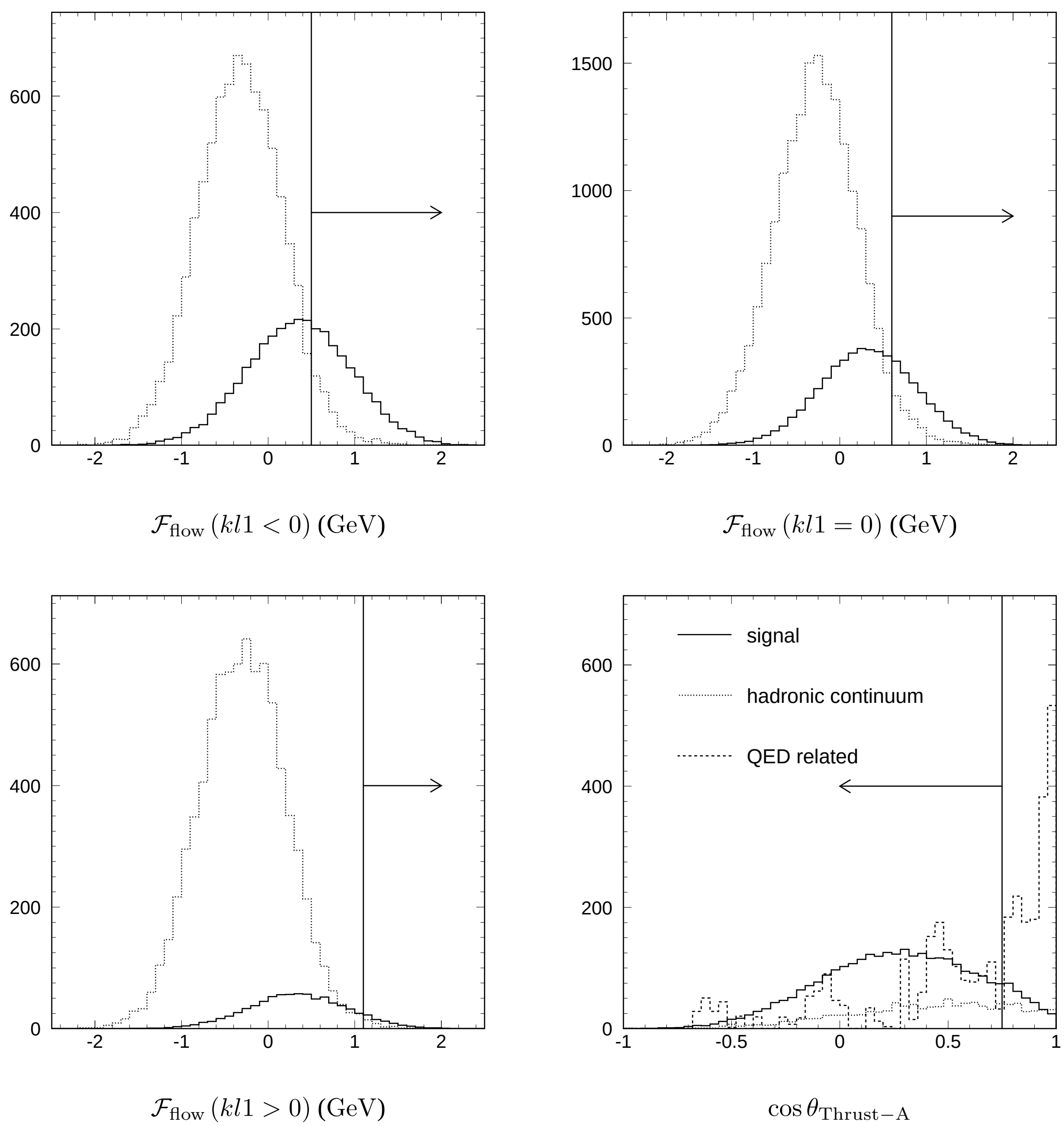

Figure 4.15: Distributions of the cut variables for signal (solid line), hadronic continuum (dashed line) and QED-related (dotted line) processes. The lines and arrows indicate the retained regions. The signal and background levels reflect expectations in the ON sample after all cuts so far discussed have been applied.

The leakage, either due to the measured $m_{e^+e^-}$ not surviving the cut or a failure to reconstruct the other electron, is estimated from the MC to be 41% and 38% for J/ψ and $\psi(2S)$ decay backgrounds, respectively. These vetoes result in a signal inefficiency of 0.4%.

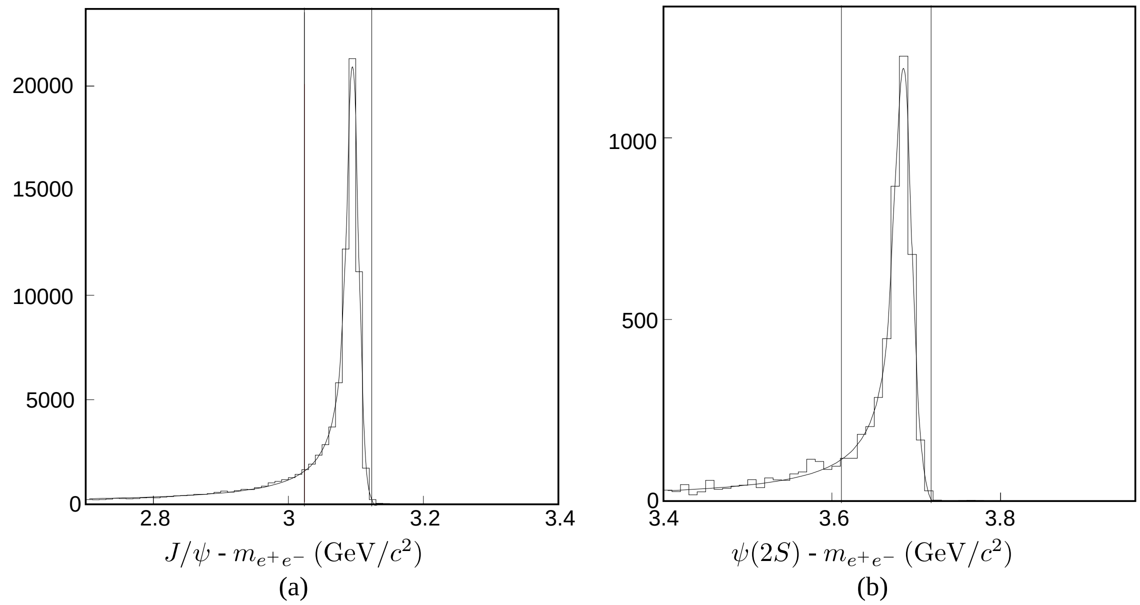

Figure 4.16: $B\overline{B}$ MC sample $m_{e^+e^-}$ distributions for generator identified (a) J/ψ and (b) $\psi(2S)$ decays. The candidates have all but continuum suppression criteria applied. The vertical lines bound the vetoed interval.

4.6 Reconstruction efficiency

In order to calculate a branching fraction the observed electron spectrum must be corrected for the signal reconstruction efficiency. The efficiency is measured as a function of the momentum in the centre of mass frame; for a given momentum region, Δp, there are N_g generated electrons and after cuts, N_r electrons are recovered, therefore the signal efficiency is calculated as

$$\epsilon_{\mathrm{MC}}(\Delta p) = \frac{N_r(\Delta p)}{N_g(\Delta p)}. \tag{4.46}$$

Table 4.4 shows a summary of the cuts applied to select $B \to X_u e \nu_e$ events and the cumulative efficiencies for each cut in the signal region, $2.2 < p_{\mathrm{cm}}/(\mathrm{GeV}/c) < 2.6$. The $\mathcal{F}_{\mathrm{flow}}$ cut is the most restrictive.

The efficiency as a function of generated momentum is plotted in figure 4.17. The reduction in efficiency seen for higher momenta is a consequence of the continuum cuts, since at these momenta the event topology of signal events comes to resemble that of continuum.

Cut	Candidates	Efficiency ϵ_{MC}
Generated	194606	-
Detector Acceptance		≈ 0.91
+ Track finding ($p_{\mathrm{lab}} > 1\,\mathrm{GeV}/c$)		≈ 0.93
+ Electron ID	148953	≈ 0.90
$R_2 < 0.50$	143470	0.963
`HadronC`	122568	0.860
IP + Barrel	106370	0.868
π^0/γ veto	106292	0.999
$\mathcal{F}_{\mathrm{flow}}(kl1)$	33929	0.319
$\cos\theta_{\mathrm{Thrust-A}} < 0.75$	30537	0.900
J/ψ veto	30451	0.997
$\psi(2S)$ veto	30420	1.000
Net	30420	0.156

Table 4.4: The selection criteria in order of application: resultant remaining candidates and efficiencies for the momentum interval, $2.2 < p_{\mathrm{cm}}/\mathrm{GeV}/c < 2.6$ in the ISGW2 signal MC sample.

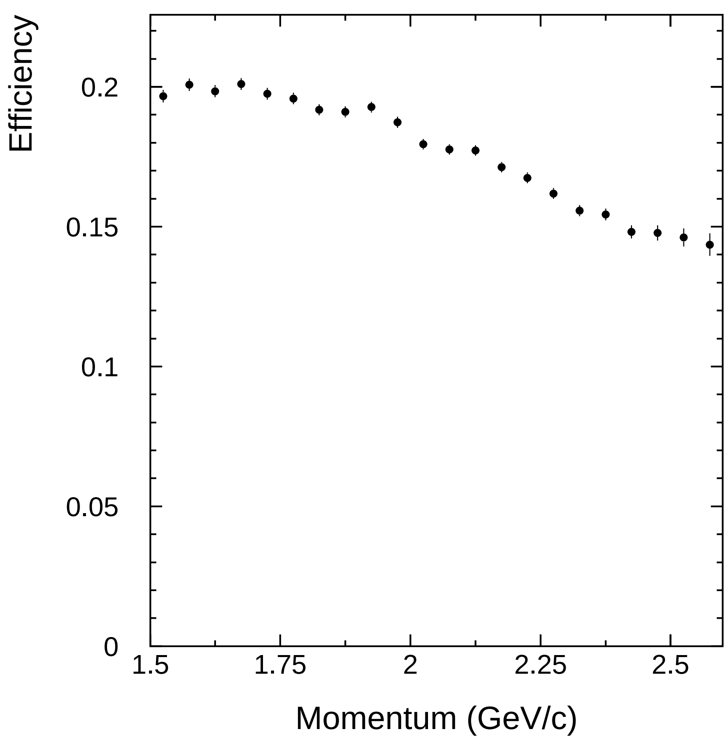

Figure 4.17: The efficiency as a function of momentum calculated using the ISGW2 signal MC sample

The following subsections describe sources of systematic uncertainty and model dependence in the efficiency measurement that derive from the use of MC.

4.6.1 Tracking efficiency in data and MC

The uncertainty on the track finding efficiency is a non-negligible source of systematic uncertainty. The tracks considered as electron candidates all have momenta in the lab frame greater than $1\ \mathrm{GeV}/c$. At Belle tracking performance for this kinematic region was studied using the embedding method [55]. The study is briefly described here.

The embedding method involves embedding the MC simulated detector response to a single track into MC and data $B\overline{B}$ events, and running the track finding and fitting software over the samples. The track finding efficiency is defined as the probability of reconstructing the embedded track.

In the embedding study performed, care was taken to consider all known sources of uncertainty in the MC simulation: magnetic field effects; CDC wire hit inefficiency; uncertainties in the material budget of the SVD and CDC; and drift time resolution effects in the CDC. No significant deviation between the data and MC single track reconstruction efficiency was found. The ratio of track finding efficiency in data to MC was found to be consistent with unity with an error of 1%. Accordingly, a 1% uncertainty was assigned as the systematic error in the efficiency due to tracking.

4.6.2 Electron identification efficiency in data and MC

At Belle a study of the electron identification (ID) efficiency has been performed with QED type two-photon events, $e^+e^- \to e^+e^-e^+e^-$, and a sample which contains single MC electron tracks embedded in hadronic data events[56]. The study measured the electron identification efficiency for the cut, $\mathcal{L}_e > 0.8$, the same as chosen for this analysis. The ratios of the measured efficiencies in two-photon to embedded MC electron track samples,

$$R = \frac{\epsilon_{e-\mathrm{ID}}(2\gamma)}{\epsilon_{e-\mathrm{ID}}(\mathrm{Embedded\,MC})}, \tag{4.47}$$

for various polar angle regions are given in Table 4.5. R is interpreted as the electron identification efficiency difference in data compared to MC. The measurements show very good agreement in the barrel regions of the ECL, less so for the endcaps. For this reason electron candidates were required to be within acceptance of the barrel ECL, $32.20° < \theta < 128.72°$.

For the benefit of this analysis a study of electron ID efficiency was undertaken in inclusive J/ψ events. A comparison of J/ψ yields between the cases where either one or both of the daughter tracks are subject to an electron ID requirements can yield an ID efficiency measurement (the method implemented is similar to that described in reference [57]). The study involved fully reconstructing $J/\psi \to e^+e^-$ decays with tracks satisfying the same track requirements as those met by electron candidates considered for this analysis, which are described in section 4.5.2. The study found, for $\mathcal{L}_e > 0.8$,

$$\frac{\epsilon_{e-\mathrm{ID:DATA}}}{\epsilon_{e-\mathrm{ID:MC}}} = 1.00 \pm 0.02. \tag{4.48}$$

Due to the measured consistency between MC and data in electron identification as demonstrated in the study, no corrections to the MC were applied. The error in the ratio, 2%, was assigned as the systematic uncertainty in the efficiency due to electron identification.

θ region (LAB)	$\mathcal{L}_e > 0.8$ R
$18 - 25$	1.045 ± 0.039
$25 - 35$	1.028 ± 0.037
$35 - 40$	1.000 ± 0.049
$40 - 60$	0.998 ± 0.016
$60 - 125$	1.011 ± 0.013
$125 - 132$	1.124 ± 0.170
$132 - 151$	1.096 ± 0.058

Table 4.5: Electron identification data to MC efficiency ratio (R) for $\mathcal{L}_e > 0.8$.

4.6.3 Event selection

A sample of fully reconstructed $B^+ \to D(\to K\pi)\rho^+$ decays was used to investigate possible differences between MC and data response to the event selection criteria; namely the $\mathcal{F}_{\mathrm{flow}}\,(kl1)$ and $\cos\theta_{\mathrm{Thrust-A}}$ cuts were investigated since these were the most restrictive.

The decay $B^+ \to D(\to K\pi)\rho^+$ was chosen for its ability to mimic the kinematics of $B^+ \to X_u l \nu_l$ decay. The $K\pi$ system is associated to the $e\nu_e$ system, such that the kaon, disregarding the particle identification is taken as the electron while the pion is assigned as the neutrino. The study is constrained to a limited kinematic region since $q^2 = m_D^2 = 3.5\,\mathrm{GeV}^2/c^4$.

Charged kaons and pions were selected from tracks satisfying $\mathcal{R}_{K\pi} > 0.6$ and $\mathcal{R}_{K\pi} < 0.6$ respectively. Neutral pion candidates were reconstructed from photon pairs with invariant masses in the range $0.115\,\mathrm{GeV}/c^2 < m_{\gamma\gamma} < 0.154\,\mathrm{GeV}/c^2$, corresponding to an interval of $\pm 3\sigma$ about the nominal π^0 mass, where σ is the experimental resolution. Photon candidates detected in the barrel and endcap ECL were required to have a minimum energy of $50\,\mathrm{MeV}$ and $100\,\mathrm{MeV}$, respectively. The π^0 reconstruction is the same as that implemented in the Belle $B \to \rho^0\pi^0$ analysis[58]. Neutral D meson candidates were reconstructed from the $K\pi$ decay mode with masses in the range $1.84\,\mathrm{GeV}/c^2 < m_{K^\pm\pi^\mp} < 1.89\,\mathrm{GeV}/c^2$[59]. Charged ρ meson candidates were reconstructed from the $\pi^\pm\pi^0$ decay mode with masses in the range $0.620\,\mathrm{GeV}/c^2 < m_{\pi^\pm\pi^0} < 0.920\,\mathrm{GeV}/c^2$, corresponding to $\pm\Gamma_\rho$, where Γ_ρ is the natural width of the ρ. B meson candidates were subsequently reconstructed from D and ρ meson pairs. B mesons originating from the $\Upsilon(4S)$ decay must each have half of the beam energy. This constraint provides two variables that are useful in selecting B meson candidates. These are the beam constrained mass,

$$M_{bc} = \sqrt{(E_{cm}/2)^2 - P_B^2}, \tag{4.49}$$

and the missing energy,

$$\Delta E = E_B - E_{cm}/2. \tag{4.50}$$

Here E_B is the reconstructed energy of the B meson candidate, E_{cm} is the beam energy, and P_B is the reconstructed momentum of the B meson candidate in the $\Upsilon(4S)$ rest frame. B meson candidates were required to have an $M_{bc} > 5.27\,\mathrm{GeV}/c^2$, in the circumstance of more than B meson candidate being found in the event, then that with smallest ΔE was kept. The combinatorial background in the MC was found to be negligible. The continuum background was modelled using OFF data, which was appropriately scaled and subtracted from yields found in the ON data to reveal signal B candidates.

Signal B meson yields were measured for $K^{\pm}$ candidates with momentum range $1.5 < p_{\mathrm{cm}}/(\mathrm{GeV}/c) < 2.6$ in $0.05\,\mathrm{GeV}/c$ bins. The kaon in the $B^+ \to D(\to K\pi)\rho^+$ decay was required to pass the same track and impact parameter cuts as the candidate electrons. The cut variables were calculated assuming missing momentum and energy from the pion, as is the case with a neutrino. The cut selection efficiency was measured as the ratio of yields after and before the $\mathcal{F}_{\mathrm{flow}}$ $(kl1)$ and $\cos\theta_{\mathrm{Thrust-A}}$ cuts were applied.

The cut efficiency is plotted for both data and MC in figure 4.18 along with the resultant data to MC efficiency ratio. The ratio was fit with a constant giving

$$\frac{\epsilon_{\mathrm{cut:DATA}}}{\epsilon_{\mathrm{cut:MC}}} = 0.997 \pm 0.022. \tag{4.51}$$

The result translates to an uncertainty of 2% in the continuum cut selection efficiency. The uncertainty doubled, 4%, was assigned as the systematic uncertainty due to event selection. The doubling was implemented to compensate for the assumption that the results from the study could be extrapolated to the other regions of q^2.

4.6.4 Model dependence

The main continuum suppression variable used in the signal event selection was chosen on its ability to minimise the bias in q^2. The q^2 efficiency, as taken from the generator information, is plotted in figure 4.19a. The use of the $\mathcal{F}_{\mathrm{flow}}$ variable as opposed to a conventional R_2 cut, causes the efficiency curve in the low q^2 region to plateau. The thrust axis polar angle cut is found to marginally reduce the efficiency at higher q^2. The efficiency as a function of the hadronic recoil mass, M_{X_u}, is plotted in figure 4.19b, which shows a slight degradation for higher M_{X_u}. Since different models predict different shapes in momentum, di-lepton mass, and hadronic recoil mass, the efficiency, dependent on these variables, measured in one sample will

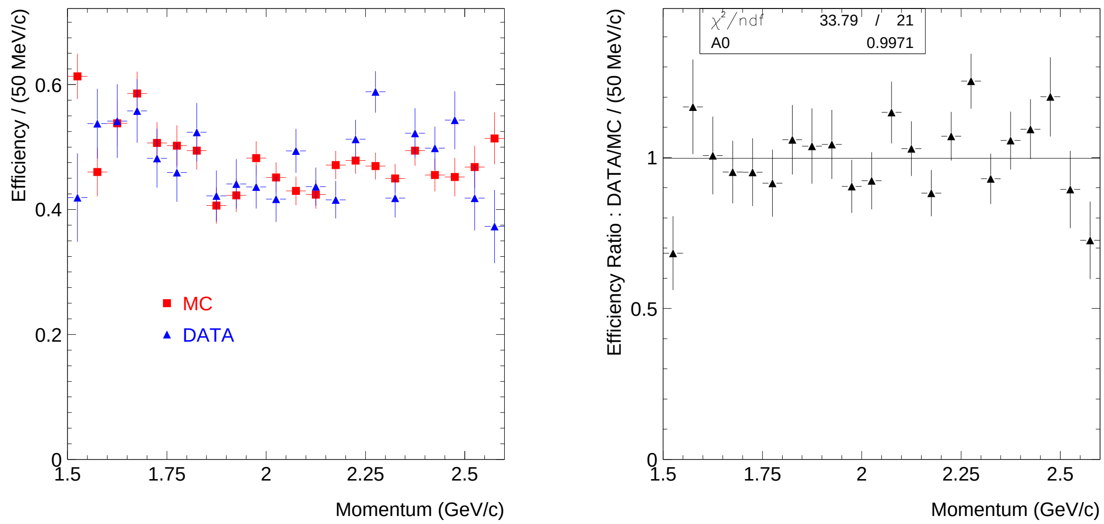

(a) (b)

Figure 4.18: $B \to D(\to K\pi)\rho$ control sample: (a) $\mathcal{F}_{\text{flow}}$ $(kl1)$ and $\cos\theta_{\text{Thrust-A}}$ cut efficiency in data (triangle) and MC (square) as a function of momentum and (b) the ratio of data to MC efficiencies as a function of the momentum.

differ to that as measured in a sample that has been constructed from different model assumptions. In other words, the efficiency is model dependent.

The model dependence was investigated by measuring the efficiency in all the signal MC sets described in section 4.2.2. The resultant measurements were used to calculate a mean, μ, and a root-mean-square deviation, σ_{RMS}. The uncertainty in modelling was calculated as

$$\Delta_{\text{model}} = (\mu - \epsilon_{\text{MC}}) \oplus \sigma_{\text{RMS}}, \tag{4.52}$$

where ϵ_{MC} is the efficiency as measured from the mainly exclusive ISGW2 modelled signal MC sample. The measured efficiencies in each of the signal MC sets along with the mean, root-mean-square and resultant model uncertainty are given in table 4.6. The model dependence ranges between $1.6\% - 2.6\%$ and increases as the lower momentum cutoff is decreased. This is not unexpected, since as shown in figure 4.3, the wide momentum intervals encompass the turning points in the spectrum, and this is where discrepancies in the spectral shapes are most noticeable.

4.6.5 Summary

The reconstruction efficiencies in the overlapping momentum intervals relevant to the extraction of $|V_{ub}|$ are shown in table 4.7. The error includes the uncertainties from MC statistics, tracking, electron identification, event selection and signal modelling. The consistency between the MC and data response was such that no

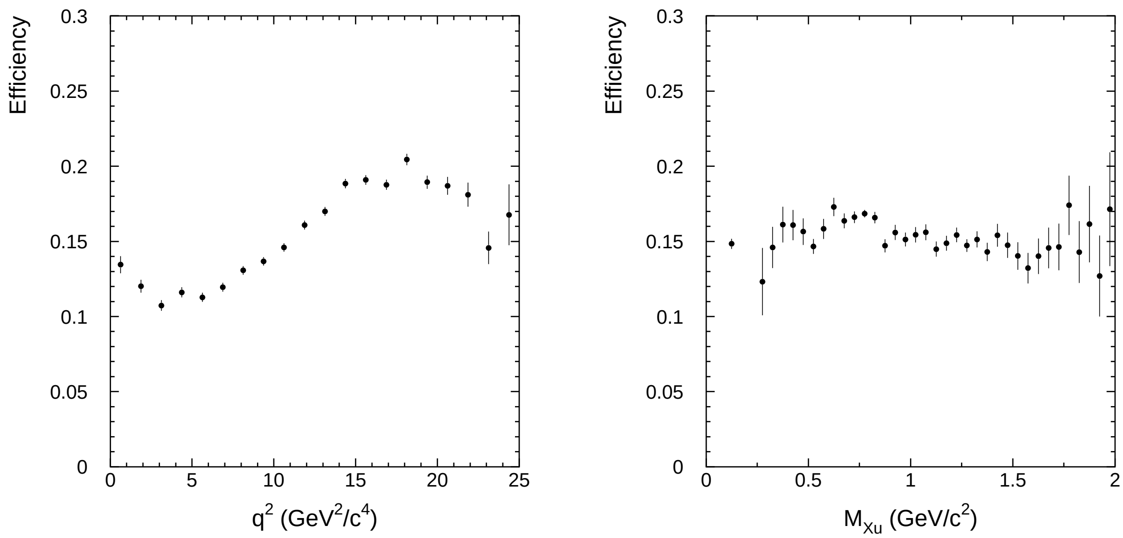

(a) (b)

Figure 4.19: The (a) q^2 and (b) M_{X_u} acceptance in the momentum region, $2.2 < \frac{p_{\rm cm}}{{\rm GeV}/c} < 2.6$, calculated using the ISGW2 signal MC sample.

Sample	Signal reconstruction efficiency ϵ(%) Region $x : x < p_{\rm cm}/({\rm GeV}/c) < 2.6$					
	$x = 1.9$	$x = 2.0$	$x = 2.1$	$x = 2.2$	$x = 2.3$	$x = 2.4$
ISGW2 ($\epsilon_{\rm MC}$)	17.03	16.62	16.17	15.70	15.22	14.79
Inclusive m_b μ_π^2						
4.80 0.30	17.08	16.45	15.97	15.58	14.97	15.22
4.68 0.30	17.75	17.20	16.59	16.18	15.42	14.75
4.92 0.30	16.55	16.17	15.65	15.26	14.95	14.63
4.80 0.19	17.34	16.95	16.38	15.83	15.72	15.25
4.80 0.41	16.66	16.21	15.84	15.32	15.03	14.94
μ	17.07	16.60	16.10	15.65	15.26	14.93
$\sigma_{\rm RMS}$	0.44	0.41	0.35	0.34	0.28	0.22
$\Delta_{\rm model}$	0.44	0.41	0.36	0.35	0.28	0.24

Table 4.6: Signal reconstruction efficiency for various signal MC samples(as described in Sec.4.2.2) and the resultant $B \to X_u l \nu_l$ model uncertainty.

corrections to the efficiency as measured by the MC were applied.

$p_{\rm cm}$ GeV/c	$\epsilon_{\rm MC}(\%)$
1.9-2.6	17.03 ± 0.90
2.0-2.6	16.62 ± 0.87
2.1-2.6	16.17 ± 0.82
2.2-2.6	15.70 ± 0.80
2.3-2.6	15.22 ± 0.76
2.4-2.6	14.79 ± 0.73

Table 4.7: Efficiency in overlapping momentum intervals.

Chapter 5

Analysis procedure

The analysis procedure in brief is as follows - once all the selection criteria are applied, the measurement of $B \to X_u e\nu_e$ is conducted for electron candidate momenta, $p_{\rm cm}$, above $1.9\,{\rm GeV}/c$ and below $2.6\,{\rm GeV}/c$, in six overlapping momentum regions defined by $\{1.9, 2.0, 2.1, 2.2, 2.3, 2.4\} < p_{\rm cm}/{\rm GeV}/c < 2.6$.

The continuum background is estimated from OFF resonance data. Minor $B\overline{B}$ backgrounds, namely fakes and secondary electrons, are modelled from the $B\overline{B}$ MC sample and normalised according to a fit of MC to data in the vetoed J/ψ mass region. The major $B\overline{B}$ background, $B \to X_c e\nu_e$, is modelled using a calibrated $B\overline{B}$ MC sample, and normalised according to the results of a fit conducted in the lower sideband region. This region is defined between $1.5\,{\rm GeV}/c$ and $2.2\,{\rm GeV}/c$ (the upper bound depends on the lower bound used for the signal extraction).

5.1 Raw electron yields in the ON sample

The electron candidate yields in the ON data sample after the application of selection criteria are given in table 5.1. The yields are made up of signal and background electron candidates. The following sections describe the estimation of each background.

$p_{\rm cm}$ (GeV/c)	$N_{\rm ON}$
$1.9 - 2.6$	104472 ± 323.2
$2.0 - 2.6$	54566 ± 233.6
$2.1 - 2.6$	23617 ± 153.7
$2.2 - 2.6$	8854 ± 94.1
$2.3 - 2.6$	3534 ± 59.2
$2.4 - 2.6$	1741 ± 41.7
$2.8 - 3.5$	2237 ± 47.3

Table 5.1: Raw electron candidate yields in the ON data sample, where the error is statistical.

5.2 Continuum Background

To account for the difference in beam energies between ON and OFF resonance running conditions, the momentum of candidates in the OFF sample are scaled by the ratio of ON to OFF centre of mass energy, such that

$$\frac{E_{\rm cm}^{\rm ON}}{E_{\rm cm}^{\rm OFF}} = \frac{10.58}{10.52} = 1.006, \tag{5.1}$$

and

$$p_{\rm cm} \rightarrow \frac{E_{\rm cm}^{\rm ON}}{E_{\rm cm}^{\rm OFF}}\, p_{\rm cm}. \tag{5.2}$$

The continuum background is calculated by multiplying the OFF yields by the scaling factor, α. The systematic uncertainty is derived from the error in α, which is 0.5%. The OFF data sample electron yields after the application of selection criteria are given in table 5.2. The ON and scaled OFF electron candidate momentum spectra are plotted in figure 5.1(a).

The beam energy difference may affect the continuum selection efficiency. All event shape distributions, such as $\mathcal{F}_{\rm flow}$ and $\cos\theta_{\rm Thrust-A}$ distributions are affected by the energy difference because the event topology is sensitive the available energy, that is events tend to become more jet-like at high energies and thus ON resonance continuum is more jet-like than OFF resonance continuum. The combined $\mathcal{F}_{\rm flow}\,(kl1)$ and $\cos\theta_{\rm Thrust-A}$ cut efficiencies were measured in hadronic continuum events MC generated at ON and OFF resonance energies. For electron candidates with momentum $p_{\rm cm} > 2.0\,{\rm GeV}/c$ the ON to OFF ratio of efficiencies was found to be

$$\frac{\epsilon_{q\bar{q}}^{\rm ON}}{\epsilon_{q\bar{q}}^{\rm OFF}} = 0.99 \pm 0.10. \tag{5.3}$$

The error in the study was limited by statistics.

The effect was also investigated by subtracting the scaled OFF yield from the ON yield in the momentum region $2.8 < p_{\rm cm}/{\rm GeV}/c < 3.5$, above the kinematic maximum for $B\overline{B}$ events. The resulting yield of 85 ± 93 electron candidates is consistent with zero. The resultant subtracted spectrum is plotted in figure 5.1(b).

$p_{\rm cm}$ (GeV/c)	$N_{\rm OFF}$	$\alpha N_{\rm OFF}$
$1.9-2.6$	2075 ± 45.6	$6234.3 \pm 136.9 \pm 25.3$
$2.0-2.6$	1631 ± 40.4	$4900.3 \pm 121.3 \pm 19.9$
$2.1-2.6$	1244 ± 35.2	$3737.6 \pm 106.0 \pm 15.2$
$2.2-2.6$	913 ± 30.2	$2743.1 \pm 90.8 \pm 11.1$
$2.3-2.6$	625 ± 25.0	$1877.8 \pm 75.1 \pm 7.6$
$2.4-2.6$	388 ± 19.7	$1165.8 \pm 59.2 \pm 4.7$
$2.8-3.5$	716 ± 26.8	$2151.2 \pm 80.4 \pm 10.7$

Table 5.2: Raw electron candidate yields in the OFF data sample.

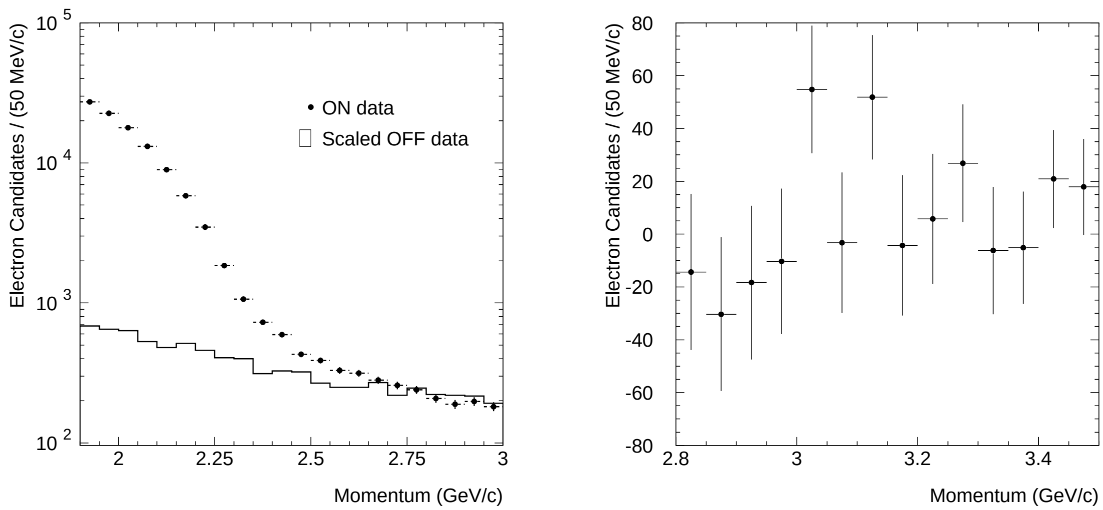

(a) (b)

Figure 5.1: Electron candidate momentum spectrum in (a) ON (data points) and scaled OFF (open histogram) data samples (b) continuum subtracted data ($N_{\mathrm{ON}} - \alpha N_{\mathrm{OFF}}$).

5.3 Minor $B\overline{B}$ backgrounds

The minor $B\overline{B}$ backgrounds consists of fakes and secondary electrons. Hadrons, such as pions and kaons, which are misidentified as electrons are referred to as 'fakes'. Secondary electrons are electrons that originate from non primary B meson decays.

5.3.1 Monte Carlo to Data Normalisation

The $B\overline{B}$ MC sample is used to estimate the background contribution from fakes and secondary electrons. The sample contains roughly three and half times as much $N_{B\overline{B}}$ events as the ON data sample. The exact scaling, referred to as the MC normalisation factor, denoted $R_{\mathrm{data/mc}}$, is required to properly scale these background contributions.

The ratio of the number of vetoed electron candidates for data to MC in the J/ψ mass region is used to calculate $R_{\mathrm{data/mc}}$. The benefit of this approach is that normalisation can occur after the full selection criteria have been applied. It therefore takes into account manifest MC and data efficiency differences. Furthermore, inclusive J/ψ decays are reasonably well modelled in the MC, with the inclusive branching fraction $\mathcal{B}(B \to J/\psi X)$, as implemented in the `QQ98` event generator being consistent with the world average measurement[17].

The yields of electrons from J/ψ, in $0.05\,\mathrm{GeV}/c$ bins, were extracted from fits to the $m_{e^+e^-}$ distributions in the mass range, $2.7\,\mathrm{GeV}/c^2 - 3.4\,\mathrm{GeV}/c^2$. In the fits, `CRYSTAL BALL` line shape and exponential functions were used to model the signal and background, respectively. The yield was calculated as the integration of the `CRYSTAL BALL` line shape function in the vetoed J/ψ mass region.

$R_{\mathrm{data/mc}}$ is calculated by performing a χ^2 fit of the MC momentum spectrum of vetoed electron candidates from J/ψ to the equivalent spectrum in data. $R_{\mathrm{data/mc}}$ is the free parameter in the fit. The fit result is displayed in figure 5.2. It finds

$$R_{\mathrm{data/mc}} = 0.263 \pm 0.004. \tag{5.4}$$

The ratio of $N_{B\overline{B}}$ events in data to MC is 0.278, which is slighter larger than that given by the fit. The difference between the two measures, 5.4%, is taken as a systematic uncertainty in the evaluation of the fake and secondary backgrounds.

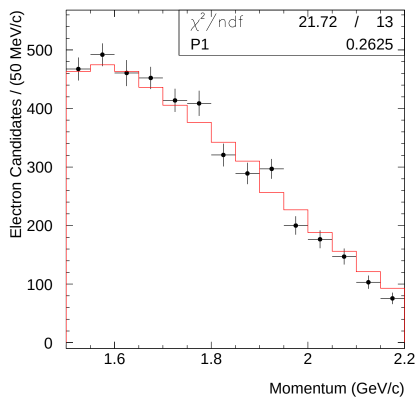

Figure 5.2: Fit of MC (histogram) to data (data points) in the momentum spectrum of vetoed electrons from J/ψ.

5.3.2 Fakes

In the MC all but a very small fraction of electron fakes are caused by pions ($\approx 2\%$ kaon, $\approx 1\%$ proton). The inclusive pion rate from B decays in the generator is consistent with the world average. Measurements of the pion to electron fake rate f_π, in MC and data were carried out in the momentum interval, $1.5 < p_{\mathrm{cm}}/(\mathrm{GeV}/c) < 2.7$, using a sample of $K_s \to \pi^+\pi^-$ decays. The pions were required to meet the same track requirements as those applied to the electron candidates in this analysis with the exception of the impact parameter cuts.

A correction factor, calculated as the ratio of fake rate in data to MC, is applied to the MC electron fake yield. These are given in table 5.3. Figure 5.3 displays the momentum spectra of fakes in the $B\overline{B}$ MC sample as well as that of the pions used in the K_s sample fake rate study. It demonstrates that the corrections as calculated using the latter sample are suitable for application to the fakes spectrum, in that, the corrections are not marred by spectral differences. The corrected fakes yield from MC are scaled by $R_{\mathrm{data/mc}}$.

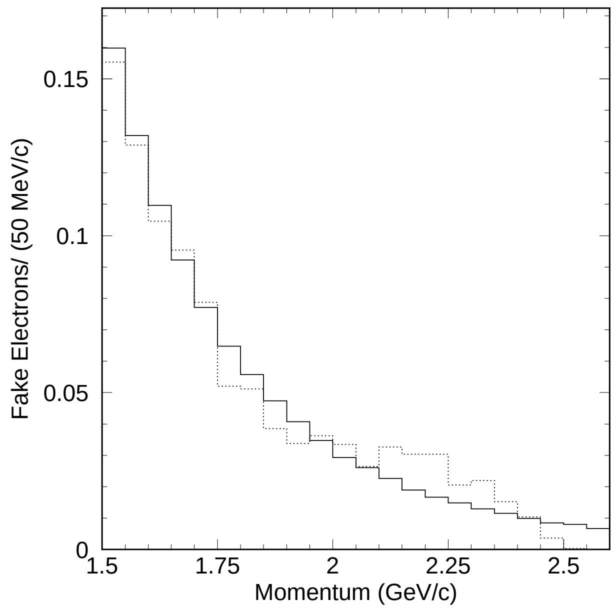

Figure 5.3: The normalised momentum spectrum of electron fakes after applying selection criteria (dotted line) and of pions from $K_s \to \pi^+\pi^-$ decays in data (solid line).

Barrel : Pion to Electron Fake Rate $f_\pi(\%)$		
Sample	Momentum (GeV/c)	
	1.5-2.2	2.2-2.7
DATA	0.060 ± 0.004	0.114 ± 0.017
MC	0.123 ± 0.010	0.137 ± 0.031
RATIO	0.49 ± 0.05	0.83 ± 0.23

Table 5.3: Pion to electron fake rate measurements.

The yields of fake electrons are given in table 5.4. The statistical error derives from MC statistics. In the signal region the relative uncertainty in the correction factor is 0.3[1], and is assigned as the systematic uncertainty in the fakes yield. This more than dominates the 5% uncertainty associated with $R_{\mathrm{data/mc}}$.

[1]Rounded up.

$p_{\rm cm}$ (GeV/c)	$N_{\rm fake}$
$1.9 - 2.6$	$231.4 \pm 7.1 \pm 69.4$
$2.0 - 2.6$	$176.8 \pm 6.2 \pm 53.0$
$2.1 - 2.6$	$129.1 \pm 5.3 \pm 38.7$
$2.2 - 2.6$	$79.3 \pm 4.2 \pm 23.8$
$2.3 - 2.6$	$39.9 \pm 2.9 \pm 12.0$
$2.4 - 2.6$	$11.1 \pm 1.6 \pm 3.3$

Table 5.4: Fake electron candidate yields derived from corrected MC. The first error is statistical and the second is systematic.

5.3.3 Secondary electrons $B \to X \to e$

The non primary B-meson decays contributing secondary electrons include $J/\psi \to e^+e^-$, $D \to Xe\nu_e$, $\psi(2S) \to e^+e^-$ and to a lesser extent $\tau \to e\nu\nu$, $D_s \to Xe\nu_e$, photon conversions and π^0 Dalitz decays. The branching fractions were measured in the generator in a study of one million generic B decays. Where they differ from world average values, corrections are applied, as listed in Table 5.5.

Secondary Electrons $B \to X \to e$	
X	correction
D^0	0.91
$D^\pm$	0.83
$\psi(2S)$	0.89
τ	0.94

Table 5.5: Inclusive branching fraction correction factors.

Figure 5.4 shows the background from secondary electrons in the endpoint region. The "other" category includes background from D_s, π^0 and γ. Even though an explicit veto is applied, the $J/\psi \to e^+e^-$ is found to be the dominant background. The yields from J/ψ are given in table 5.6. The first error is the uncertainty from MC statistics and the second error is the systematic uncertainty. The latter is obtained from the uncertainty in the $B \to J/\psi \to e$ inclusive rate, 5.2%, combined the uncertainty from $R_{\rm data/mc}$, which in total is 7.5%.

The remaining secondary background yields, dominated by electrons from semileptonic D-meson decays, are given in table 5.7. The first error is from MC statistics. The second error, the systematic uncertainty, derives from the MC normalisation, 5%, which is combined with each individual inclusive decay branching fraction uncertainty. Since backgrounds from γ and π^0 have little effect on the endpoint region, a conservative 100% systematic uncertainty was assigned. The systematic uncertainties for the remaining backgrounds were assigned according to the cumulative errors in world average inclusive measurements; 80% for D_s, 12% for τ, 16% for $\psi(2s)$, 14% for D^+, and 6% for D^0.

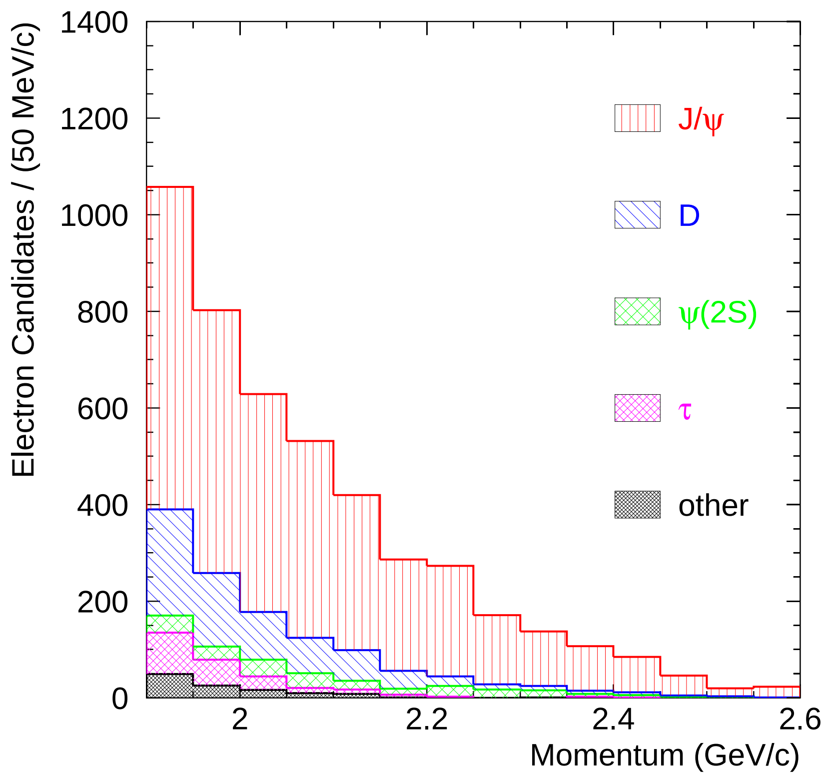

Figure 5.4: Secondary electron backgrounds in the endpoint region.

$p_{\rm cm}$ (GeV/c)	$N_{J/\psi}$
$1.9 - 2.6$	$889.6 \pm 15.4 \pm 66.7$
$2.0 - 2.6$	$569.0 \pm 12.3 \pm 42.7$
$2.1 - 2.6$	$339.0 \pm 9.5 \pm 25.4$
$2.2 - 2.6$	$191.4 \pm 7.1 \pm 14.3$
$2.3 - 2.6$	$93.7 \pm 5.0 \pm 7.0$
$2.4 - 2.6$	$39.9 \pm 3.2 \pm 3.0$

Table 5.6: Secondary electrons from J/ψ, where the first error is statistical and the second is systematic.

p_{cm} (GeV/c)	$N_{B\to X\to e}$
$1.9-2.6$	$576.6\pm17.6\pm75.0$
$2.0-2.6$	$269.8\pm9.5\pm34.4$
$2.1-2.6$	$129.8\pm5.9\pm15.0$
$2.2-2.6$	$53.5\pm3.6\pm6.1$
$2.3-2.6$	$23.1\pm2.4\pm2,7$
$2.4-2.6$	$7.8\pm1.4\pm0.8$

Table 5.7: Secondary electrons from all other decays, where the first error is statistical and the second is systematic.

5.4 Major $B\overline{B}$ backgrounds : Charmed Semileptonic B decay

Candidate electrons from charmed semileptonic B meson decay are the dominant background for regions including momentum $p_{\mathrm{cm}} < 2.3\,\mathrm{GeV}/c$. This background was evaluated from fits of MC simulated spectra to the ON data electron spectrum in the lower sideband region. This is the same approach undertaken in the CLEO analysis [30].[2]

The fits performed in the lower sideband regions, which are defined by $1.5 < p_{\mathrm{cm}}/\mathrm{GeV}/c < \{1.9, 2.0, 2.1, 2.2\}$, determine the charmed semileptonic B-meson decay background in the regions, $\{1.9, 2.0, 2.1, \{2.2, 2.3, 2.4\}\} < p_{\mathrm{cm}}/\mathrm{GeV}/c < 2.6$ respectively.

The spectrum from $B\to X_c e\nu_e$ in the `QQ98` generator is modelled using four components[3]: $X_c = D$(ISGW2), D^*(HQET), higher resonance charm meson states D^{**}(ISGW2) and non-resonant $D^{(*)}\pi$ (Goity and Roberts [60]). The spectrum from $B\to X_u e\nu_e$ is derived from the (mainly) inclusive signal MC sample (described in section 4.2.2, with $m_b = 4.80\,\mathrm{GeV}/c^2$ and $\mu_\pi^2 = 0.30\,\mathrm{GeV}^2/c^2$).

The background estimate is sensitive to the makeup of $B\to X_c e\nu_e$ processes, so therefore as much information as possible was sourced from available data to better model the background. This translated into an exhaustive MC calibration effort. The calibration involved:

Beam energy correction In the centre of mass frame, the endpoint of the electron spectrum from $B\to X_c e\nu_e$ decays, $E^{\mathrm{max}}_{\mathrm{cm}}$, is determined by the B-meson boost, β, and endpoint energy in the B-meson rest frame, $E^{\mathrm{max}}_{\mathrm{B-rest}}$,. such that for a small boost

$$E^{\mathrm{max}}_{\mathrm{cm}} \simeq (1+\beta)E^{\mathrm{max}}_{\mathrm{B-rest}}. \tag{5.5}$$

[2]The procedure however deviates slightly from that of CLEO, since only spectra derived from the data and MC samples where all selection criteria have been applied are used. CLEO determined the relative weights of the sub-component backgrounds from fits to spectra where the main continuum suppression cuts had not been applied. The relative weightings were then preserved in the fits of simulated MC to data spectra where the continuum suppression cut had been applied.

The approach used here is different, since the assumption that continuum cuts don't affect the relative weighting is not made. The selection criteria bias the q^2 and momentum spectra and may therefore act differently on each sub-component of the background. This may cause the relative sub-component proportions to vary before and after cuts. Though the extent to which this may occur is not examined.

[3]More information is given in Appendix A

A beam energy difference between data and MC will cause a difference in the respective B boosts and therefore a likewise change in the kinematic endpoint. Since the $\Upsilon(4S)$ mass is so close to the $B\overline{B}$ production threshold the endpoint is highly dependent on the total energy of the colliding beams. The nominal centre of mass collision energy during ON resonance running is given by

$$\sqrt{s} = \sqrt{2E_{e^+}E_{e^-}(1+\cos\theta_{\rm crossing})} = \sqrt{2\times 3.5\times 8.0\times(1+\cos(0.022))} = 10.58\,\mathrm{GeV}, \quad (5.6)$$

and it is these beam conditions that are implemented in the `QQ98` generator. The KEKB accelerator team do their best to implement these parameter values but inevitably there is a tolerance.

Belle has measured the beam energy in data from a sample of fully reconstructed B meson decays[61]. The study measured the beam energy in run intervals chosen according to the consistency of hadronic to Bhabha event ratios. The measured beam energy in the ON data sample used for this analysis was calculated as an average of their measurements weighted by the number of Bhabha events. The beam energy in data was calculated to be

$$E^{\rm beam}_{\rm cm:DATA} = (5.28863 \pm 0.00014)\,\mathrm{GeV}. \quad (5.7)$$

This value is lower than that simulated in the MC

$$E^{\rm beam}_{\rm cm:MC} = 5.29003\,\mathrm{GeV}. \quad (5.8)$$

Furthermore, the resolution, though slightly finer in data, was found to agree with the MC prediction within uncertainty. The beam energy difference is significant. For example, it translates into a 13% over-estimate of the background from $B \to De\nu_e$ in the momentum interval $2.3\,\mathrm{GeV}/c - 2.6\,\mathrm{GeV}/c$. The large discrepancy meant that the typical procedure of re-weighting the MC in B-meson momentum was not applied. Rather an event by event correction, based on the measured difference in beam energy in data and MC, was applied to the reconstructed candidate electron momentum in MC. It was implemented as follows:

1. For a semileptonic B-meson decay, $B \to Xe\nu$, retrieve the generator information of the B-meson and electron 4-momenta in the $\Upsilon(4S)$ rest frame, P_B and P_e respectively. In this frame denote p_e^{gen} as the magnitude of the electron momentum, which is the generated momentum of the reconstructed electron;
2. Boost P_e into the rest frame of the B-meson;
3. Boost P_e back into $\Upsilon(4S)$ frame; using a corrected B boost vector calculated such that

$$E^{\rm B}_{\rm cm:MC} \to (E^{\rm B}_{\rm cm:MC} - E^{\rm B}_{\rm cm:MC:\mu}) + E^{\rm B}_{\rm cm:DATA:\mu}, \quad (5.9)$$

where $E^{\mathrm{B}}_{\mathrm{cm:MC:}\mu}$ and $E^{\mathrm{B}}_{\mathrm{cm:DATA:}\mu}$ refer to the mean beam energies. Denote $p_e^{gen\prime}$ as the new magnitude of the generated electron momentum;

4. Shift the reconstructed electron momentum in MC, p_e^{rec}, by the difference in generated momentum,

$$p_e^{rec} \rightarrow p_e^{rec} + (p_e^{gen\prime} - p_e^{gen}). \tag{5.10}$$

The correction was tested by observing the B momentum distribution in MC before and after the correction, and comparing the latter to that of a small MC sample generated with measured beam energy in data. Figure 5.5 displays the results of the comparison, which shows the correction to be adequate.

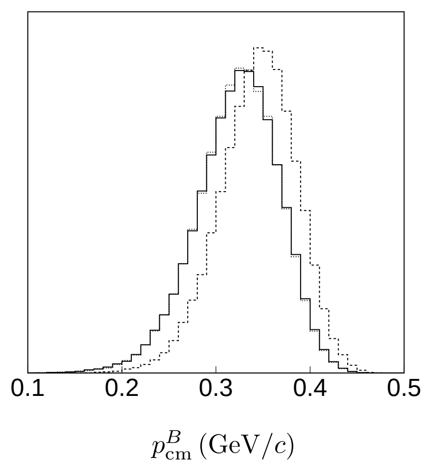

Figure 5.5: B meson momentum distributions for default $B\overline{B}$ MC (dotted line), corrected default $B\overline{B}$ MC (solid line), and corrected at the generator level $B\overline{B}$ MC (dashed line). The correction applied acts to transform the "dotted" line spectrum to that of the "solid" line, therefore conforming to the case of a correct beam energy in the MC as given by the "dashed" line spectrum.

QED radiative corrections The MC does not include effects of QED radiative corrections, where photons are radiated in the final state ($B \rightarrow X e \nu_e \gamma$). These are not to be confused with subsequent Bremsstrahlung energy loss from interaction of the electron with the detector. QED radiative correction, also known as final state radiation loss, was studied using the `PHOTOS` package[62]. `PHOTOS` simulates the photon emission from the decay electron on an event by event basis. It uses a leading-log approximation for the bremsstrahlung matrix element. The `PHOTOS` simulation of the electron spectrum of $B \rightarrow D e \nu_e$ has been found to agree to within 10% of an exact $\mathcal{O}(\alpha)$ calculation[63].

Four million $B \rightarrow X_c e \nu_e$ simulated events generated with and without `PHOTOS` implemented were used to construct weighting histograms in generated electron momentum. These histograms were used to reweight the $B\overline{B}$ MC sample so as to include the QED radiative effects on the reconstructed

MC momentum spectrum. Figure 5.6 shows the generated electron momentum spectrum with and without PHOTOS implemented.

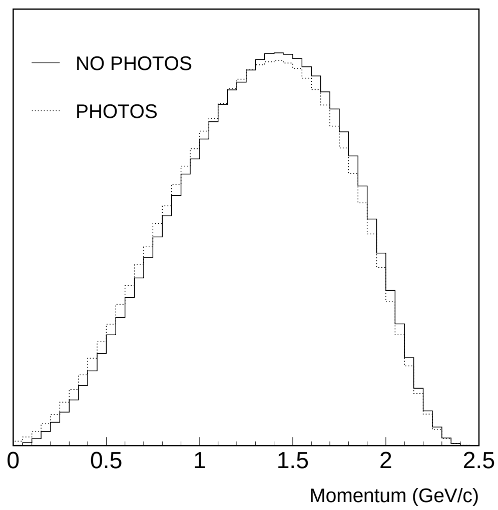

Figure 5.6: Semileptonic B meson decay electron spectra with and without using the PHOTOS package.

Form factors for $B \to D^*/De\nu_e$ The differential partial decay width for $B \to D^*e\nu$ in HQET is given by:

$$\frac{d\Gamma}{dw}(B \to D^*l\nu) = \frac{G_F^2|V_{cb}|^2}{48\pi^3}\mathcal{K}_{\mathcal{D}}(w)\mathcal{F}(w)^2, \tag{5.11}$$

where w is the inner product of the B and D^* meson 4-velocities (and is directly related to the leptonic mass q^2), $\mathcal{K}_{\mathcal{D}}$ is the phase space factor, and $\mathcal{F}(w)$ is the form factor (FF). In the MC, the $B \to D^*l\nu$ component is modelled using a linear approximation for the form factor, which has since been shown to be inaccurate[4]. The latest measurements of the spectrum assume a non-linear shape for the form factor function, which is parameterised by the slope of the form factor at zero recoil ($w = 1$), ρ^2. The MC is re-weighted in q^2 according to the non-linear shape given in reference[64] with the slope parameter set to the world average value, $\rho^2 = 1.51 \pm 0.13$[17]. Additional information necessary to specifying the decay dynamics are the vector and axial form factor ratios, R_1 and R_2. These were set according to CLEO measurements[65], $R_1 = 1.18$ and $R_2 = 0.71$, as was done in the determination of the ρ^2 world average. The QQ98 and re-modelled q^2 spectra are compared in figure 5.7a.

In the MC $B \to De\nu_e$ decays were generated assuming the ISGW2 form factor model. It is re-weighted according to the HQET-based parameterisation given in reference[64], with the form factor

[4] A discussion can be found in the V_{cb} review article appearing in the 2002 Review of Particle Physics[17]

slope variable set to the world average value $\rho_D^2 = 1.19 \pm 0.19$[17]. The respective q^2 spectra are compared in figure 5.7b.

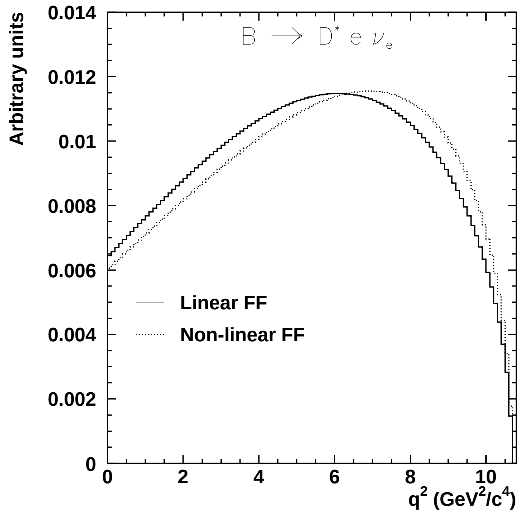

(a)

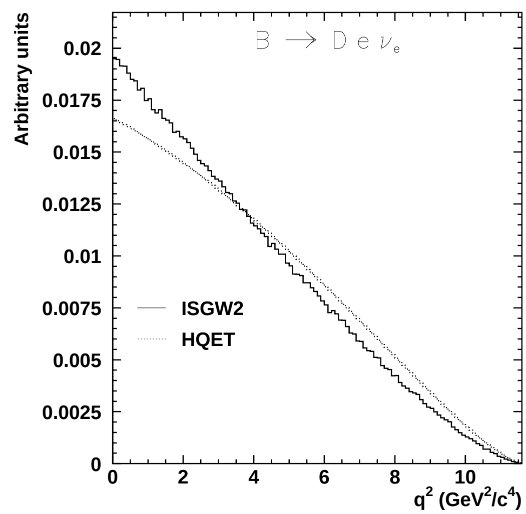

(b)

Figure 5.7: Differential q^2 decay distributions for (a) $B \rightarrow D^* e\nu$, where FF refers to form factor and (b) $B \rightarrow De\nu$.

Makeup of $B \rightarrow D^{**} e\nu_e$ Following the prescription in the Belle $m_X - q^2$ V_{ub} analysis[66, 67], the better known subcomponents were required to satisfy

$$R_{D^{**}} = \frac{\mathcal{B}(B \rightarrow D_1(2420)l\nu) + \mathcal{B}(B \rightarrow D_2^*(2460)l\nu)}{\mathcal{B}(B \rightarrow D^{**}l\nu)} = 0.45 \pm 0.25, \tag{5.12}$$

which has been derived by averaging maximum and minimum assessments of each of the branching fractions in the above expression. In the fit $R_{D^{**}}$ is fixed to 0.45.

Relative $B \rightarrow D^*/De\nu_e$ proportions To better constrain the fit,

$$\frac{\mathcal{B}(B \rightarrow D^* l\nu)}{\mathcal{B}(B \rightarrow Dl\nu)} = 2.80 \pm 0.23, \tag{5.13}$$

which has been calculated as a mean over world average values (2003) of neutral and charged modes[5],

$$\mathcal{B}(B \rightarrow D^* l\nu) = \frac{1}{2}((5.53 \pm 0.23) + (6.5 \pm 0.5)) = (6.015 \pm 0.28)\% \tag{5.14}$$

$$\mathcal{B}(B \rightarrow Dl\nu) = \frac{1}{2}((2.15 \pm 0.22) + (2.14 \pm 0.20)) = (2.145 \pm 0.14)\%. \tag{5.15}$$

[5]The use of the PDG world averages for 2003 is justified given the large increase observed in the $\mathcal{B}(B \rightarrow D^* l\nu_l)$ world average between 2002 and 2003. The information is given in Appendix B (see Particle Data Group 2003 archives at http://pdg.lbl.gov)

Consequently in the fit the ratio of the rates was fixed to 2.80

Before fitting, the above corrections were incorporated into the $B\overline{B}$ MC. The fits were conducted using the `HBOOK`[68] routine, `HMCMLL`[69]. The `HMCMLL` routine receives histograms as inputs and implements a binned maximum likelihood fit. The likelihood takes into account the bin to bin statistical fluctuations of the fitting components.

The fit determines the fraction of each of the floated components with the constraint that all the fractions sum to unity. The fit fractions are converted to normalisation factors for the $B \to X_c e\nu_e$ calibrated MC yields found in the signal region.

The fit components are displayed in figure 5.8 and are as follows:

- OFF resonance data (Continuum background) - fixed (Fig. 5.8(a));
- MC Fakes and secondary electron - fixed (Fig. 5.8(b));
- MC $B \to (D + D^*)e\nu$ - floated (Fig. 5.8(c));
- MC $B \to D^{**}e\nu$ - floated (Fig. 5.8(d));
- MC $B \to D^{(*)}\pi e\nu_e$ - floated (Fig. 5.8(e));
- MC $B \to X_u e\nu$ - fixed for all but the $1.5 < p_{\mathrm{cm}}/\mathrm{GeV}/c < 2.2$ fit (fixed to the Belle measurement $\mathcal{B}(B \to X_u e\nu) = (2.27 \pm 0.60) \times 10^{-3}$[66]) (Fig. 5.8(f)).

The fit results for the $1.5 < p_{\mathrm{cm}}/\mathrm{GeV}/c < \{1.9, 2.0, 2.1, 2.2\}$ intervals are displayed in Figures 5.9, 5.10, 5.11 and 5.12 respectively.

The goodness of fit was estimated by calculating a χ^2 given by

$$\chi^2 = \sum_i \frac{(d_i - f_i)^2}{\sigma^2_{d_i}}, \tag{5.16}$$

where d and f are the data and fitted yields respectively, i denotes the bin, and σ_d is the data yield uncertainty. All the fits have acceptable χ^2 values.

The D^{**} and $D^{(*)}\pi$ components have very similar momentum spectra, only slight variations are evident at higher momenta, as such the fits showed a preference for either of the two contributions.[6] This phenomenon is here after called $D^{(*)}\pi/D^{**}$ mode switching. It's problematic in the estimation of systematic uncertainties because it tends to occur when fit quantities are varied about their errors. Its impact is discussed in the next subsection.

Inclusive semileptonic branching ratios calculated from the fits provide consistency checks but are subject to large uncertainties from model dependent efficiency calculations for each of the charmed background components. With an uncertainty of the order of 10%, each measurement is found to be consistent

[6] This behaviour was also evident in the CLEO analysis for a D^* former factor variation introduced for a systematic error calculation[30]:page 157, Table 4.8. It occurs more often in this analysis.

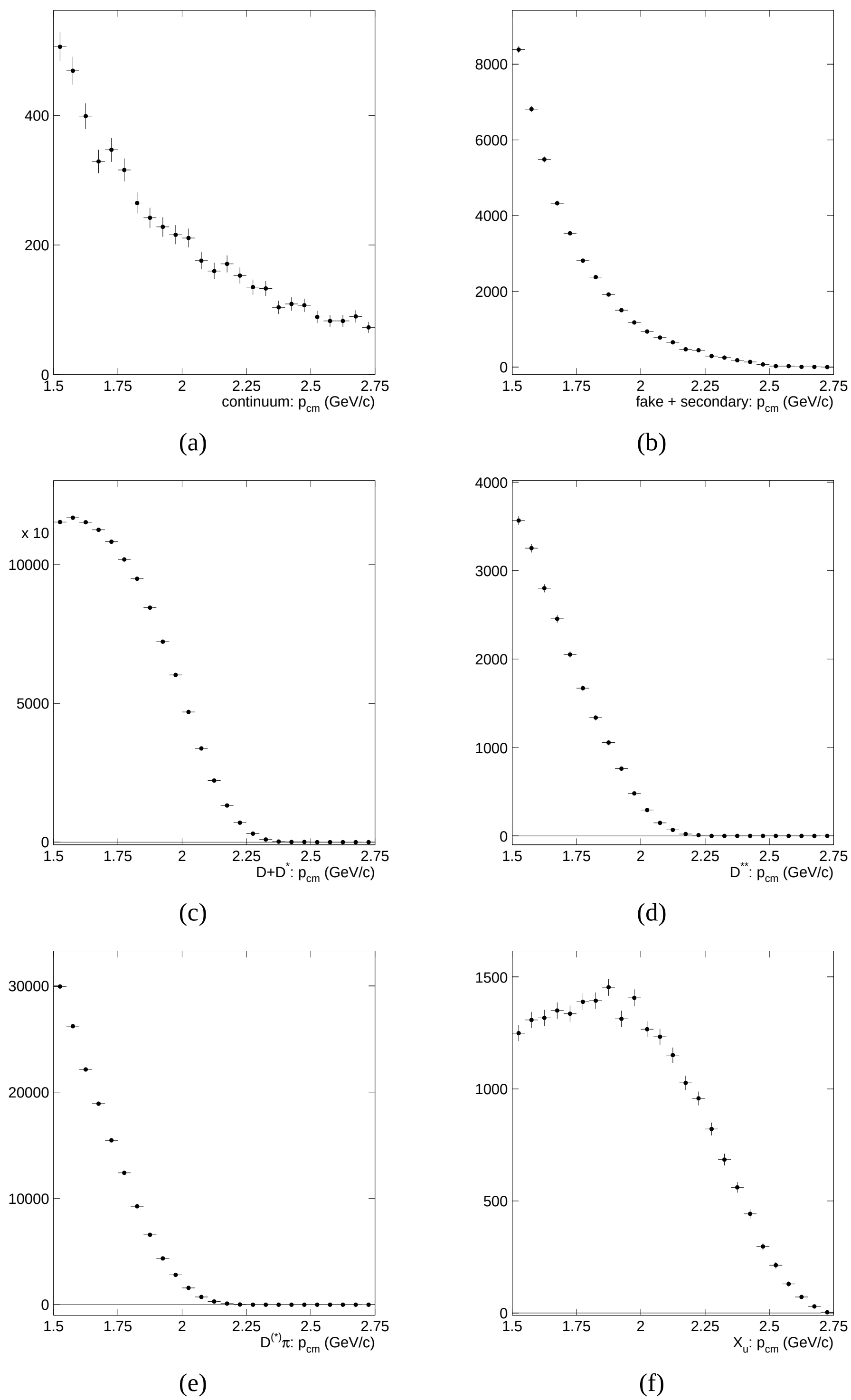

Figure 5.8: Lower sideband fit components: (a) continuum, (b) fakes and secondary, (c) D and D^{*}, (d) D^{**}, (e) $D^{(*)}\pi$, and (f) X_u.

with the world average value of $(10.70 \pm 0.28)\%$. Moreover, the exclusive combined branching fractions, $B \to (D + D^*)e\nu_e$, for all fits are found to be consistent with the world averages.

5.4.1 Systematic uncertainties

The systematic uncertainties in the charmed semileptonic B meson decay background yields have been assessed by varying fixed constraints in the fits by their uncertainties($\pm 1\sigma$). This included the variation: of the form factor slope variables for D^* and D; the ratio of the branching fractions for $B \to D^* e\nu_e$ to $B \to De\nu_e$; of known higher mass charm resonances with respect to the overall contribution, $R_{D^{**}}$; the $B \to X_u e\nu_e$ branching fraction where applicable; of the beam energy; to the mainly ISGW2 modelled signal MC; to the case of no non-resonant charmed background; and no final state radiation loss correction.

The observed change in the estimated background is assigned as a systematic uncertainty. In the case of a symmetric variation($\pm 1\sigma$), the maximum of the observed changes was assigned as the uncertainty. The total uncertainty was calculated as the quadratic sum of the individual uncertainties. The results are given in table 5.8.

The uncertainties associated with the fake, secondary and continuum backgrounds in the lower sideband fit were found to be negligible. In general the greatest uncertainty was derived from the variation in the $B \to D^* e\nu_e$ form factor slope. It was to be expected as it is the largest background. For the fit in the momentum interval $1.5 < \frac{p_{\rm cm}}{{\rm GeV}/c} < 2.2$, the signal component, which was left to float, was found to give $\mathcal{B}(B \to X_u e\nu_e) = (0.256 \pm 0.037)\%$ (statistical error only). In the other three sideband fits it was fixed, and the variation of the assumed branching fraction caused the second largest source of systematic uncertainty.

The systematic changes in the momentum interval, $2.2 < p_{\rm cm}/{\rm GeV}/c < 2.6$, yielded similar changes in the X_c yield. As the momentum interval is widened the behaviour with respect to the makeup of the charmed background is somewhat erratic because of $D^{(*)}\pi/D^{**}$ mode switching. The results for varying $R_{D^{**}}$ for the momentum interval $1.9 < p_{\rm cm}/{\rm GeV}/c < 2.6$, gave the change in the X_c yield for $R_{D^{**}} = 0.70$ equal to -4.7 while for $R_{D^{**}} = 0.20$ it was equal -755.3. By assigning the maximum observed change as the systematic uncertainty, the mode switching effect is taken into account in the uncertainty.

In addition, to ensure the uncertainty is not being under estimated a systematic error is assigned according to the observed change when no non-resonant ($B \to D^{(*)}\pi e\nu_e$) component is included in the fits.

The efficiency for selecting $B \to X_c l\nu$ events

The $B \to X_c e\nu$ momentum spectra are modelled using the $B\overline{B}$ MC sample. As detailed in the previous subsection, great effort was made to calibrate the various components. Another source of discrepancy between MC and data may come about from the response to the event selection cuts. The effect of the

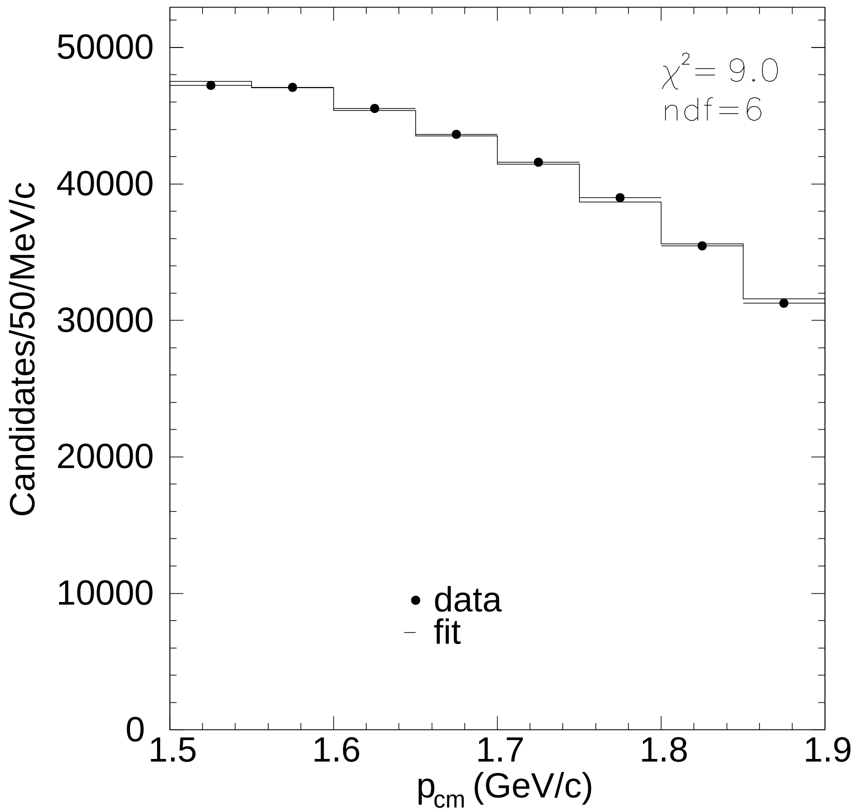

ON	# Candidates = 330780	
Source	Fraction	Error
OFF	0.0261	fixed
Fakes+secondary	0.0281	fixed
$B \to (D + D^*)l\nu$	0.8669	0.0071
$B \to D^{**}l\nu$	0.0000	0.0027
$B \to D^{(*)}\pi l\nu$	0.0573	0.0126
$B \to X_u l\nu$	0.0216	fixed
EDM	0.00126915	
ISTAT	3	
χ^2	9.0	
NDF	6	

Figure 5.9: The lower sideband fit $1.5 < p_{\mathrm{cm}}/(\mathrm{GeV/c}) < 1.9$ ("EDM" and "ISTAT" are parameters specific to `MINUIT`[70] which is called by `HBOOK`. "EDM" is the vertical distance remaining to the minimum. "ISTAT" is a status integer indicating how good is the covariance matrix: 0 - Not calculated at all; 1 - Diagonal approximation only, not accurate; 2 - Full matrix, but forced positive definite; 3 - Full accurate covariance matrix).

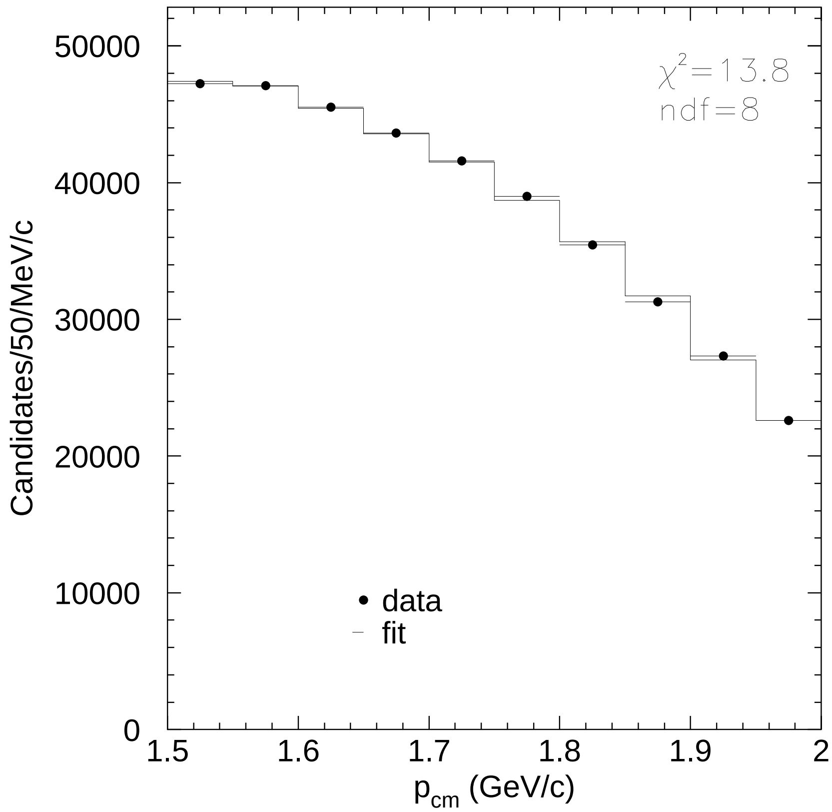

ON	# Candidates = 380686	
Source	Fraction	Error
OFF	0.0262	fixed
Fakes+secondary	0.260	fixed
$B \to (D + D^{*})l\nu$	0.8640	0.0060
$B \to D^{**}l\nu$	0.0603	0.0110
$B \to D^{(*)}\pi l\nu$	0.0000	0.0047
$B \to X_u l\nu$	0.0235	fixed
EDM	0.00043595	
ISTAT	3	
χ^2	13.8	
NDF	8	

Figure 5.10: The lower sideband fit $1.5 < p_{\rm cm}/({\rm GeV/c}) < 2.0$ ("EDM" and "ISTAT" are parameters specific to `MINUIT`[70] which is called by `HBOOK`."EDM" is the vertical distance remaining to the minimum. "ISTAT" is a status integer indicating how good is the covariance matrix: 0 - Not calculated at all; 1 - Diagonal approximation only, not accurate; 2 - Full matrix, but forced positive definite; 3 - Full accurate covariance matrix).

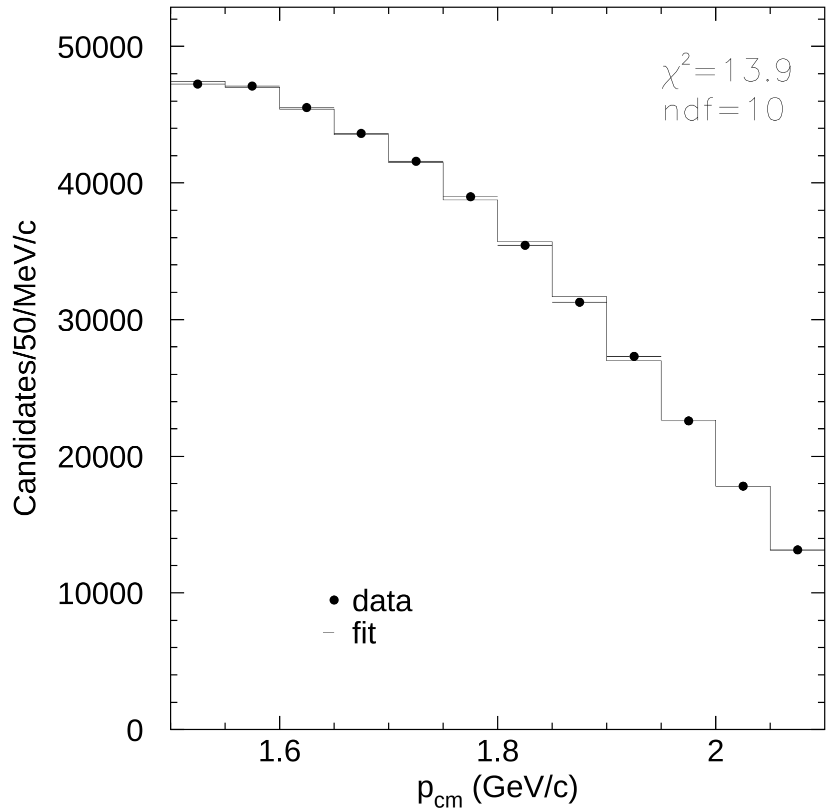

ON	# Candidates = 411635	
Source	Fraction	Error
OFF	0.0270	fixed
Fakes+secondary	0.250	fixed
$B \to (D + D^*)l\nu$	0.8767	0.0042
$B \to D^{**}l\nu$	0.0001	0.0002
$B \to D^{(*)}\pi l\nu$	0.0454	0.0045
$B \to X_u l\nu$	0.0258	fixed
EDM	1.35844E-05	
ISTAT	3	
χ^2	13.9	
NDF	10	

Figure 5.11: The lower sideband fit $1.5 < p_{\rm cm}/({\rm GeV/c}) < 2.1$ ("EDM" and "ISTAT" are parameters specific to `MINUIT`[70], which is called by `HBOOK`. "EDM" is the vertical distance remaining to the minimum. "ISTAT" is a status integer indicating how good is the covariance matrix: 0 - Not calculated at all; 1 - Diagonal approximation only, not accurate; 2 - Full matrix, but forced positive definite; 3 - Full accurate covariance matrix).

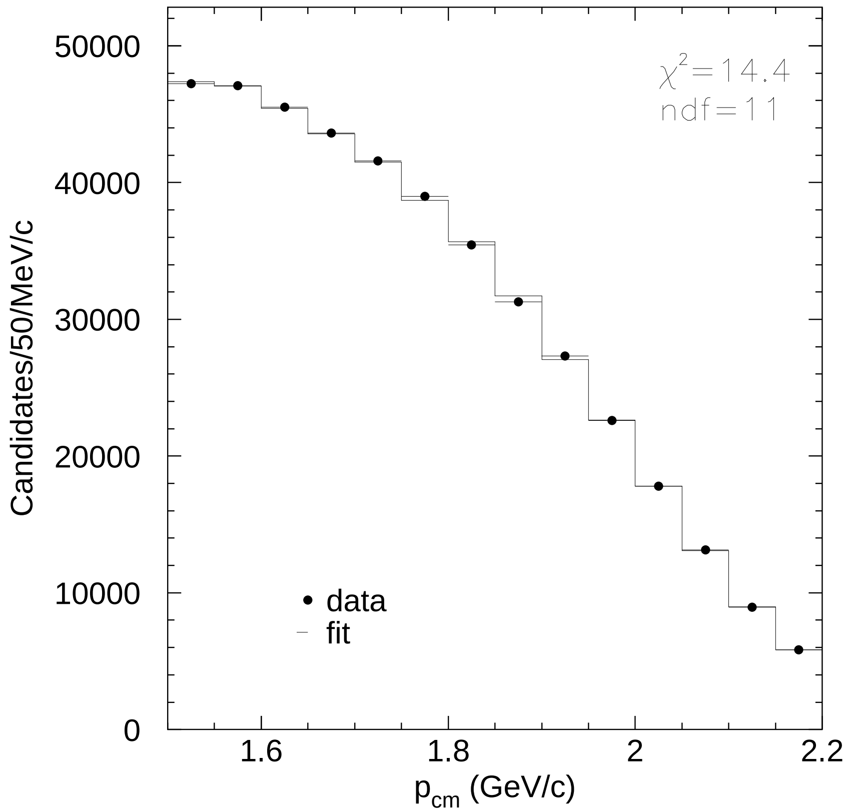

ON	# Candidates = 426398	
Source	Fraction	Error
OFF	0.0284	fixed
Fakes+secondary	0.0246	fixed
$B \to (D + D^{*})l\nu$	0.8597	0.0098
$B \to D^{**}l\nu$	0.0510	0.0068
$B \to D^{(*)}\pi l\nu$	0.0045	0.0023
$B \to X_u l\nu$	0.0318	0.0046
EDM	0.00985677	
ISTAT	3	
χ^2	14.4	
NDF	11	

Figure 5.12: The lower sideband fit $1.5 < p_{\mathrm{cm}}/(\mathrm{GeV/c}) < 2.2$ ("EDM" and "ISTAT" are parameters specific to `MINUIT`[70] which is called by `HBOOK`. "EDM" is the vertical distance remaining to the minimum. "ISTAT" is a status integer indicating how good is the covariance matrix: 0 - Not calculated at all; 1 - Diagonal approximation only, not accurate; 2 - Full matrix, but forced positive definite; 3 - Full accurate covariance matrix).

	$x < p_{\rm cm}/\mathrm{GeV}/c < 2.6$					
x	1.9	2.0	2.1	2.2	2.3	2.4
D^* form factor slope						
$\rho^2 = 1.64$	1255.3	744.3	230.1	186.7	21.6	0.1
$\rho^2 = 1.38$	-1335.5	-528.6	-391.5	-144.6	-16.8	-0.1
D form factor slope						
$\rho_D^2 = 1.38$	-269.0	-142.4	-83.1	-45.9	-8.1	-0.2
$\rho_D^2 = 1.00$	217.2	117.0	-45.4	31.3	6.0	0.2
Relative $B \to D^*/De\nu_e$ rates						
$R_{D^*/D} = 3.03$	-76.3	-80.0	-40.3	-32.1	-6.6	-0.2
$R_{D^*/D} = 2.57$	83.9	90.7	47.3	28.3	6.6	0.2
Higher mass charm meson proportions						
$R_{D^{**}} = 0.70$	-4.7	278.1	0.1	53.6	5.9	0.1
$R_{D^{**}} = 0.20$	-755.3	-119.5	-0.3	-30.4	-3.5	-0.0
$B \to X_u e\nu_e$ branching fraction						
$\mathcal{B}(B \to X_u e\nu_e) = 0.287\%$	-746.2	-271.8	-320.0	n/a	n/a	n/a
$\mathcal{B}(B \to X_u e\nu_e) = 0.167\%$	745.7	627.4	191.7	n/a	n/a	n/a
Beam energy variation						
$E_{beam} = 5.28877\,\mathrm{GeV}$	104.4	103.6	84.4	48.2	10.0	0.0
$E_{beam} = 5.28849\,\mathrm{GeV}$	-90.0	-95.1	-75.7	-46.5	-13.2	0.0
Signal component modelling						
ISGW2	52.1	-6.4	-135.4	31.8	3.1	0.0
Removal of non-resonant charmed component						
No $B \to D^{(*)}\pi e\nu_e$	-380.7	17.7	-119.9	-3.9	0.5	0.0
Removal of final state radiation loss correction						
No PHOTOS	-25.1	155.6	-54.6	28.4	2.6	0.1
Total	1774.7	1043.4	455.3	212.2	28.3	0.3

Table 5.8: Systematic uncertainties in the estimation of the $B \to X_c e\nu_e$ background.

$\mathcal{F}_{\text{flow}}\,(kl1)$ and $\cos\theta_{\text{Thrust}-\text{A}}$ cuts were investigated in a control sample that consisted of inclusive $J/\psi \rightarrow e^+e^-$ decays in $B\overline{B}$ events.

The $B \rightarrow J/\psi(\rightarrow e^+e^-)X$ for the most part can be represented as $X_s e^+e^-$, by regarding one of the electrons as the neutrino it's evident that $X_s e\nu$ has event topology and final *strangeness* content similar to $X_c(\rightarrow X_s)e\nu$[7]. The similar final state *strangeness* content has the effect of preserving the $kl1$ dependence in the $\mathcal{F}_{\text{flow}}$ cut. However, the sample is monochromatic in q^2, where necessarily $q^2 = m^2_{J/\psi} = 9.6\,\text{GeV}^2/c^4$.

The decay $J/\psi \rightarrow e^+e^-$ was reconstructed in both ON and OFF sample data and $B\overline{B}$ MC. The J/ψ daughter with the highest momentum was assigned as the electron candidate and was therefore required to meet the same track and electron ID requirements as the candidates considered in this analysis. The other electron candidate was assigned as the neutrino, and therefore, was treated as a missing particle in the $\mathcal{F}_{\text{flow}}\,(kl1)$ and $\cos\theta_{\text{Thrust}-\text{A}}$ variable calculations.

J/ψ candidates were reconstructed within the mass window, $2.7 < m_{e^+e^-}/\text{GeV}/c^2 < 3.4$. Distributions of J/ψ candidates from $B\overline{B}$ events were obtained by subtracting scaled OFF data from ON data. The J/ψ signal yield was calculated from a fit to the mass spectrum; whereby a `CRYSTAL BALL` line shape and exponential function were used to model the signal and background components respectively. J/ψ yields were likewise obtained in the $B\overline{B}$ MC sample.

The selection efficiency as a result of the $\mathcal{F}_{\text{flow}}\,(kl1)$ and $\cos\theta_{\text{Thrust}-\text{A}}$ cuts was measured as the after to before cut ratio of yields. Yields were extracted for candidate electron momentum in the range $1.5 < p_{\text{cm}}/\,\text{GeV}/c < 2.5$, in $0.05\,\text{GeV}/c$ bins. The cut efficiency is plotted for both data and MC in figure 5.13a, along with the resultant data to MC efficiency ratio in figure 5.13b, which is fit with a constant plus a slope. There is no apparent bias as a function of momentum since the slope is negligible, the error on the slope places a limit on the systematic bias at the level of 5%, and is insignificant when compared to the systematic effects discussed previously. The value of the constant is 0.97 ± 0.01, which is a slight downward shift from unity. This shift is of no consequence to the analysis as the $B \rightarrow X_c e\nu_e$ components are not fixed in the lower sideband fits, and therefore the fit can compensate for the shift.

5.4.2 Summary

The resultant $B \rightarrow X_c e\nu_e$ background yields are given in table 5.9. The first error derives from MC statistics and the second error is the systematic uncertainty. The uncertainty in the knowledge of the D^* form factor dominates the error.

[7] The use of $B \rightarrow J/\psi(\rightarrow e^+e^-)X$ as a control sample was used first in the Belle $q^2 - M_X$ V_{ub} analysis[67]

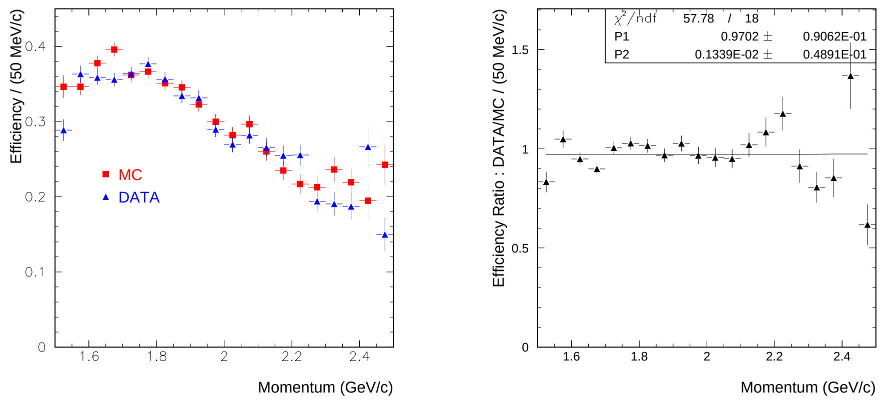

(a) (b)

Figure 5.13: (a) The combined $\mathcal{F}_{\text{flow}}\,(kl1)$ and $\cos\theta_{\text{Thrust}-\text{A}}$ cut efficiencies in data and MC as extracted from the $B \to J/\psi X$ control sample and (b) the resultant data to MC efficiency ratio as a function of the momentum.

p_{cm} (GeV/c)	$N_{B\to X_c e\nu_e}$
$1.9 - 2.6$	$88955.7 \pm 174.3 \pm 1774.7$
$2.0 - 2.6$	$43218.4 \pm 123.8 \pm 1043.4$
$2.1 - 2.6$	$15798.5 \pm 73.9 \pm 455.3$
$2.2 - 2.6$	$3686.4 \pm 35.6 \pm 212.2$
$2.3 - 2.6$	$348.7 \pm 10.9 \pm 28.3$
$2.4 - 2.6$	$3.6 \pm 1.1 \pm 0.3$

Table 5.9: Candidates from charmed semileptonic B meson decays, where the first error is statistical and the second is systematic.

5.5 Endpoint $B \to X_u e\nu_e$ yields

The signal yields are calculated by subtracting each of the backgrounds from the ON yield,

$$N_{B\to X_u e\nu_e} = N_{\rm ON} - (\alpha N_{\rm OFF} + N_{\rm Fakes} + N_{B\to X\to e} + N_{B\to J/\psi\to e} + N_{B\to X_c e\nu_e}), \tag{5.17}$$

these are given in table 5.10 for all the overlapping momentum intervals.

$p_{\rm cm}$ (GeV/c)	$2.4-2.6$	$2.3-2.6$	$2.2-2.6$
$N_{\rm ON}$	1741.0 ± 41.7	3534.0 ± 59.4	8854.0 ± 94.1
$\alpha N_{\rm OFF}$	$1165.8\pm59.2\pm4.7$	$1877.8\pm75.1\pm7.6$	$2743.1\pm90.8\pm11.1$
Fakes	$11.1\pm1.6\pm3.3$	$39.9\pm2.9\pm12.0$	$79.3\pm4.2\pm23.8$
$N_{B\to J/\psi\to e}$	$39.9\pm3.2\pm3.0$	$93.7\pm5.0\pm7.0$	$191.4\pm7.\pm14.3$
$N_{B\to X\to e}$	$7.8\pm1.4\pm0.8$	$23.1\pm2.4\pm2.7$	$53.5\pm3.6\pm6.1$
$N_{B\to X_c e\nu_e}$	$3.6\pm1.1\pm0.3$	$348.7\pm10.9\pm28.3$	$3686.4\pm35.6\pm212.2$
$N_{B\to X_u e\nu_e}$	$512.8\pm72.5\pm6.5$	$1150.8\pm96.6\pm32.5$	$2100.3\pm135.8\pm214.4$

$p_{\rm cm}$ (GeV/c)	$2.1-2.6$	$2.0-2.6$	$1.9-2.6$
$N_{\rm ON}$	23617.0 ± 153.7	54566.0 ± 233.6	104472.0 ± 323.2
$\alpha N_{\rm OFF}$	$3737.6\pm106.0\pm15.2$	$4900.3\pm121.3\pm19.9$	$6234.3\pm136.9\pm25.3$
Fakes	$129.1\pm5.3\pm38.7$	$176.8\pm6.2\pm53.0$	$231.4\pm7.1\pm69.4$
$N_{B\to J/\psi\to e}$	$339.0\pm9.5\pm25.4$	$569.0\pm12.3\pm42.7$	$889.6\pm15.4\pm66.7$
$N_{B\to X\to e}$	$129.8\pm5.9\pm15.0$	$269.8\pm9.5\pm34.4$	$567.6\pm17.6\pm75.0$
$N_{B\to X_c e\nu_e}$	$15798.5\pm73.9\pm455.3$	$43218.4\pm123.8\pm1043.4$	$88955.7\pm174.3\pm1774.7$
$N_{B\to X_u e\nu_e}$	$3483.0\pm201.2\pm458.2$	$5431.7\pm291.4\pm1046.4$	$7593.3\pm392.6\pm1779.0$

Table 5.10: The $B \to X_u e\nu_e$ endpoint yields, where the first error is statistical and the second is systematic.

5.6 Corrected End-Point Electron Spectrum

The background subtracted and efficiency corrected data spectrum attributed to $B \to X_u e\nu_e$ is shown in figure 5.14, overlay-ed is a histogram representing an expectation of the spectrum shape, which has been derived using information from a fit to the Belle measured $B \to X_s\gamma$ photon energy spectrum (as detailed in the next chapter). In order to construct the plot, systematic and statistical uncertainties for signal yields and efficiencies were calculated for each momentum bin. The net error is the quadratic sum of the statistical and systematic errors. There is a bin-to-bin correlation in the errors.

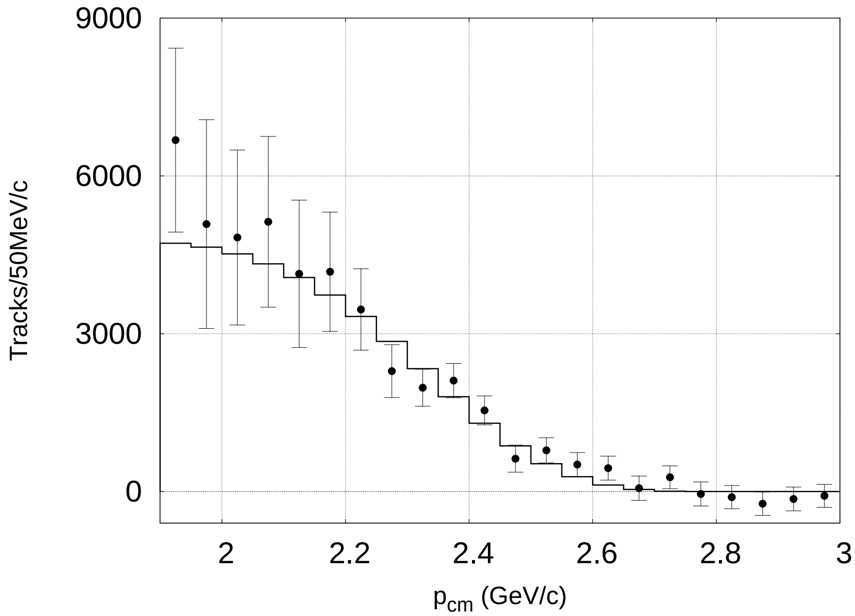

Figure 5.14: The electron momentum spectrum attributed to $B \to X_u e \nu_e$ for background subtracted efficiency corrected data (black circles) and a theoretical prediction based on measurements of the $B \to X_s \gamma$ spectrum and calculated using the De Fazio and Neubert prescription with an exponential model for the b-quark shape function, where $(\Lambda^{\mathrm{SF}}, \lambda_1^{\mathrm{SF}}) = (0.66\,\mathrm{GeV}/c^2, -0.40\,\mathrm{GeV}^2/c^2)$ (histogram). The histogram has been normalised according to the net signal yield in the region $2.2 < p_{\mathrm{cm}}/\mathrm{GeV}/c < 2.6$.

Chapter 6

Extracting $|V_{ub}|$

6.1 Partial branching fractions

The partial branching fractions are calculated as

$$\Delta\mathcal{B}(B \to X_u e \nu_e) = \frac{N(B \to X_u e \nu_e)(\Delta p)}{2N_{B\overline{B}}\epsilon_{\mathrm{MC}}(\Delta p)}, \tag{6.1}$$

where $N(B \to X_u e \nu_e)(\Delta p)$ is the signal yield (given in section 5.6) and $\epsilon_{\mathrm{MC}}(\Delta p)$ is the signal reconstruction efficiency (given in section 4.6.5), as measured in the momentum interval denoted Δp. The number of B mesons contained in the analysed data set is given by $2N_{B\overline{B}}$, where $N_{B\overline{B}}$ is the number of $B\overline{B}$ events (given in section 4.4). The calculated partial branching fractions for the six momentum intervals considered are given in table 6.1. The first error is due to statistics and the second, which includes the uncertainty in $N_{B\overline{B}}$ and the efficiency, is systematic. The systematic uncertainty more or less doubles as the interval is increased by $100\,\mathrm{MeV}/c$.

Momentum interval (GeV/c)	$\Delta\mathcal{B}(B \to X_u e \nu_e)$ (10^{-4})
1.9-2.6	$7.59 \pm 0.39 \pm 1.83$
2.0-2.6	$5.56 \pm 0.30 \pm 1.11$
2.1-2.6	$3.66 \pm 0.21 \pm 0.52$
2.2-2.6	$2.28 \pm 0.15 \pm 0.26$
2.3-2.6	$1.29 \pm 0.11 \pm 0.08$
2.4-2.6	$0.59 \pm 0.08 \pm 0.04$

Table 6.1: Partial branching fractions in overlapping momentum intervals, the first error is statistical and the second is systematic.

6.1.1 Stability studies

To investigate the stability of the partial branching fraction measurements to the main event selection criteria, namely continuum suppression cuts: $\mathcal{F}_{\mathrm{flow}}\,(kl1)$; and $\cos\theta_{\mathrm{Thrust-A}}$, the analysis was redone for multiple cut variations. The variations are listed in table 6.2. They examine the the effect of relaxing and tightening the continuum cuts. The measured partial branching fractions are plotted in figure 6.1 and figure 6.2 for the $\mathcal{F}_{\mathrm{flow}}\,(kl1)$ and $\cos\theta_{\mathrm{Thrust-A}}$ cuts, respectively. No significant trends are evident. In general, the greatest fractional changes are observed for the narrower momentum intervals, this is due to statistical fluctuations encountered in the OFF resonance data sample, for which the selection efficiency varies greatly as a function of the cut.

The analysis was also redone for the cut

$$\mathcal{F}_{\mathrm{flow}} > 0.70, \tag{6.2}$$

where the cut chosen was optimal and independent of $kl1$. All the branching fraction measurements were found to be less than 2% smaller than the default value, with the exception of the measurement in the narrowest interval, which was found to differ by -3.1%. Since this is the first time a $kl1$ type variable has been used in an endpoint analysis, conservatively, the deviation was assigned as a systematic uncertainty, which has been included in the errors shown in table 6.1.

$\mathcal{F}_{\mathrm{flow}}$ cut index	$\mathcal{F}_{\mathrm{flow}}\,(kl1)$ cut $kl1<0$	$kl1=0$	$kl1>0$	$\cos\theta_{\mathrm{Thrust-A}}$
1	>0.2	>0.3	>0.8	<0.75
2	>0.3	>0.4	>0.9	<0.75
3	>0.4	>0.5	>1.0	<0.75
$4^{\dagger}$	>0.5	>0.6	>1.1	<0.75
5	>0.6	>0.7	>1.2	<0.75
6	>0.7	>0.8	>1.3	<0.75
7	>0.8	>0.9	>1.4	<0.75
$\cos\theta_{\mathrm{Thrust-A}}$ cut index	$\mathcal{F}_{\mathrm{flow}}\,(kl1)$ cut $kl1<0$	$kl1=0$	$kl1>0$	$\cos\theta_{\mathrm{Thrust-A}}$
1	>0.5	>0.6	>1.1	<0.95
2	>0.5	>0.6	>1.1	<0.85
$3^{\dagger}$	>0.5	>0.6	>1.1	<0.75
4	>0.5	>0.6	>1.1	<0.65
5	>0.5	>0.6	>1.1	<0.55

Table 6.2: Labels and definitions of cuts used in the stability study.. † - the default cut used in this analysis.

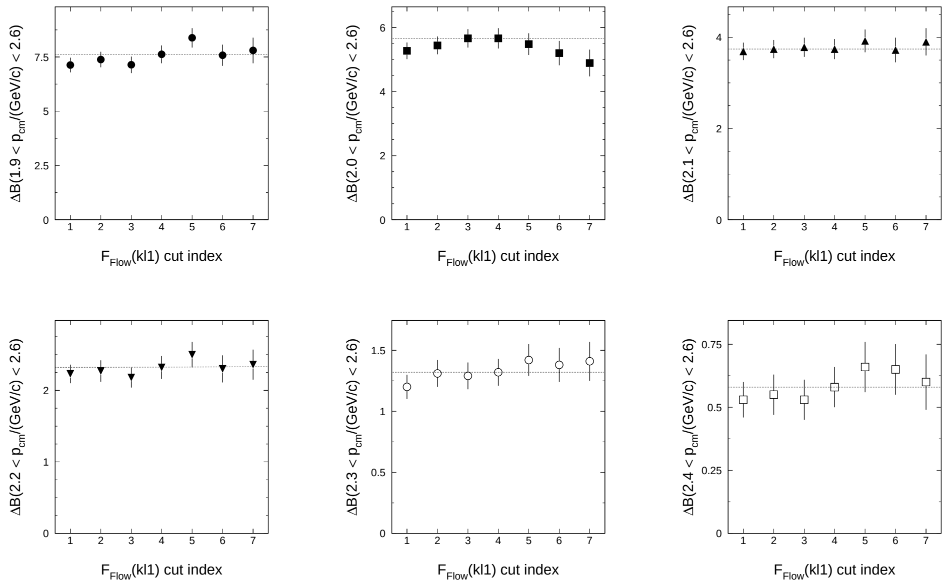

Figure 6.1: Measured partial branching fractions for the $\mathcal{F}_{\rm flow}\,(kl1)$ cut scan. The errors are statistical and there is bin to bin correlation. The most relaxed cut configuration has 3 times greater signal efficiency than the most stringent cut, corresponding to roughly double and half the default efficiency, respectively. The dotted line represents the value obtained for the default cut ($\mathrm{index} = 4$).

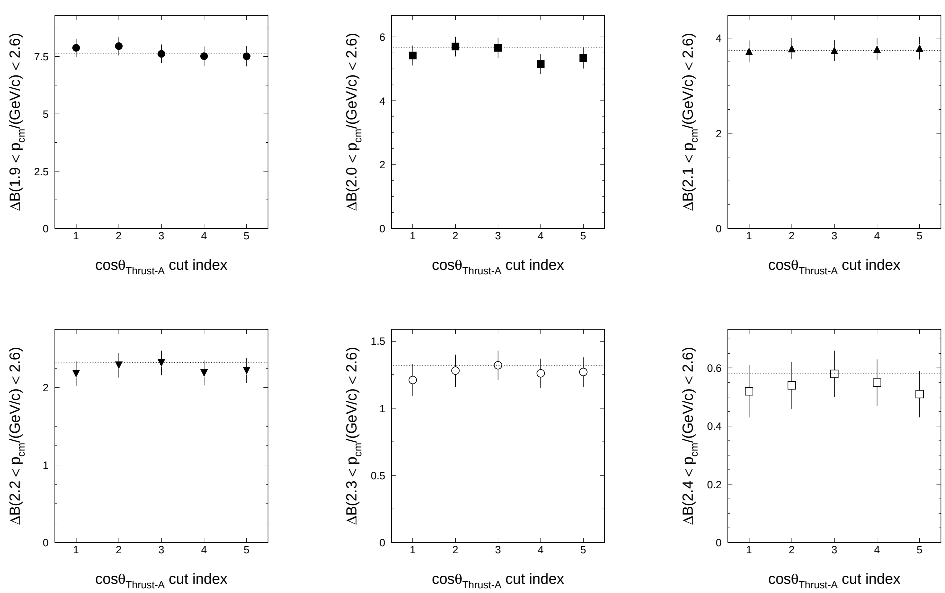

Figure 6.2: Measured partial branching fractions for the $\cos\theta_{\rm Thrust-A}$ cut scan. The errors are statistical and there is bin to bin correlation. The most relaxed cut configuration has 0.3 times greater signal efficiency than the most stringent cut. The dotted line represents the value obtained for the default cut ($\mathrm{index} = 3$).

6.2 The spectral fractions f_u

To extract values for $|V_{ub}|$ the partial branching fraction measurements must be extrapolated to the full phase space using spectral fractions, f_u, such that

$$\mathcal{B}(B \to X_u e \nu_e) = \frac{\Delta\mathcal{B}(B \to X_u e \nu_e)(\Delta p)}{f_u(\Delta p)}. \tag{6.3}$$

The CLEO collaboration were the first to derive f_u from their measured $B \to X_s\gamma$ photon energy spectrum[29]. Previously they were extracted from models. The following subsections describe a method based on that devised by CLEO[14, 30], as applied to the Belle measured spectrum[71]. The results of the study to extract the shape function parameters also appear in reference [72].

From an experimentalists' point of view it is natural to talk about the momentum, as opposed to the energy, since the former is measured to a greater precision than the latter. Theorists phrase discussions of the spectral fractions in terms of energy. Their convention is adhered to in this section. Owing to the electron's relatively tiny mass, there is a negligible difference between the magnitude of its momentum and energy, therefore energy and momentum spectral fractions are equivalent.

6.2.1 The Belle $B \to X_s\gamma$ photon energy spectrum

The full details of the $B \to X_s\gamma$ photon energy spectrum measurement at Belle can be found in references[71, 73]. Here the analysis is briefly reviewed.

The analysis used data samples amounting to $140\,\mathrm{fb}^{-1}$ and $15\,\mathrm{fb}^{-1}$ of integrated luminosity taken at (ON) and $60\,\mathrm{MeV}$ below (OFF) the $\Upsilon(4S)$ resonance energy respectively.

The analysis procedure involved reconstructing photon candidates with energy greater than $1.5\,\mathrm{GeV}$ as measured in the $\Upsilon(4S)$ rest frame. Photon candidates were vetoed if they had a high likelihood of originating from π^0 and η decays to two photons. The likelihood, modelled in MC, was calculated as a function of: the combined invariant mass of the photon candidate paired with another photon reconstructed in the event; and the energy and polar angle of the other photon in the laboratory frame.

In general, the background of photons from continuum dominates. It is suppressed through use of event shape variables, which are used as inputs into two Fisher discriminants[52]. The first discriminant is used to distinguish spherically-shaped $B\overline{B}$ events from jet-like continuum events and includes the: Fox-Wolfram moments[49]; thrust; and the angles of the thrust axis with respect to the beam and candidate photon directions. The second discriminant is designed to exploit the topology of $b \to s\gamma$ events by utilising energy flow into three angular regions, $\alpha^* < 30°$, $30° \leq \alpha^* \leq 140°$, $\alpha^* > 140°$, where α^* is the angle to the candidate photon. After cuts the remaining continuum background is removed by subtracting scaled OFF data yields from that of ON data.

Backgrounds from B decays are estimated from $B\overline{B}$ MC and scaled according to studies in data wherever possible and then subtracted from the data. Their contributions include:

- photons from π^0 and η (veto leakage);
- other real photons mainly from ω, η', and J/ψ;
- ECL clusters not due to single photons (mainly electrons interacting with matter, K_L^0 and $\bar{n}$);
- and beam background.

The photon spectra for ON and scaled OFF data samples along with the results of subsequent background subtractions are plotted in figure 6.3(a). The $B \to X_s\gamma$ photon energy spectrum that has been corrected for efficiency is shown in figure 6.3(b). The analysis measured the branching fraction,

$$\mathcal{B}(B \to X_s\gamma) = (3.55 \pm 0.32^{+0.30+0.11}_{-0.31-0.07}) \times 10^{-4}, \tag{6.4}$$

where the errors are statistical, systematic and theoretical, respectively. This result is in agreement with the latest theoretical calculations [74, 75], as well as with previous measurements made by CLEO and Belle [29, 76]. The first two moments for $E^{\gamma}_{\mathrm{cm}} > 1.8\,\mathrm{GeV}$, as obtained from the efficiency corrected spectrum and adjusted for the B boost, energy resolution and binning effects, were measured to be

$$\langle E_\gamma \rangle = 2.292 \pm 0.026 \pm 0.034\,\mathrm{GeV}, \tag{6.5}$$

and

$$\left\langle E_\gamma^2 \right\rangle - \langle E_\gamma \rangle^2 = 0.0305 \pm 0.0074 \pm 0.0063\,\mathrm{GeV}^2, \tag{6.6}$$

where the errors are statistical and systematic.

6.2.2 Fitting the energy spectrum

Information about the shape function, which describes the *Fermi motion* of the b-quark within the B meson, can be gained from the $B \to X_s\gamma$ photon energy spectrum (the relationship is described in section 2.3.1). The information is obtained by fitting MC simulated spectra to the “raw” data spectrum. “Raw” here refers to the spectrum as obtained after the application of the $B \to X_s\gamma$ analysis cuts and from which the background has been subtracted.

Using MC “raw” spectra correctly accounts for efficiency, B boost and energy resolution effects. The MC spectra are derived using the Kagan and Neubert prescription[77](as described in section 2.3.1), which includes the shape function.

The procedure is as follows:

1. Assume a model for the shape function;

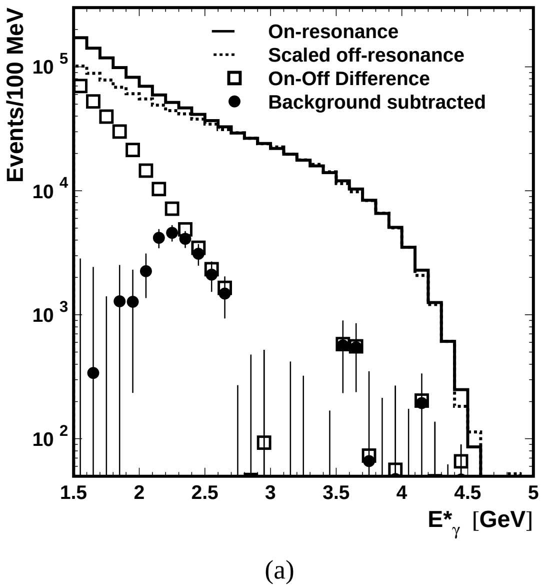

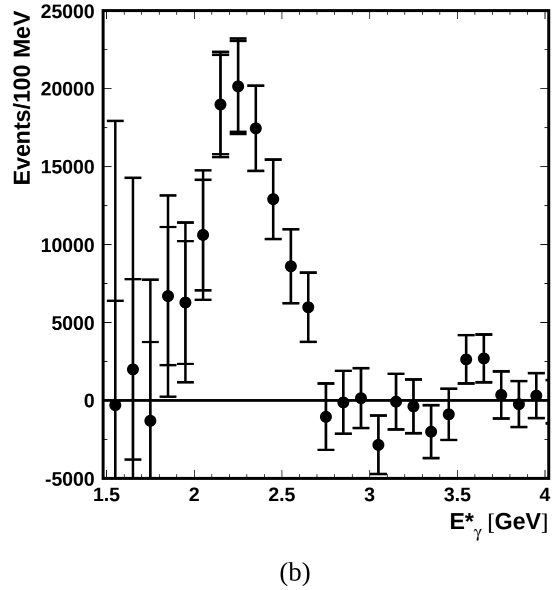

Figure 6.3: (a) Photon energy spectra in the $\Upsilon(4S)$ frame. (b) Efficiency-corrected photon energy spectrum. The two error bars show the statistical and total errors.

2. Simulate the photon energy spectrum based on the Kagan and Neubert prescription for a certain set of the shape function parameters $(\Lambda^{\rm SF}, \lambda_1^{\rm SF})$;
3. Perform a χ^2 fit of the MC simulated spectrum to the "raw" data spectrum where only the normalisation of the simulated spectrum is floated and keep the resultant χ^2 value;
4. Repeat steps 2-3 for different sets of parameters in order to construct a two dimensional grid with each point having a χ^2 value;
5. Find the minimum χ^2 on the grid and all points on the grid that are one unit of χ^2 above the minimum;
6. Calculate $B \to X_u l \nu_l$ spectral fractions for the χ^2 minimum point as well as for select points that have a χ^2 value one unit above the minimum;
7. Repeat steps 1-6 for a different shape function model.

Shape function models

Three shape function forms suggested in the literature are employed; Exponential, Gaussian and Roman[78]. These are described in table 6.3. The shape function variable is the residual light cone momentum k_+. The shape function is parameterised by $\Lambda^{\rm SF}$ and $\lambda_1^{\rm SF}$. These parameters are related to the b quark mass, m_b, and the average momentum squared of the b quark, μ_π^2, via the relations

$$\Lambda^{\rm SF} = M_B - m_b, \tag{6.7}$$

and

$$\lambda_1^{\rm SF} = -\mu_\pi^2, \tag{6.8}$$

where M_B is the mass of the B meson. Example shape function curves are plotted in figure 6.4.

Shape Function	Form
Exponential	$F(k_+; a) = N(1-x)^a e^{(1+a)x}$
Gaussian	$F(k_+; c) = N(1-x)^c e^{-b(1-x)^2}$ where $b = (\Gamma(\frac{1}{2}(c+2))/\Gamma(\frac{1}{2}(c+1)))^2$
Roman	$F(k_+; \rho) = N\frac{\kappa}{\sqrt{\pi}} \exp\big\{ -\frac{1}{4}\big(\frac{1}{\kappa}\frac{\rho}{1-x} - \kappa(1-x)\big)^2\big\}$ where $\kappa = \frac{\rho}{\sqrt{\pi}} e^{\rho/2} K_1(\rho/2)$ (K_1-MacDonald function)
where $x = k_+/\Lambda^{\rm SF}$ $-m_b \leq k_+ \leq \Lambda^{\rm SF}$ and a, c, ρ, N are chosen to satisfy $A_0 = 1$, $A_1 = 0$, $A_2 = -\lambda_1^{\rm SF}/3$, where $A_n = \int k_+^n F(k_+) dk_+$	

Table 6.3: The three models used for the shape function forms.

Monte Carlo simulated photon energy spectrum

It is not feasible to generate signal MC samples with all the variations of shape function form and parameter ranges necessary to simulate a spectrum that would best fit the data. Instead, a large inclusive $B \to X_s\gamma$ MC sample is used in which the M_{X_s} spectrum has been generated according to a Breit-Wigner form. The MC is re-weighted in generated M_{X_s} to agree with spectra as calculated with the Kagan and Neubert prescription (with the given shape function model and set of parameters). The Belle $B \to X_s\gamma$ analysis cuts are applied to the MC and the resultant $B \to X_s\gamma$ photon energy spectrum in the $\Upsilon(4S)$ rest frame is measured.

Fitting the spectrum

A χ^2 fit of the MC simulated photon spectrum to the “raw” data spectrum is performed in the interval $1.5 < E_{\rm cm}^{\gamma}/{\rm GeV} < 2.8$. The normalisation parameter is floated in the fit. The “raw” spectrum is plotted in

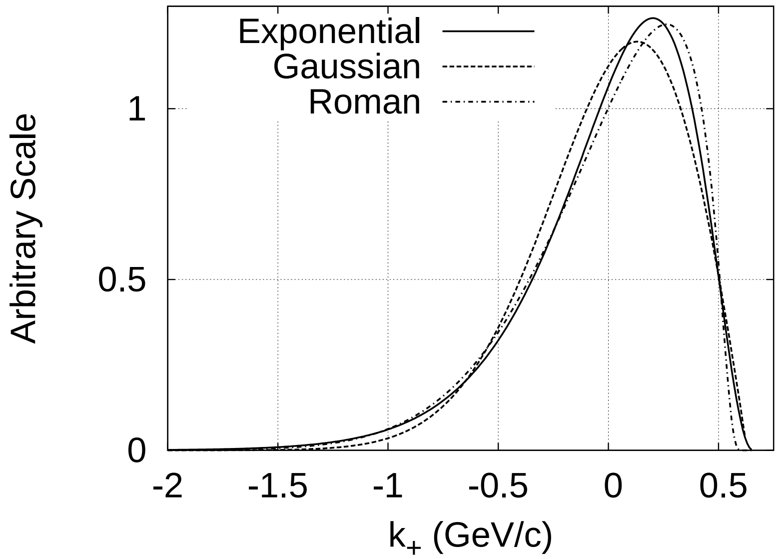

Figure 6.4: Shape function model curves for Exponential $(\Lambda^{\mathrm{SF}}, \lambda_1^{\mathrm{SF}}) = (0.66, -0.40)$, Gaussian $(\Lambda^{\mathrm{SF}}, \lambda_1^{\mathrm{SF}}) = (0.63, -0.33)$, and Roman $(\Lambda^{\mathrm{SF}}, \lambda_1^{\mathrm{SF}}) = (0.66, -0.39)$, where Λ^{SF} and λ_1^{SF} are measured in units of GeV/c^2 and GeV^2/c^2 respectively.

figure 6.5, where the errors include both statistical and systematic uncertainties. The latter are dominated by the estimation of the $B\overline{B}$ background, and are 100% correlated. Therefore the covariance matrix is constructed as

$$V_{ij} = \sigma_{d_i}^{\mathrm{stat}} \sigma_{d_j}^{\mathrm{stat}} \delta_{ij} + \sigma_{d_i}^{\mathrm{sys}} \sigma_{d_j}^{\mathrm{sys}}, \tag{6.9}$$

where $i, j = 1, 2, \ldots, 13$ denote the bin number and σ_d is the error in the data. Then the χ^2 minimised in the fit is given by

$$\chi^2 = \sum_{ij} (d_i - f_i)(V_{ij})^{-1}(d_j - f_j), \tag{6.10}$$

where $(V_{ij})^{-1}$ denotes the ij^{th} element of the inverted covariance matrix.[1]

The best fit and $\Delta\chi^2$ contour

The best fit parameters are associated with the minimum chi-squared case, χ^2_{min}. The 1σ error "ellipse" is defined as the contour which satisfies $\Delta\chi^2 \equiv \chi^2 - \chi^2_{\mathrm{min}} = 1$. The contours are found to be well

[1] In general the covariance matrix can be written as

$$V_{ij} = \sigma_{d_i}^{\mathrm{stat}} \sigma_{d_j}^{\mathrm{stat}} \delta_{ij} + \rho_{ij} \sigma_{d_i}^{\mathrm{sys}} \sigma_{d_j}^{\mathrm{sys}} \tag{6.11}$$

where ρ_{ij} is the correlation coefficient between the errors in bin i and j. When the errors are 100% correlated across bins $\rho_{ij} = 1$, when they are uncorrelated $\rho_{ij} = \delta_{ij}$.

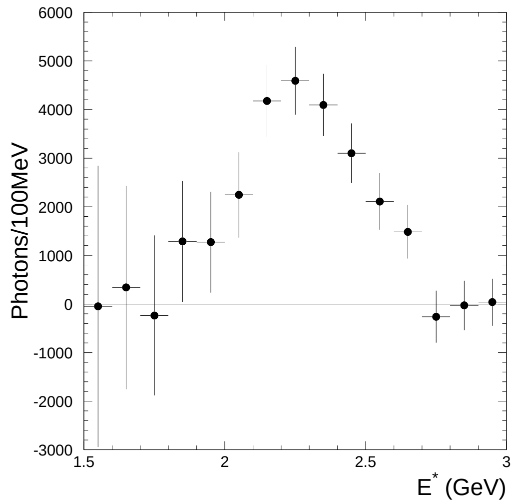

Figure 6.5: "Raw" photon energy spectrum in the $\Upsilon(4S)$ frame. The errors include both statistical and systematic uncertainties.

approximated by the function[79]

$$\Delta\chi^2(\Lambda^{\mathrm{SF}}, \lambda_1^{\mathrm{SF}}) = \left(\frac{\lambda_1^{\mathrm{SF}} + a(\Lambda^{\mathrm{SF}})^2 + b}{c}\right)^2 + \left(\frac{(\Lambda^{\mathrm{SF}})^2 + d}{e}\right)^2. \tag{6.12}$$

The parameters a, b, c, d, and e are determined by fitting the $\Delta\chi^2$ function to the parameter points that lie on the contour.

Calculating spectral fractions

Spectral fractions are evaluated using De Fazio and Neubert[25] calculations of the $B \to X_u l \nu_l$ lepton energy spectrum. The spectral fraction, f_u^x, is defined as

$$f_u^x = \frac{\int_x^{2.6\,\mathrm{GeV}} \frac{d\Gamma}{dE_{\mathrm{cm}}^l} dE_{\mathrm{cm}}^l}{\int_0^{\frac{M_B}{2}} \frac{d\Gamma}{dE_{\mathrm{cm}}^l} dE_{\mathrm{cm}}^l}, \tag{6.13}$$

which is the fraction of $B \to X_u l \nu_l$ events lying between the lower lepton energy cutoff, x, and $2.6\,\mathrm{GeV}$, as measured in the $\Upsilon(4S)$ rest frame.

The spectral fractions are calculated for the parameter values corresponding to the minimum χ^2 point, denoted c, and the points that define the long and short axes of the $\Delta\chi^2 = 1$ fitted contour, denoted e_1, e_2, e_3, and e_4, and depicted in figure 6.6. For a given shape function model

$$f_{u-\mathrm{shape}} = f_u^x(c), \tag{6.14}$$

with the statistical uncertainty given by

$$\Delta f_{u-\text{shape}} = \frac{(f_u^x(e_1) - f_u^x(e_2))}{2} \oplus \frac{(f_u^x(e_3) - f_u^x(e_4))}{2}. \tag{6.15}$$

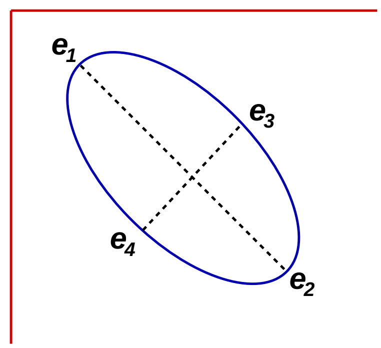

Figure 6.6: The points of interest on the $\Delta\chi^2 = 1$ contour.

Results

The minimum χ^2 fit for each shape function model is displayed in figure 6.7. The contour fits to the points with $\Delta\chi^2 = 1$ are shown in figure 6.8. The minimum χ^2 point (c) and points of interest on the contour (e_1, e_2, e_3, e_4) are given in table 6.4. The best fit parameter values are found to be consistent across all three shape function forms. The spectral fractions for the energy intervals of interest to this analysis are given in table 6.5. Since there is no preference for one shape function over another, the final f_u^x values are calculated as an average over the three models,

$$\bar{f}_u = \sum_{\text{shape}}^{N} \frac{f_{u-\text{shape}}}{N}, \tag{6.16}$$

with the statistical uncertainty likewise averaged,

$$\Delta \bar{f}_u = \sum_{\text{shape}}^{N} \frac{\Delta f_{u-\text{shape}}}{N}, \tag{6.17}$$

where N is the number of shape function models used ($N = 3$). The spread across different shape function models is assigned as a systematic error, and is calculated as the root-mean-square (RMS) of deviations from the central value, given by

$$\text{RMS} = \sqrt{\sum_{\text{shape}}^{N} \frac{(f_{u-\text{shape}} - \bar{f}_u)^2}{N-1}}. \tag{6.18}$$

The resultant f_u^x values and uncertainties are given in table 6.6.

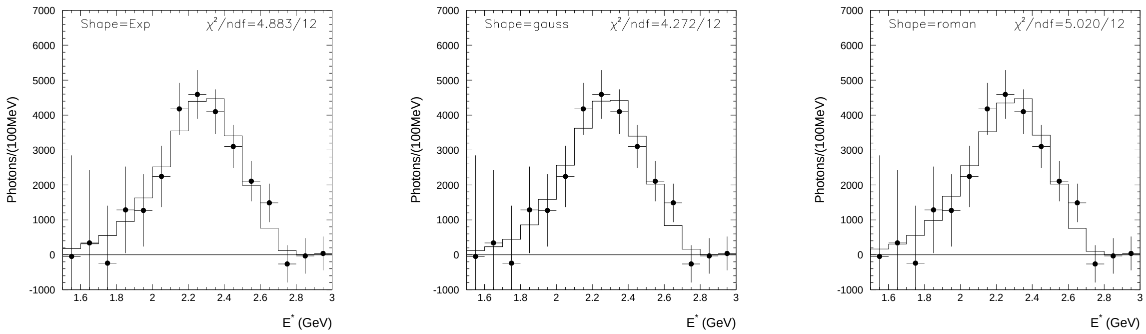

(a) Exponential. (b) Gaussian. (c) Roman.

Figure 6.7: The minimum χ^2 (best) fits of MC simulated spectra to the "raw" data for each shape function model.

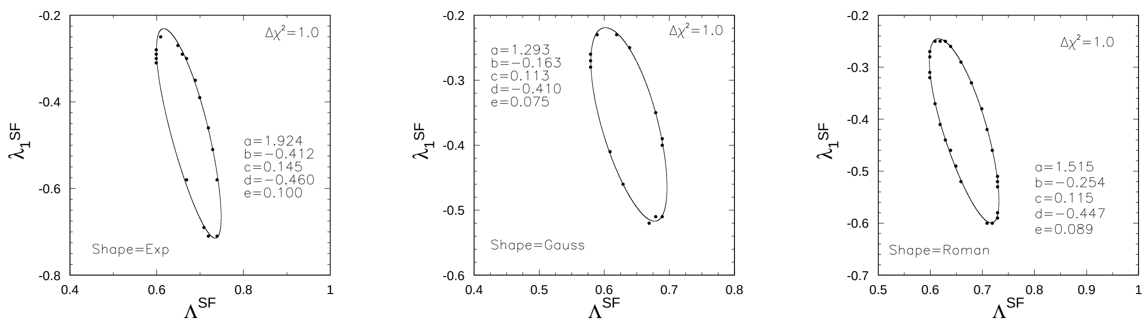

(a) Exponential. (b) Gaussian. (c) Roman.

Figure 6.8: The fitted $\Delta\chi^2 = 1$ contours for each shape function model, where $\Lambda^{\rm SF}$ and $\lambda_1^{\rm SF}$ are measured in units of (GeV/c^2) and (GeV^2/c^2) respectively.

6.2.3 Strong Coupling α_s

The strong coupling constant α_s, is an input into the parton-level calculations for both $b \to s\gamma$ and $b \to ul\nu$ spectra. By default $\alpha_s(\mu)$ is evaluated at the mass scale $\mu = m_b$. It is calculated using the relation

$$\alpha_s(\mu) = \frac{1}{\frac{1}{\alpha_s(M_{Z^0})} + \frac{23}{12\pi}\ln\left(\frac{\mu}{M_{Z^0}}\right)^2}. \tag{6.19}$$

To investigate the systematic effect of the choice $\mu = m_b$, the analysis is redone for $\mu = m_b/2$ and $\mu = 2m_b$, using the exponential shape function form. The $\Lambda^{\rm SF}$ and $\lambda_1^{\rm SF}$ values corresponding to $\chi^2_{\rm min}$ for

Shape	Exponential		Gauss		Roman	
	Λ^{SF} (GeV/c^2)	λ_1^{SF} (GeV^2/c^2)	Λ^{SF} (GeV/c^2)	λ_1^{SF} (GeV^2/c^2)	Λ^{SF} (GeV/c^2)	λ_1^{SF} (GeV^2/c^2)
c	0.659	-0.400	0.629	-0.330	0.659	-0.390
e_1	0.614	-0.231	0.598	-0.220	0.613	-0.246
e_2	0.736	-0.714	0.680	-0.517	0.720	-0.600
e_3	0.719	-0.462	0.681	-0.357	0.707	-0.410
e_4	0.635	-0.483	0.598	-0.380	0.627	-0.434

Table 6.4: The best fit shape function parameter values for the $\chi^2_{\min}$ point, c, and for points defining the long and short axis of the $\Delta\chi^2 = 1$ "ellipse", e_1, e_2, e_3 and e_4.

f_u^x						
Exponential						
Point	$x = 1.9$	$x = 2.0$	$x = 2.1$	$x = 2.2$	$x = 2.3$	$x = 2.4$
c	0.3213	0.2454	0.1730	0.1088	0.0578	0.0239
e_1	0.3377	0.2591	0.1822	0.1126	0.0574	0.0221
e_2	0.2988	0.2276	0.1614	0.1033	0.0570	0.0249
e_3	0.3023	0.2272	0.1572	0.0966	0.0499	0.0200
e_4	0.3283	0.2539	0.1829	0.1188	0.0662	0.0292
Gaussian						
Point	$x = 1.9$	$x = 2.0$	$x = 2.1$	$x = 2.2$	$x = 2.3$	$x = 2.4$
c	0.3293	0.2518	0.1777	0.1122	0.0604	0.0257
e_1	0.3422	0.2631	0.1855	0.1154	0.0599	0.0240
e_2	0.3108	0.2370	0.1682	0.1083	0.0606	0.0274
e_3	0.3124	0.2351	0.1626	0.1001	0.0523	0.0215
e_4	0.3374	0.2613	0.1883	0.1228	0.0692	0.0313
Roman						
Point	$x = 1.9$	$x = 2.0$	$x = 2.1$	$x = 2.2$	$x = 2.3$	$x = 2.4$
c	0.3206	0.2447	0.1728	0.1091	0.0584	0.0242
e_1	0.3374	0.2593	0.1833	0.1146	0.0596	0.0235
e_2	0.3009	0.2288	0.1619	0.1036	0.0572	0.0249
e_3	0.3056	0.2298	0.1590	0.0977	0.0502	0.0198
e_4	0.3296	0.2546	0.1832	0.1192	0.0667	0.0295

Table 6.5: f_u^x for the three shape function models.

x (GeV)	f_u^x
1.9	$0.3237 \pm 0.0218 \pm 0.0043$
2.0	$0.2473 \pm 0.0196 \pm 0.0035$
2.1	$0.1745 \pm 0.0161 \pm 0.0025$
2.2	$0.1100 \pm 0.0120 \pm 0.0018$
2.3	$0.0589 \pm 0.0083 \pm 0.0014$
2.4	$0.0246 \pm 0.0050 \pm 0.0009$

Table 6.6: The spectral fractions calculated as an average over the three shape function forms. The first error is statistical. The second error is the root mean square deviation and is assigned as a systematic uncertainty.

different α_s are given in table 6.7. The greatest variation in f_u observed from either of these changes is taken as the systematic uncertainty. The uncertainties are given in table 6.8.

μ	$\alpha_s(\mu)$	Λ^{SF} (GeV/c^2)	λ_1^{SF} (GeV^2/c^2)
m_b	0.210	0.66	-0.40
$m_b/2$	0.257	0.65	-0.41
$2m_b$	0.177	0.68	-0.43

Table 6.7: The best fit parameters for various α_s using the exponential shape function form.

x (GeV)	Uncertainty $\Delta f_u(\alpha_s)$
1.9	0.0030
2.0	0.0033
2.1	0.0034
2.2	0.0031
2.3	0.0024
2.4	0.0014

Table 6.8: The uncertainty in f_u due to α_s.

6.2.4 Theoretical Uncertainty

The assumption of shape function universality is only valid to leading order in $1/m_b$. CLEO quantified an uncertainty for this assumption by varying the best fit shape parameters, Λ^{SF} and λ_1^{SF} by $\pm 10\%$ based on a recommendation by Neubert. However since then work has been done to better quantify the uncertainty, as alluded to in §2.3.1. In general these uncertainties are known as power corrections, deriving from subleading twist effects that are encoded into subleading shape functions, and weak annihilation effects.

Leibovich, Ligeti and Wise considered the effects of [31]:

- the subleading shape functions, which are suppressed by powers of $\Lambda_{\mathrm{QCD}}/m_b$, but are enhanced by numerical factors. Assuming the functions were positive for all values of k_+, the fractional rates in the endpoint regions were found to decrease by large amounts, for example -15% for $E_0 = 2.2\,\mathrm{GeV}$, where E_0 is the lower energy cutoff (as measured in the rest frame of the B meson). The use of $B \to X_s\gamma$ results, as reported in this thesis, can alleviate this correction by about a third.

- weak annihilation (WA) graphs (the dimension-6 four quark operators in the OPE). These are suppressed by $\Lambda^2_{\mathrm{QCD}}/m_b^2$ but are enhanced by a numerical factor of $16\pi^2$. The terms vanish if factorisation is assumed and the vacuum saturation approximation is evoked. They assume deviations of 10% from that ideal case and find a fractional correction in the partial rate for $E_0 = 2.2\,\mathrm{GeV}$ of $12-17\%$. Moreover, the sign is undetermined.

They conclude that the uncertainty on $|V_{ub}|$ for $E_0 = 2.2\,\mathrm{GeV}$ is above the 10% level, even with the inclusion of information from the $B \to X_s\gamma$ photon energy spectrum. This uncertainty is larger than found by varying the shape parameters by $\pm10\%$.

Bauer, Luke and Mannel[80] also studied the subleading shape function effects. They calculated a correction of 15% to $|V_{ub}|$ for $E_0 = 2.2\,\mathrm{GeV}$. Since in their own evaluation the calculation was "highly model dependent", they estimated the uncertainty in $|V_{ub}|$ to be at the 15% level.

Although pessimistic about the $|V_{ub}|$ extraction at $E_0 \geq 2.2\,\mathrm{GeV}$, both papers point out that if $|V_{ub}|$ could be extracted for a lower energy cutoff of $E_0 \leq 2.0\,\mathrm{GeV}$, then the $|V_{ub}|$ extraction can proceed without recourse to the shape function, and therefore subject to a much reduced theoretical error.

Following these studies, Neubert also performed calculations of subleading effects [81]. Neubert showed that the first moments of the subleading shape functions gave a large negative non-vanishing contribution to f_u, which were found to affect f_u even for E_0 values well below the endpoint. The correction was found to be of order $\Lambda^2_{\mathrm{QCD}}/(m_b\Delta E)$, where $\Delta E = M_B/2 - E_0$. Consequent subleading shape function modelling uncertainties in $|V_{ub}|$ are then treated with respect to this correction and are estimated to be below the 10% level.

All these evaluations are performed in the rest frame of the B meson. Although the B meson boost in the $\Upsilon(4S)$ frame is small it still introduces smearing, and this complicates the use of relations given in the theory papers. Therefore, likely power corrections to f_u have not been implemented but rather are treated as uncertainties. Therefore, in light of the findings discussed above, it was decided, instead to be more conservative with the theoretical uncertainty evaluation, by varying the shape function parameters by $\pm20\%$, such that they bound the corrections. The uncertainty is calculated as

$$\Delta = \frac{f_u^{+20\%\Lambda^{\mathrm{SF}}} - f_u^{-20\%\Lambda^{\mathrm{SF}}}}{2} \oplus \frac{f_u^{+20\%\lambda_1^{\mathrm{SF}}} - f_u^{-20\%\lambda_1^{\mathrm{SF}}}}{2}. \tag{6.20}$$

The resultant uncertainties are given in table 6.9 as well as for comparison, those for $\pm10\%$ and $\pm15\%$

variations. The errors on f_u roughly agree with those estimated by Bauer, Luke and Mannel [80].

Region	P.C. uncertainties		
(GeV)	$\pm10\%$	$\pm15\%$	$\pm20\%$
1.9-2.6	0.0205	0.0307	0.0408
2.0-2.6	0.0210	0.0314	0.0417
2.1-2.6	0.0201	0.0301	0.0399
2.2-2.6	0.0173	0.0259	0.0343
2.3-2.6	0.0126	0.0188	0.0250
2.4-2.6	0.0070	0.0105	0.0140

Table 6.9: An estimate of power correction (P.C.) effects on f_u, as found by varying the best fit shape function parameters by $\pm10\%$, $\pm15\%$ and $\pm20\%$.

6.2.5 Summary

The spectral fractions used to extrapolate the partial to the full branching fractions are summarised in table 6.10. The first error is statistical, the second, a sum in quadrature of the RMS and α_s related uncertainty, is systematic, and the third is a theoretical error. The spectral fractions found by CLEO are given in table 6.11.

CLEO spectral fractions are larger than those presented here. This is due to the difference in the respective Λ^{SF}. For the exponential shape function model, CLEO found, $(\Lambda^{\mathrm{SF}}, \lambda_1^{\mathrm{SF}})_{\mathrm{Exp}} = (0.545, -0.342)$[24]. In general, larger values of Λ^{SF} will give smaller f_u values for the energy spectrum. Independent of the extracted b-quark shape function parameter values, the discrepancy can be traced to the difference in the measured first order moments of the $B \to X_s\gamma$ photon energy spectrum. The CLEO measured moment from $E_\gamma = (2.0 - 2.8)\,\mathrm{GeV}/c$ is $\langle E_\gamma \rangle = 2.346 \pm 0.032 \pm 0.011$ while for Belle, measured from $E_\gamma = (1.8 - 2.8)\,\mathrm{GeV}/c$, it is $\langle E_\gamma \rangle = 2.292 \pm 0.026 \pm 0.034$.

Both CLEO and Belle spectra were obtained for energies as measured in the $\Upsilon(4S)$ rest frame. Belle, aided by a larger sample of both ON and OFF resonance data compared to CLEO, was able to measure significant yields in the energy bins, $(1.8 - 1.9)\,\mathrm{GeV}$ and $(1.9 - 2.0)\,\mathrm{GeV}$. The statistical uncertainty is dominated by the statistics available in the OFF resonance data sample, even though the Belle analysis used fourteen times more ON resonance data, only three times more OFF resonance data was available. The statistical errors are roughly half those of CLEO.

The CLEO systematic uncertainty is typically $2 \sim 3$ times larger, which may be due to the inclusion of an uncertainty due the $B\overline{B}$ background normalisation in their analysis. In the analysis presented here the uncertainty in the $B\overline{B}$ background is included in the error on the points in the raw data spectrum and incorporated into the definition of the χ^2. Therefore it is taken into account in the statistical error. Both analyses include effects of the shape function model differences and α_s variation.

The theoretical uncertainties, as discussed in the previous subsection, are estimated differently in this analysis, and dominate the overall uncertainty.

x (GeV)	f_u^x
1.9	$0.324 \pm 0.022 \pm 0.005 \pm 0.041$
2.0	$0.247 \pm 0.020 \pm 0.005 \pm 0.042$
2.1	$0.175 \pm 0.016 \pm 0.004 \pm 0.040$
2.2	$0.110 \pm 0.012 \pm 0.004 \pm 0.034$
2.3	$0.059 \pm 0.008 \pm 0.003 \pm 0.025$
2.4	$0.025 \pm 0.005 \pm 0.002 \pm 0.014$

Table 6.10: Spectral fractions extracted from the Belle $B \to X_s\gamma$ analysis, f_u. The first error is statistical, the second is systematic, and the third is from theory.

x (GeV)	f_u^x
2.0	$0.278 \pm 0.043 \pm 0.025 \pm 0.017$
2.1	$0.207 \pm 0.037 \pm 0.020 \pm 0.017$
2.2	$0.137 \pm 0.025 \pm 0.016 \pm 0.016$
2.3	$0.078 \pm 0.015 \pm 0.009 \pm 0.013$
2.4	$0.039 \pm 0.008 \pm 0.003 \pm 0.009$

Table 6.11: The CLEO spectral fractions, f_u. The first error is statistical, the second is systematic, and the third is from theory[30].

6.3 Branching fraction measurements

The total inclusive branching fraction is calculated as

$$\mathcal{B}(B \to X_u e\nu_e) = \frac{\Delta\mathcal{B}(B \to X_u e\nu_e)(\Delta p)}{f_u(\Delta p)}(1 + \delta_{\mathrm{RAD}}), \tag{6.21}$$

where δ_{RAD} accounts for the distortion in the yield caused by the electron energy loss through final state radiation. In the procedure for extracting $|V_{ub}|$, in equation 2.31 this effect is not taken into account. The distortion is momentum dependent and is calculated from a comparison of ISGW2 modelled MC spectra generated with and without implementing `PHOTOS`. The `PHOTOS` package was described previously in section 5.4. The δ_{RAD} for the relevant momentum intervals are shown in table 6.12. Based on studies comparing `PHOTOS` results with detailed theoretical calculations[63], a 10% systematic uncertainty is assigned and combined with the statistical error on δ_{RAD}. The resultant branching fractions are calculated and given in table 6.13. For comparison the errors on f_u are kept separate. The branching fractions are consistent with each other.

Momentum interval GeV/c	δ_{RAD}
$1.9 - 2.6$	0.060 ± 0.007
$2.0 - 2.6$	0.066 ± 0.007
$2.1 - 2.6$	0.074 ± 0.008
$2.2 - 2.6$	0.086 ± 0.010
$2.3 - 2.6$	0.096 ± 0.011
$2.4 - 2.6$	0.107 ± 0.014

Table 6.12: Final state radiation loss corrections in overlapping momentum intervals. The error is both statistical and systematic combined. The latter is dominant.

Momentum interval GeV/c	$\mathcal{B}(B \to X_u e \nu_e)$ (10^{-3})
$1.9 - 2.6$	$2.48 \pm 0.61 \pm 0.17 \pm 0.31$
$2.0 - 2.6$	$2.40 \pm 0.50 \pm 0.20 \pm 0.40$
$2.1 - 2.6$	$2.26 \pm 0.35 \pm 0.21 \pm 0.52$
$2.2 - 2.6$	$2.25 \pm 0.30 \pm 0.26 \pm 0.70$
$2.3 - 2.6$	$2.40 \pm 0.25 \pm 0.36 \pm 1.02$
$2.4 - 2.6$	$2.65 \pm 0.41 \pm 0.56 \pm 1.51$

Table 6.13: Full branching fractions for the overlapping momentum regions. The first error is the experimental error (combined statistical and systematic). The second is from f_u (combined statistical and systematic) and the third, also from f_u relates to the assumption of the shape function universality in $b \to s\gamma$ and $b \to ul\nu$ decays (f_u theoretical uncertainty).

6.4 Calculating $|V_{ub}|$

The branching fractions given in table 6.13 are used as inputs into the $|V_{ub}|$ extraction formula [17], which is given by

$$|V_{ub}| = 0.00445 \times \left(1 \pm 0.052|_{m_b} \pm 0.020|_{\lambda_{1,2}}\right) \left(\frac{\mathcal{B}(B \to X_u l\nu)}{0.002}\right)^{\frac{1}{2}} \left(\frac{1.55\ \mathrm{ps}}{\tau_B}\right)^{\frac{1}{2}}, \tag{6.22}$$

where $\tau_B = (1.604 \pm 0.012)\,\mathrm{ps}$ is the B lifetime [17], which is calculated as an average over charged and neutral B mesons. The resultant $|V_{ub}|$ values are shown in table 6.14. The error associated with the calculation is taken as the quadratic sum of the uncertainties in the B lifetime, b quark mass, and non-perturbative parameters $\lambda_{1,2}$. For purposes of comparison, the error associated with the $|V_{ub}|$ calculation is denoted separately, in addition to those already mentioned for the branching fraction. The total error is calculated as a quadratic sum of all the contributing errors. The $|V_{ub}|$ values with total errors are plotted in figure 6.9a. There is a less than 10% variation in the $|V_{ub}|$ values. The relative error from each contribution is plotted in figure 6.9b. The plot shows that for high momentum cutoffs the theoretical uncertainties associated with the subleading shape function effects dominate. As the cutoff is lowered they are reduced and the error becomes dominated by the systematic uncertainty associated with the charmed background estimation. The plot neatly shows that if there were no theoretical uncertainty in f_u then the $|V_{ub}|$ of minimal uncertainty would occur at a lower cutoff of $2.2\,\mathrm{GeV}/c$. If it were halved it would occur for a lower cutoff of $2.1\ \mathrm{GeV}/c$. Owing to the large theory error from f_u, $|V_{ub}|$ values of minimal uncertainty, as based on a quadratic sum, are found in the regions with the lowest momentum cutoffs. The contributing uncertainties are summarised in table 6.15.

The $|V_{ub}|$ of minimal uncertainty is extracted in the momentum interval $2.0 < p_{\mathrm{cm}}/\mathrm{GeV}/c < 2.6$, with an uncertainty of 15%, and as such this is the $|V_{ub}|$ measurement quoted for this analysis:

$$|V_{ub}| = (4.79 \pm 0.50 \pm 0.20 \pm 0.40 \pm 0.26) \times 10^{-3}.$$

The first error is the experimental error (combined statistical and systematic). The second is derived from f_u (combined statistical and systematic) and the third, also from f_u relates to the assumption of the shape function universality in $b \to s\gamma$ and $b \to ul\nu$ decays. The fourth is from the $|V_{ub}|$ extraction formula. The largest uncertainty comes from the $B \to X_c e\nu_e$ background subtraction since the background is very large in this region. The theoretical uncertainty in f_u runs a close second.

6.4.1 Comparison with the CLEO endpoint analysis

The CLEO analysis[14] collected yields of both electrons and muons, utilising integrated luminosity samples of $9.13\,\mathrm{fb}^{-1}$ and $4.35\,\mathrm{fb}^{-1}$ taken at and just below the $\Upsilon(4S)$ resonance energy respectively. The

Momentum interval (GeV/c)	$\lvert V_{ub}\rvert(10^{-3})$	Total error	
$1.9-2.6$	$4.88 \pm 0.60 \pm 0.17 \pm 0.31 \pm 0.26$	±0.74	(15.3%)
$2.0-2.6$	$4.79 \pm 0.50 \pm 0.20 \pm 0.40 \pm 0.26$	±0.72	(15.0%)
$2.1-2.6$	$4.65 \pm 0.36 \pm 0.22 \pm 0.53 \pm 0.25$	±0.72	(15.5%)
$2.2-2.6$	$4.64 \pm 0.31 \pm 0.26 \pm 0.72 \pm 0.25$	±0.87	(18.7%)
$2.3-2.6$	$4.79 \pm 0.25 \pm 0.36 \pm 1.02 \pm 0.26$	±1.14	(23.7%)
$2.4-2.6$	$5.04 \pm 0.39 \pm 0.54 \pm 1.43 \pm 0.27$	±1.60	(31.7%)

Table 6.14: Values of $|V_{ub}|$ calculated for the overlapping momentum intervals. The first error is the experimental error (combined statistical and systematic). The second is derived from f_u (combined statistical and systematic) and the third, also from f_u relates to the assumption of the shape function universality in $b \to s\gamma$ and $b \to ul\nu$ decays. The fourth is from the $|V_{ub}|$ extraction formula.

	Momentum Interval (GeV/c)					
Source of Uncertainty	$1.9-2.6$	$2.0-2.6$	$2.1-2.6$	$2.2-2.6$	$2.3-2.6$	$2.4-2.6$
Statistical	0.13	0.13	0.13	0.15	0.20	0.36
$B \to X_c e\nu_e$ background	0.57	0.46	0.30	0.23	0.06	0.00
Other B background	0.04	0.03	0.03	0.03	0.03	0.03
Efficiency-detector	0.11	0.11	0.11	0.11	0.11	0.12
Efficiency-model	0.06	0.06	0.05	0.05	0.05	0.05
$kl1$ dependence	0.03	0.03	0.02	0.04	0.03	0.08
$N_{B\overline{B}}$	0.03	0.03	0.03	0.03	0.03	0.03
δ_{RAD}	0.02	0.02	0.02	0.02	0.03	0.03
f_u statistical	0.16	0.19	0.21	0.25	0.34	0.51
f_u systematic	0.04	0.05	0.06	0.07	0.11	0.17
f_u theory	0.31	0.40	0.53	0.72	1.02	1.43
$\lvert V_{ub}\rvert : m_b(1S), \lambda_{1,2}, \tau_B$	0.26	0.26	0.25	0.25	0.26	0.27
total	±0.74	±0.72	±0.72	±0.87	±1.14	±1.60

Table 6.15: Uncertainties contributing to $|V_{ub}|$.

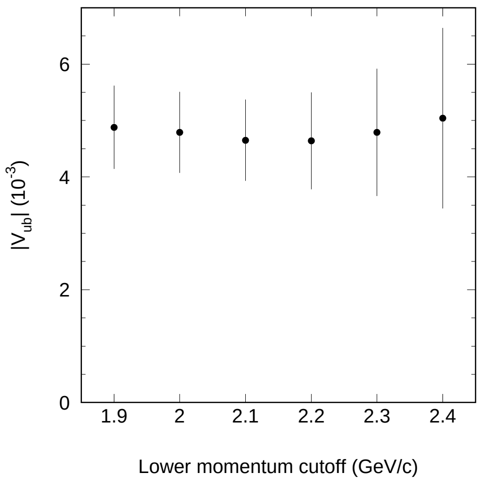

(a)

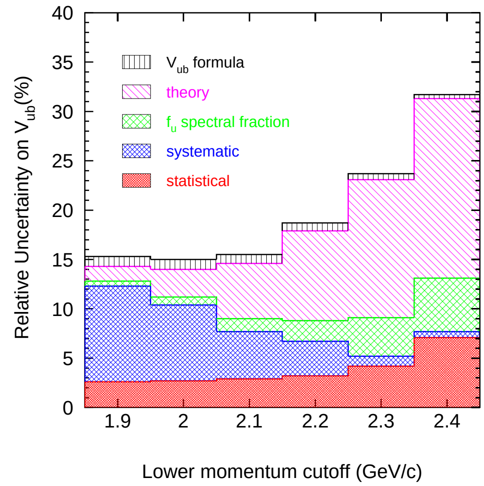

(b)

Figure 6.9: Measured $|V_{ub}|$ as a function of the lower electron momentum cutoff. The error is a quadratic sum of errors given in table 6.14. (b) Relative uncertainties in $|V_{ub}|$, where the histograms show the effect of the accumulation of errors from statistics, systematics, spectral fractions, shape function universality and the $|V_{ub}|$ extraction formula respectively.

proper comparison of the respective endpoint $|V_{ub}|$ measurements can proceed if the full branching fractions for this analysis are calculated with the CLEO determined spectral fractions.

Table 6.16 contains $|V_{ub}|$ values measured with CLEO f_u values, as well as CLEO $|V_{ub}|$ values calculated with the $|V_{ub}|$ extraction formula used in this analysis. Only experimental uncertainties are given since the errors on f_u and the $|V_{ub}|$ calculation are the same. All results agree very well, though there is better agreement for intervals beginning at $2.2\,\mathrm{GeV}/c$ and above. However, the relative uncertainties are much reduced for this analysis compared with CLEO for the wide momentum regions. There are several reasons why this and other differences arise:

- the systematic uncertainties in the wide momentum intervals are dominated by the modelling of the $B \to D^{(*)}e\nu_e$ background. The understanding of the dominant charmed background has improved since the CLEO analysis was conducted.
- The relative rate of $B \to Dl\nu_l$ and $B \to D^*l\nu_l$ is fixed in the estimation of the background for both analysis. However, this measurement uses the 2003 world averages for $\mathcal{B}(B \to D^*l\nu)$ which are more than 20% larger than those for 2002, and moreover have a reduced uncertainty.
- The $\mathcal{F}_{\text{flow}}$ -$kl1$ combination cut not only shows a preference for signal over continuum, but is 25% more efficient for charmless semileptonic B-meson decays than charmed. Therefore this gives a slight improvement over the CLEO analysis by increasing the signal to background ratio.
- The assumed branching fraction for the $B \to X_ul\nu$ in the lower sideband fits (with the exception of

the $1.5 - 2.2\,\mathrm{GeV}/c$ region where none is assumed) is taken to be $(2.27 \pm 0.60) \times 10^{-3}$, as assigned from a Belle $|V_{ub}|$ measurement [66, 67], whereas the CLEO analysis assumed a branching fraction $\simeq (1.90 \pm 0.20) \times 10^{-3}$ based on their earlier published analysis [51]. As reflected in the systematic error evaluation for this assumption, this will affect the resultant signal yield.

Momentum interval	$V_{ub}(10^{-3})$	
(GeV/c)	This measurement	CLEO
$2.0 - 2.6$	4.52 ± 0.47	3.90 ± 0.83
$2.1 - 2.6$	4.27 ± 0.33	3.99 ± 0.47
$2.2 - 2.6$	4.15 ± 0.28	4.12 ± 0.34
$2.3 - 2.6$	4.16 ± 0.22	4.31 ± 0.24
$2.4 - 2.6$	4.00 ± 0.31	4.08 ± 0.28

Table 6.16: Values of $|V_{ub}|$ with CLEO spectral fractions for measurements presented here and for CLEO measurements (as adjusted for a common $|V_{ub}|$ formula).

6.4.2 Comparison with other $|V_{ub}|$ measurements

Other $|V_{ub}|$ measurements are compared with the $|V_{ub}|$ value calculated for the momentum interval, $2.0 < p/\mathrm{GeV}/c < 2.6$. Figure 6.10 shows a plot of that value along with all published inclusive $|V_{ub}|$ measurements as well as the world average of exclusive decays.

Since $|V_{ub}|$ was confirmed to be non zero by both CLEO[82] and ARGUS[83], a number of $|V_{ub}|$ measurements have been made. All four experiments at LEP: ALEPH[84]; L3[85]; DELPHI[86]; and OPAL[87], measured $|V_{ub}|$ from $B \to X_u l\nu$ decays. The B mesons were produced in jets originating from $Z^0 \to b\bar{b}$ events. The LEP Heavy Flavour Group calculated an average of the four measurements[17],

$$|V_{ub}| = (4.09^{+0.36+0.42}_{-0.39-0.47} \pm 0.25 \pm 0.23) \times 10^{-3},$$

where the first error combines statistical with detector systematic uncertainty, the second is the $b \to cl\nu$ background systematic, the third is from the extrapolation from the restricted to the full phase space, and the fourth from the $|V_{ub}|$ calculation. The other measurements in the plot, include that from CLEO, as discussed in the previous section, and measurements from BaBar[88] and Belle[67].

The BaBar analysis was the first to utilise an $\Upsilon(4S)$ resonance event sample where one of the B mesons had been fully reconstructed via hadronic modes. Referred to as fully reconstructed B samples, they allow for a much improved determination of neutrino momentum. This provides improved resolution in M_X reconstruction than is the case for samples lacking this constraint. The efficiency for fully reconstructing a B meson in any given $\Upsilon(4S)$ decay is small, they quote an efficiency of about 0.5% for B^+B^- and 0.3% $B^0\bar{B}^0$. An M_X analysis offers more $B \to X_u l\nu$ phase space and better signal to noise than an endpoint analysis. However the fraction of signal events in M_X within acceptance is similarly sensitive to the *Fermi motion* of the b quark. BaBar measured $|V_{ub}|$ with a cut of $M_X < 1.55\,\mathrm{GeV}/c^2$.

The Belle analysis was the first to explore the so-called theoretically clean region[89] of $|V_{ub}|$ extraction, by combining information on the leptonic invariant mass squared, q^2, and M_X, and imposing $q^2 > 8\,\mathrm{GeV}^2/c^4$ and $M_X < 1.7\,\mathrm{GeV}/c^2$. It is far less sensitive to the b-quark *Fermi motion* effects than either M_X or endpoint analyses, whilst still accessing ample $B \to X_u l \nu_l$ phase space ($\sim 30\%$). Belle employed a novel X_u reconstruction method in which a simulated annealing minimisation technique was used. It effectively fully reconstructed one of the B mesons from the $\Upsilon(4S)$ resonance decay with much better efficiency than the traditional method at the expense of a reduced signal to noise level ($\approx 1 : 5.5$).

$|V_{ub}|$ can be, and is, determined from branching fraction measurements of exclusive processes $B \to \rho l \nu$ and $B \to \pi l \nu$. To calculate $|V_{ub}|$ one needs to know the relevant form factor, which are calculated using a variety of methods: lattice QCD; light cone sum rules; and quark models (ISGW2 for example). Exclusive $|V_{ub}|$ values are not easily compared with inclusive determinations, but are equally important. The world average (WA) value given in the 2004 Particle Data Group review of particle physics[90], is

$$|V_{ub}| = (3.26 \pm 0.19 \pm 0.15 \pm 0.04^{+0.54}_{-0.39}) \times 10^{-3},$$

where the errors derive from statistics, experimental systematics, $\rho l \nu$ form factor uncertainties, and Lattice QCD and Light Cone Sum Rules, respectively. Adding the uncertainties in quadrature gives an upwards relative uncertainty of 18%. The measurement presented here is 1.6σ away from this average, so at first sight, is not in good agreement. But this is the wrong view to take, since exclusive and inclusive determinations belong to distinct theoretical frameworks, namely quenched lattice QCD and OPE regimes of long (HQET) and short (perturbative in α_s) distance physics, respectively, a systematic difference is not unexpected.

In summary the measurement presented here is within uncertainty of all inclusive values given in the plot. Moreover, the overall relative uncertainty is competitive with the latter three measurements, which are state of the art $|V_{ub}|$ measurements, as their treatment of the $B \to X_c l \nu$ background supersedes that of LEP experiments[17].

6.4.3 Implications of the measurement

A measurement such as this, if published, will be incorporated in the world average $|V_{ub}|$ value. The problem of averaging the $|V_{ub}|$ values determined from inclusive rates is very difficult.[2]

Recently, Gibbons advocated the procedure of averaging the inclusive $|V_{ub}|$ measurements that are least susceptible to theoretical uncertainties, and using the measurements in the more theoretically sensitive re-

[2] For some discussion see the $|V_{ub}|$ review article in reference [17]

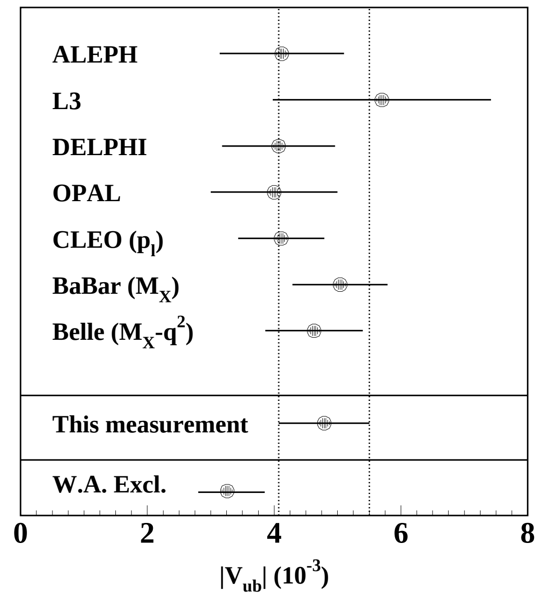

Figure 6.10: Comparison with other $|V_{ub}|$ measurements. (W.A. refers to the World average)

gions to provide bounds for the theoretical errors in the averaged measurement[24]. To date, only Belle had a $q^2 - M_X$ $|V_{ub}|$ measurement[67] that could be included in the average. Available endpoint measurements of $|V_{ub}|$ were used to constrain some of the theoretical uncertainties in the average.[3]

This procedure was pursued in the 2004 Particle Data Group (PDG) review article on $|V_{ub}|$ [90]. The inclusive average quoted is

$$|V_{ub}| = (4.63 \pm 0.28_{\mathrm{STAT}} \pm 0.39_{\mathrm{SYS}} \pm 0.48_{\mathrm{f_{qM}}} \pm 0.32_{\Gamma\mathrm{theory}} \pm 0.27_{\mathrm{WA}} \pm 0.31_{\mathrm{SSF}} \pm 0.11_{\mathrm{LQD}}) \times 10^{-3}, \tag{6.23}$$

where the first error is statistical (STAT), the second is systematic (SYS), the third is associated with the spectral fraction in q^2 and M_X (f_{qM}), the fourth is from the $|V_{ub}|$ extraction formula as dominated by the uncertainty in the b quark mass (Γtheory), and the remaining refer to theoretical uncertainties from weak annihilation graphs (WA), subleading shape function effects (SSF) and the assumptions of local quark hadron duality (LQD). Naively summing in quadrature the uncertainties amount to 19%. Endpoint $|V_{ub}|$ measurements were used to constrain the WA and LQD uncertainties. The measurements reported here will undoubtedly help to reduce the theoretical error or at the very least provide a more thorough understanding of them.

[3]The available measurements include the published CLEO and unpublished BaBar and Belle endpoint analyses. As a rule, unpublished $|V_{ub}|$ measurements, have not been compared with the measurements made in this thesis.

A review of theoretical uncertainties in $|V_{ub}|$ extractions given by Luke at the second CKM workshop [91] identified four main experimental goals in helping resolve outstanding theory issues, two of which this thesis has investigated:

- improved determination of the shape function from the $B \to X_s\gamma$ spectrum;
- $|V_{ub}|$ values as a function of the lepton momentum cut that can bound the size of subleading shape function corrections.

Perhaps superseding all the above, is the $|V_{ub}|$ extraction in the momentum interval, $2.0 < p_{\rm cm}/{\rm GeV}/c < 2.6$. The result was able to be achieved due the improvement in the understanding of the charmed semileptonic B meson decay background. Though incurring large experimental uncertainty due a poor signal-to-background of 1:9, the theoretical uncertainties are significantly reduced as compared to the $|V_{ub}|$ extraction in the interval $2.2 < p_{\rm cm}/{\rm GeV}/c < 2.6$.

Chapter 7

Conclusion

7.1 Improvements and limitations in the analysis

The uncertainty in the charmed semileptonic B meson decay background modelling is the major limitation in reducing the experimental error in the $|V_{ub}|$ measurement. The lesser components, $B \to D^* e\nu_e$ and $B \to De\nu_e$ components, need to better constrained to avoid the mode switching phenomenon. In hindsight it would have been better to constrain the $B \to D^{**} e\nu_e$ component to be greater than the $B \to D^{(*)}\pi e\nu_e$ component, as is the case for measurements presented in the literature to date[17]. In fact, an extreme case of this was implemented in the systematic uncertainty study where no non-resonant component was included in the fit. Although the mode switching effect was taken into account in the systematic uncertainty, it is believed, that such a constraint would make the evaluation of the uncertainty more robust.

The systematic uncertainty in the efficiency estimated for event selection was performed in a limited region of phase space. In future, modes similar to $B \to D(\to K\pi)\rho$ should be investigated to increase the range and therefore confidence in the evaluation.

The theoretical error on f_u has a significant impact on the uncertainty, it was calculated in a crude fashion. If it were reduced by half, then the minimal uncertainty in $|V_{ub}|$ would be found to be 12% instead of 15%. The inclusion of subleading effects in the evaluation of f_u is possible given recent theoretical developments[31, 80, 81]. An application of these methods in one form or another should better quantify the error.

The signal MC samples using the De Fazio and Neubert calculated differential $B \to X_u l\nu$ spectra used values for the parameters m_b and μ_π^2 that were set using CLEO measurements of $B \to X_c l\nu$ and $B \to X_s\gamma$ moments (as described in section 4.2.2). This procedure was carried out on the assumption that moments of the b-quark shape function are directly related to local operators in HQET. A point of issue are recent results reported by Bauer and Manohar [92]. These authors further investigate leading shape function effects in $B \to X_s\gamma$ and $B \to X_u l\nu_l$ decays. They engage soft-collinear effective theory (SCET) to investigate the shape function region in $B \to X_s\gamma$ and $B \to X_u l\nu_l$ decays. Their pertinent findings include:

- due to different anomalous dimensions (deriving from radiative corrections) of the shape function and local operators, moments of the shape function are not directly related to local operators in HQET;

- that the procedure of convolving the perturbative parton-level spectrum with the non-perturbative shape function, as performed by De Fazio and Neubert (DFN) is incorrect because there are large perturbative corrections present in the definition of the shape function.

The latter finding is of prime concern as the approach of DFN underpins the experimental technique, from the generation of $B \to X_u l\nu$ Monte Carlo events and resultant efficiency measurements thru to the evaluation of the spectral fractions f_u, which also relies on Kagan and Neubert calculations of $B \to X_s\gamma$, whose approach of migrating from the parton-to-hadron level is the same as DFN. Unfortunately the authors do not quantify the source of the discrepancy between their results and the hitherto accepted practice of DFN. Shortly following the appearance of the Bauer and Manohar results, some overlapping work, which also uses SCET, was reported by Bosch, Lange, Neubert and Paz [93] whereby they disagree with Bauer and Manohar on the conclusion that moments of the shape function cannot be related to HQET parameters. Quite significant, perhaps, are the new expressions they derive for $B \to X_u l\nu_l$ decay distributions, one of which predicts a spectral fraction for $E_l > 2.2\,\mathrm{GeV}$, as measured in the rest frame of the B meson, of 22%. Even adjusting for smearing due to the B meson motion in the $\Upsilon(4S)$ rest frame, this estimate far exceeds that calculated for this and the CLEO analysis, which are 11% and 14% respectively. Since these results are very recent, they couldn't be satisfactorily incorporated into the analysis as presented in this thesis. To date no $|V_{ub}|$ analysis has incorporated these effects. The above discussion is in part included to give the reader references to the new and exciting work in the theory of inclusive semileptonic B meson decays in it's application to the determination of $|V_{ub}|$.

7.2 Outlook

The future of inclusive $|V_{ub}|$ measurements is promising owing to the ever-growing sample of $\Upsilon(4S)$ resonance decay events currently being accumulated by the Belle and BaBar experiments.

Improved measurements of charmed semileptonic B meson decays are needed to reduce uncertainties associated with its modelling, in particular the $B \to D^* l\nu_l$ form factor slope ρ^2. Currently this number is dominated by the uncertainty in the associated form factor ratios, R_1 and R_2[17, 94]. To date only the CLEO collaboration has measured these parameters. Improved measurements will reduce the error in the $|V_{ub}|$ measurements presented here.

If this analysis is repeated with larger ON and OFF data samples (at Belle there is currently 10 and 3 times more ON and OFF data available), the statistical error would be reduced, but the overall error on $|V_{ub}|$ would decrease marginally. However, for a study of the partial rates or the spectrum of $B \to X_u e \nu_e$, increased OFF data statistics would be of benefit to the high momentum bins.

The measurement of the $B \to X_u l \nu$ momentum spectrum presented here is perhaps precise enough for an extraction of b-quark shape function parameters from the spectrum itself, if performed, the f_u theoretical error would be reduced.

The ever increasing size of fully reconstructed B decay samples available for analyses at Belle and BaBar will have a significant impact. These samples allow implementation of methods that require information of the neutrino. Two such methods proposed, by Bauer et al[89] and Bosch et al[95], predict that theoretical uncertainties on $|V_{ub}|$ at the 5-10% level can be achieved.

There is no reason why $|V_{ub}|$ extractions from the lepton momentum spectrum could not be performed in a fully reconstructed B decay sample as well. Moreover, it is beneficial because:

- the momentum could be measured in the rest frame of the B meson through use of the four-momentum of the associated fully reconstructed B meson. This in combination with a similar measurement of the $B \to X_s \gamma$ photon energy spectrum, though less feasible than $B \to X_u l \nu$ because it is rarer by an order of magnitude, would remove the need for an intermediate shape function in the f_u calculation.

- The measurements could be performed separately for charged and neutral B mesons thus allowing a test of weak annihilation effects[31, 91];

- Uncertainties in the efficiency related to the modelling of $B \to X_u l \nu$ would be diminished because the continuum background would be significantly reduced, thus avoiding the need to bias the q^2 acceptance through harsh continuum suppression cuts.

7.3 Conclusion

Inclusive charmless semileptonic B meson decays were investigated using a $27.8\,\mathrm{fb}^{-1}$ and $8.8\,\mathrm{fb}^{-1}$ dataset collected by the Belle detector at, and just below, the $\Upsilon(4S)$ resonance respectively.

Partial branching ratios of $B \to X_u e \nu_e$ are measured as a function of the electron momentum. These branching ratios are measured to be:

$$\begin{aligned}
\mathcal{B}(B \to X_u e \nu_e)(1.9 < p_{\mathrm{cm}}/\mathrm{GeV}/c < 2.6) &= (7.59 \pm 0.39 \pm 1.82) \times 10^{-3}; \\
\mathcal{B}(B \to X_u e \nu_e)(2.0 < p_{\mathrm{cm}}/\mathrm{GeV}/c < 2.6) &= (5.56 \pm 0.30 \pm 1.11) \times 10^{-3}; \\
\mathcal{B}(B \to X_u e \nu_e)(2.1 < p_{\mathrm{cm}}/\mathrm{GeV}/c < 2.6) &= (3.66 \pm 0.21 \pm 0.52) \times 10^{-3}; \\
\mathcal{B}(B \to X_u e \nu_e)(2.2 < p_{\mathrm{cm}}/\mathrm{GeV}/c < 2.6) &= (2.28 \pm 0.15 \pm 0.26) \times 10^{-3}; \\
\mathcal{B}(B \to X_u e \nu_e)(2.3 < p_{\mathrm{cm}}/\mathrm{GeV}/c < 2.6) &= (1.29 \pm 0.11 \pm 0.08) \times 10^{-3}; \\
\mathcal{B}(B \to X_u e \nu_e)(2.4 < p_{\mathrm{cm}}/\mathrm{GeV}/c < 2.6) &= (0.59 \pm 0.08 \pm 0.03) \times 10^{-3},
\end{aligned} \tag{7.1}$$

where the first error is statistical and the second error is systematic.

The parameters of the b-quark shape function, which describes the *Fermi motion* of the b-quark within the B meson, were extracted from fits to the Belle measured $B \to X_s \gamma$ photon energy spectrum assuming three different models for the shape function. The results for each model were found to be consistent with each other.

The b-quark shape function parameters were used to calculate spectral fractions for the lepton momentum spectrum. The spectral fractions were calculated to be:

$$\begin{aligned}
f_u(1.9 < p_{\mathrm{cm}}/\mathrm{GeV}/c < 2.6) &= 0.324 \pm 0.022 \pm 0.005 \pm 0.041; \\
f_u(2.0 < p_{\mathrm{cm}}/\mathrm{GeV}/c < 2.6) &= 0.247 \pm 0.020 \pm 0.005 \pm 0.042; \\
f_u(2.1 < p_{\mathrm{cm}}/\mathrm{GeV}/c < 2.6) &= 0.175 \pm 0.016 \pm 0.004 \pm 0.040; \\
f_u(2.2 < p_{\mathrm{cm}}/\mathrm{GeV}/c < 2.6) &= 0.110 \pm 0.012 \pm 0.004 \pm 0.034; \\
f_u(2.3 < p_{\mathrm{cm}}/\mathrm{GeV}/c < 2.6) &= 0.059 \pm 0.008 \pm 0.003 \pm 0.025; \\
f_u(2.4 < p_{\mathrm{cm}}/\mathrm{GeV}/c < 2.6) &= 0.025 \pm 0.005 \pm 0.002 \pm 0.014,
\end{aligned} \tag{7.2}$$

where the first error is statistical, the second systematic, and the third is from theory. These in turn were used to extrapolate from partial to full branching ratio measurements. The full branching ratios were used to calculate the CKM matrix element $|V_{ub}|$. The $|V_{ub}|$ values were calculated to be:

$$\begin{aligned}
|V_{ub}|(1.9 < p_{\rm cm}/{\rm GeV}/c < 2.6) &= (4.88 \pm 0.60 \pm 0.17 \pm 0.31 \pm 0.26) \times 10^{-3}; \\
|V_{ub}|(2.0 < p_{\rm cm}/{\rm GeV}/c < 2.6) &= (4.79 \pm 0.50 \pm 0.20 \pm 0.40 \pm 0.26) \times 10^{-3}; \\
|V_{ub}|(2.1 < p_{\rm cm}/{\rm GeV}/c < 2.6) &= (4.65 \pm 0.36 \pm 0.22 \pm 0.53 \pm 0.25) \times 10^{-3}; \\
|V_{ub}|(2.2 < p_{\rm cm}/{\rm GeV}/c < 2.6) &= (4.64 \pm 0.31 \pm 0.26 \pm 0.72 \pm 0.25) \times 10^{-3}; \\
|V_{ub}|(2.3 < p_{\rm cm}/{\rm GeV}/c < 2.6) &= (4.79 \pm 0.25 \pm 0.36 \pm 1.02 \pm 0.26) \times 10^{-3}; \\
|V_{ub}|(2.4 < p_{\rm cm}/{\rm GeV}/c < 2.6) &= (5.04 \pm 0.38 \pm 0.54 \pm 1.43 \pm 0.27) \times 10^{-3},
\end{aligned} \tag{7.3}$$

where the first error is experimental, the second is from f_u, the third is from the theoretical error in f_u, and the fourth derives from the $|V_{ub}|$ extraction formula.

The best $|V_{ub}|$ value, based on the overall fractional uncertainty, was extracted for the momentum interval, $2.0 < p_{\rm cm}/{\rm GeV}/c < 2.6$,

$$|V_{ub}| = (4.79 \pm 0.72) \times 10^{-3}. \tag{7.4}$$

The uncertainty in the value is 15%. The measurement is in good agreement with inclusively measured values of $|V_{ub}|$ [14, 67, 88].

The measurements presented here improve the determination of side-length R_b of the *Unitarity Triangle* and therefore provide a better understanding of the KM mechanism for CP violation.

Bibliography

[1] T.D. Lee and C.N. Yang. Question of parity conservation in weak interactions. *Physical Review*, 104:254, 1956.

[2] C.S. Wu, E. Ambler, R.W. Hayward, D.D. Hoppes, and R.P. Hudson. Experimental test of parity conservation in beta decay. *Physical Review*, 105:1413, 1957.

[3] R.L. Garwin, L.M. Lederman, and M. Weinrich. Observations of the failure of conservation of parity and charge conjugation in meson decays: the magnetic moment of the free muon. *Physical Review*, 105:1415, 1957.

[4] J.L. Friedman and V.L. Telegdi. Nuclear emulsion evidence for parity nonconservation in the decay chain $\pi^+ \rightarrow \mu^+ \rightarrow e^+$. *Physical Review*, 106:1290, 1957.

[5] J. H. Christenson, J. W. Cronin, V. L. Fitch, and R. Turlay. Evidence for the 2 pi decay of the k(2)0 meson. *Phys. Rev. Lett.*, 13:138–140, 1964.

[6] A. D. Sakharov. Violation of *CP* invariance, C asymmetry, and baryon asymmetry of the universe. *Pisma Zh. Eksp. Teor. Fiz.*, 5:32–35, 1967.

[7] N. Cabibbo. Unitary symmetry and leptonic decays. *Phys. Rev. Lett.*, 10:531–532, 1963.

[8] S. L. Glashow, J. Iliopoulos, and L. Maiani. Weak interactions with lepton - hadron symmetry. *Phys. Rev.*, D2:1285–1292, 1970.

[9] M. Kobayashi and T. Maskawa. CP violation in the renormalizable theory of weak interaction. *Prog. Theor. Phys.*, 49:652–657, 1973.

[10] Ashton B. Carter and A. I. Sanda. CP violation in cascade decays of B mesons. *Phys. Rev. Lett.*, 45:952, 1980.

[11] Ikaros I. Y. Bigi and A. I. Sanda. Notes on the observability of CP violations in B decays. *Nucl. Phys.*, B193:85, 1981.

[12] K. Abe et al. Observation of large CP violation in the neutral B meson system. *Phys. Rev. Lett.*, 87:091802, 2001, hep-ex/0107061.

[13] B. Aubert et al. Observation of CP violation in the B^0 meson system. *Phys. Rev. Lett.*, 87:091801, 2001, hep-ex/0107013.

[14] A. Bornheim et al. Improved measurement of $|V_{ub}|$ with inclusive semileptonic B decays. *Phys. Rev. Lett.*, 88:231803, 2002, hep-ex/0202019.

[15] Lincoln Wolfenstein. Parametrization of the Kobayashi-Maskawa matrix. *Phys. Rev. Lett.*, 51:1945, 1983.

[16] M. Battaglia et al. The CKM matrix and the unitarity triangle. 2003, hep-ph/0304132.

[17] K. Hagiwara et al. Review of particle physics. *Phys. Rev.*, D66:010001, 2002.

[18] Aneesh V. Manohar and Mark B. Wise. *Heavy Quark Physics*. Number 10 in Cambridge Monographs on Particle Physics, Nuclear Physics and Cosmology. Cambridge University Press, 2000.

[19] Ikaros I. Y. Bigi, Mikhail A. Shifman, and N. Uraltsev. Aspects of heavy quark theory. *Ann. Rev. Nucl. Part. Sci.*, 47:591–661, 1997, hep-ph/9703290.

[20] Andre H. Hoang, Zoltan Ligeti, and Aneesh V. Manohar. B decay and the Upsilon mass. *Phys. Rev. Lett.*, 82:277–280, 1999, hep-ph/9809423.

[21] Ikaros I. Y. Bigi. Memo on extracting $|V_{cb}|$ and $|V_{ub}/V_{cb}|$ from semileptonic B decays. 1999, hep-ph/9907270.

[22] Zoltan Ligeti. $|V_{cb}|$ and $|V_{ub}|$ from B decays: Recent progress and limitations. 1999, hep-ph/9908432.

[23] Ikaros I. Y. Bigi and Nikolai Uraltsev. A vademecum on quark hadron duality. *Int. J. Mod. Phys.*, A16:5201–5248, 2001, hep-ph/0106346.

[24] Lawrence Gibbons. The status of $|V_{ub}|$. 2004, hep-ex/0402009.

[25] Fulvia De Fazio and Matthias Neubert. $B \to X_u l \nu_l$ decay distributions to order alpha(s). *JHEP*, 06:017, 1999, hep-ph/9905351.

[26] Thomas Mannel and Matthias Neubert. Resummation of Nonperturbative Corrections to the Lepton Spectrum in Inclusive $B \to X l \bar{\nu}$ Decays. *Phys. Rev. D*, 50:2037–2047, 1994, hep-ph/9402288.

[27] Matthias Neubert. Analysis of the photon spectrum in inclusive $B \to X_s \gamma$ decays. *Phys. Rev.*, D49:4623–4633, 1994, hep-ph/9312311.

[28] Ikaros I. Y. Bigi, Mikhail A. Shifman, N. G. Uraltsev, and A. I. Vainshtein. On the motion of heavy quarks inside hadrons: Universal distributions and inclusive decays. *Int. J. Mod. Phys.*, A9:2467–2504, 1994, hep-ph/9312359.

[29] S. Chen et al. Branching fraction and photon energy spectrum for $b \to s\gamma$. *Phys. Rev. Lett.*, 87:251807, 2001, hep-ex/0108032.

[30] S. E. Anderson. *An Improved Measurement of the Inclusive Rate for Charmless Semileptonic Decays of B mesons*. PhD thesis, The University of Minnesota, USA, 2002.

[31] Adam K. Leibovich, Zoltan Ligeti, and Mark B. Wise. Enhanced subleading structure functions in semileptonic B decay. *Phys. Lett.*, B539:242–248, 2002, hep-ph/0205148.

[32] KEKB B–factory design report. Technical Report 95-7, KEK, 1995.

[33] The Belle detector. *Nucl. Instrum. Meth.*, A479:117–232, 2002.

[34] Hiroaki Aihara. The Belle silicon vertex detector. *Nuclear Instruments and Methods in Physics Research Section A*, 466:268–274, 2001, hep-ex/0011028.

[35] H. Hirano et al. A high resolution cylindrical drift chamber for the KEKB B–Factory. *Nucl. Instrum. Meth.*, A455:294–304, 2000.

[36] T. Iijima et al. Aerogel Cherenkov counter for the Belle detector. *Nucl. Instrum. Meth.*, A453:321–325, 2000.

[37] T. Sumiyoshi et al. Silica aerogel Cherenkov counter for the KEKB B–Factory experiment. *Nucl. Instrum. Meth.*, A433:385–391, 1999.

[38] H. Kichimi et al. The Belle TOF system. *Nucl. Instrum. Meth.*, A453:315–320, 2000.

[39] A. Abashian et al. The K(L)/mu detector subsystem for the Belle experiment atthe KEK B factory. *Nucl. Instrum. Meth.*, A449:112–124, 2000.

[40] R. Itoh. *QQ quick reference for Belle*. `http://belle.kek.jp/~software/qq/html/belle_qq.html`.

[41] Torbjorn Sjostrand. PYTHIA 5.7 and JETSET 7.4: Physics and manual. 1995, hep-ph/9508391.

[42] Bo Andersson, G. Gustafson, G. Ingelman, and T. Sjostrand. PARTON FRAGMENTATION AND STRING DYNAMICS. *Phys. Rept.*, 97:31, 1983.

[43] D. J. Lange. The EvtGen particle decay simulation package. *Nucl. Instrum. Meth.*, A462:152–155, 2001.

[44] R. Brun, R. Hagelberg, M. Hansroul, and J. C. Lassalle. GEANT: SIMULATION PROGRAM FOR PARTICLE PHYSICS EXPERIMENTS. USER GUIDE AND REFERENCE MANUAL. CERN-DD-78-2-REV.

[45] Daryl Scora and Nathan Isgur. Semileptonic meson decays in the quark model: An update. *Phys. Rev.*, D52:2783–2812, 1995, hep-ph/9503486.

[46] D. Cronin-Hennessy et al. Hadronic mass moments in inclusive semileptonic B meson decays. *Phys. Rev. Lett.*, 87:251808, 2001, hep-ex/0108033.

[47] V. Zhilich, A. Bondar, A. Kuzmin, H. Sagawa, and B. Shwartz. Offline luminosity measurements from the Belle detector. Belle Note 453, 2001.

[48] Brendan Casey. *Search for CP violation in charmless hadronic B meson decays*. PhD thesis, University of Hawaii, 2001. http://www.phys.hawaii.edu/ casey/thesis/.

[49] G. Fox and S. Wolfram. Observables for the Analysis of Event Shapes in e^+ e^- Annihilation and Other Processess. *Physical Review Letters*, 41:1581, 1978.

[50] Tracking Group. Charged Particle Tracking in Belle. Belle Note 327, 2000.

[51] J. Bartelt et al. Measurement of charmless semileptonic decays of B mesons. *Phys. Rev. Lett.*, 71:4111–4115, 1993.

[52] R. A. Fisher. The use of multiple measurements in taxonomic problems. *Annals Eugen.*, 7:179–188, 1936.

[53] KID Group, H. Hamasaki, T. Iijima, et al. Kaon Identification in Belle. Belle Note 321, 2000.

[54] E. Nakano. Belle PID. *Nucl. Instrum. Meth.*, A494:402–408, 2002.

[55] G. Majumder. Uncertainty of track finding efficiency with embedded tracks. Belle Note 641, 2003.

[56] E. Nakano. See `http://belle.kek.jp/group/pid_joint/slides-030717/nakanoe-030717.ps.gz`.

[57] K. Hanagaki, H. Kakuno, H. Ikeda, T. Iijima, and T. Tsukamoto. Electron identification in Belle. *Nucl. Instrum. Meth.*, A485:490–503, 2002, hep-ex/0108044.

[58] J. Dragic et al. Evidence of $B^0 \to \rho^0\pi^0$. 2004, hep-ex/0405068.

[59] Eric M. Heenan. *An investigation of doubly charmed B meson decays with the Belle detector*. PhD thesis, University of Melbourne, 2002.

[60] J. L. Goity and W. Roberts. Soft pion emission in semileptonic B meson decays. *Phys. Rev.*, D51:3459–3477, 1995, hep-ph/9406236.

[61] T. Browder and S. K. Swain. Beam-energy calibration. Belle Note 567, 2002.

[62] Elisabetta Barberio and Zbigniew Was. PHOTOS: A Universal Monte Carlo for QED radiative corrections. Version 2.0. *Comput. Phys. Commun.*, 79:291–308, 1994.

[63] E. Richter-Was. QED bremsstrahlung in semileptonic B and leptonic tau decays. *Phys. Lett.*, B303:163–169, 1993.

[64] Irinel Caprini, Laurent Lellouch, and Matthias Neubert. Dispersive bounds on the shape of $\overline{B} \to D^{(*)} l \bar{\nu}_l$ form factors. *Nucl. Phys.*, B530:153–181, 1998, hep-ph/9712417.

[65] J. E. Duboscq et al. Measurement of the form-factors for $\overline{B^0} \to D^{*+} l^- \bar{\nu}$. *Phys. Rev. Lett.*, 76:3898–3902, 1996.

[66] H. Kakuno. Measurement of $\mathcal{B}(B \to X_u l \nu)$ and $|V_{ub}|$ through M_X and q^2 reconstructions with a simulated annealing technique. Belle Note 615, 2003.

[67] H. Kakuno et al. Measurement of $|V_{ub}|$ using inclusive $B \to X_u l \nu$ decays with a novel X_u reconstruction method. *Phys. Rev. Lett.*, 92:101801, 2004, hep-ex/0311048.

[68] R. Brun and D. Lienart. HBOOK USER GUIDE: CERN COMPUTER CENTER PROGRAM LIBRARY LONG WRITEUP: VERSION 4. CERN-Y250.

[69] Roger J. Barlow and Christine Beeston. Fitting using finite Monte Carlo samples. *Comput. Phys. Commun.*, 77:219–228, 1993.

[70] F. James. MINUIT USER GUIDE: CERN COMPUTER CENTER PROGRAM LIBRARY LONG WRITEUP: VERSION 4. CERN-D506.

[71] P. Koppenburg et al. An inclusive measurement of the photon energy spectrum in $b \to s\gamma$ decays. 2004, hep-ex/0403004.

[72] A. Limosani and T. Nozaki. Extraction of the b-quark shape function parameters using the Belle $B \to X_s \gamma$ photon energy spectrum. 2004, hep-ex/0407052.

[73] P. Koppenburg. An inclusive measurement of the photon energy spectrum in $b \to s\gamma$ decays. Belle Note 669, 2004.

[74] Tobias Hurth, Enrico Lunghi, and Werner Porod. Untagged $B \to X_{s,d} \gamma$ CP asymmetry as a probe for new physics. 2003, hep-ph/0312260.

[75] Paolo Gambino and Mikolaj Misiak. Quark mass effects in $\overline{B} \to X_s \gamma$. *Nucl. Phys.*, B611:338–366, 2001, hep-ph/0104034.

[76] K. Abe et al. A measurement of the branching fraction for the inclusive $B \to X_s\gamma$ decays with Belle. *Phys. Lett.*, B511:151–158, 2001, hep-ex/0103042.

[77] Alexander L. Kagan and Matthias Neubert. QCD anatomy of $B \to X_s\gamma$ decays. *Eur. Phys. J.*, C7:5–27, 1999, hep-ph/9805303.

[78] Ikaros I. Y. Bigi, Mikhail A. Shifman, N. Uraltsev, and Arkady I. Vainshtein. Heavy quark distribution function in QCD and the AC**2M**2 model. *Phys. Lett.*, B328:431–440, 1994, hep-ph/9402225.

[79] R. Faccini (BaBar collaboration). HFAG-Semileptonic meeting minutes.

[80] Christian W. Bauer, Michael Luke, and Thomas Mannel. Subleading shape functions in $B \to X_u l\bar{\nu}$ and the determination of $|V_{ub}|$. *Phys. Lett.*, B543:261–268, 2002, hep-ph/0205150.

[81] Matthias Neubert. Subleading shape functions and the determination of $|V_{ub}|$. *Phys. Lett.*, B543:269–275, 2002, hep-ph/0207002.

[82] R. Fulton et al. OBSERVATION OF B MESON SEMILEPTONIC DECAYS TO NONCHARMED FINAL STATES. *Phys. Rev. Lett.*, 64:16–20, 1990.

[83] H. Albrecht et al. Study of inclusive semileptonic B meson decays. *Phys. Lett.*, B249:359–365, 1990.

[84] R. Barate et al. Determination of $|V_{ub}|$ from the measurement of the inclusive charmless semileptonic branching ratio of b hadrons. *Eur. Phys. J.*, C6:555–574, 1999.

[85] M. Acciarri et al. Measurement of the inclusive charmless semileptonic branching fraction of beauty hadrons and a determination of $|V_{ub}|$ at LEP. *Phys. Lett.*, B436:174–186, 1998.

[86] P. Abreu et al. Determination of $|V_{ub}|/|V_{cb}|$ with DELPHI at LEP. *Phys. Lett.*, B478:14–30, 2000, hep-ex/0105054.

[87] G. Abbiendi et al. Measurement of $|V_{ub}|$ using b hadron semileptonic decay. *Eur. Phys. J.*, C21:399–410, 2001, hep-ex/0107016.

[88] B. Aubert et al. Measurement of the inclusive charmless semileptonic branching ratio of B mesons and determination of $|V_{ub}|$. *Phys. Rev. Lett.*, 92:071802, 2004, hep-ex/0307062.

[89] Christian W. Bauer, Zoltan Ligeti, and Michael E. Luke. Precision determination of $|V_{ub}|$ from inclusive decays. *Phys. Rev.*, D64:113004, 2001, hep-ph/0107074.

[90] S. Eidelman et al. Review of particle physics. *Phys. Lett.*, B592:1, 2004.

[91] Michael Luke. Applications of the heavy quark expansion: $|V_{ub}|$ and spectral moments. *ECONF*, C0304052:WG107, 2003, hep-ph/0307378.

[92] Christian W. Bauer and Aneesh V. Manohar. Shape function effects in $B \to X_s\gamma$ and $B \to X_u l\nu$ decays. 2003, hep-ph/0312109.

[93] S. W. Bosch, B. O. Lange, M. Neubert, and G. Paz. Factorization and shape-function effects in inclusive b- meson decays. *Nucl. Phys.*, B699:335–386, 2004, hep-ph/0402094.

[94] N. E. Adam et al. Determination of the $\overline{B^0} \to D^* l\bar{\nu}$ width and $|V_{cb}|$. ((B)). *Phys. Rev.*, D67:032001, 2003, hep-ex/0210040.

[95] Stefan W. Bosch, Bjorn O. Lange, Matthias Neubert, and Gil Paz. Proposal for a precision measurement of $|V_{ub}|$. 2004, hep-ph/0403223.

Appendix A

Charmed Semileptonic B decays in `QQ98`

Charmed semileptonic B meson decays in QQ98 are simulated with various models. Table A.1 lists the models implemented in the `QQ98` generator for charmed semileptonic B-meson decays.

Channel X_c	Model
D^*	HQET linear form factor model $\rho^2 = 0.92$ $R_1 = 1.24$ $R_2 = 0.72$
D	ISGW2
D_0^*	ISGW2
D_1'	ISGW2
D_1	ISGW2
D_2^*	ISGW2
$D_2(^1S_0)$	ISGW2
$D_2(^3S_1)$	ISGW2
$D^+\pi^0$	Goity & Roberts
$D^0\pi^+$	Goity & Roberts
$D^{*+}\pi^0$	Goity & Roberts
$D^{*0}\pi^+$	Goity & Roberts

Table A.1: `QQ98` description of charmed semileptonic B meson decay (ISGW2 [45],Goity & Roberts [60]).

Appendix B

World averages

Branching ratio %		
Mode	2002 [17]	2003[†]
$B^0 \to X l^+ \nu$	10.5 ± 0.8	10.5 ± 0.8
$B^0 \to D^- l^+ \nu$	2.11 ± 0.17	2.14 ± 0.20
$B^0 \to D^*(2010)^- l^+ \nu$	4.60 ± 0.21	5.53 ± 0.23
$B^+ \to X l^+ \nu$	10.2 ± 0.9	10.2 ± 0.9
$B^+ \to \bar{D}^0 l^+ \nu$	2.15 ± 0.22	2.15 ± 0.22
$B^+ \to \bar{D}^*(2007) l^+ \nu$	5.3 ± 0.8	6.5 ± 0.5
$B^+ \to \bar{D}_1(2420)^0 l^+ \nu$	0.56 ± 0.16	0.56 ± 0.16
$B^+ \to \bar{D}_2^*(2460)^0 l^+ \nu$	< 0.8	< 0.8
$B^\pm/B^0 \to X e^+ \nu_e$	10.2 ± 0.4	10.70 ± 0.28
$B^\pm/B^0 \to X l^+ \nu_l$	10.38 ± 0.32	10.64 ± 0.23
$B^\pm/B^0 \to \bar{D}^{**} l^+ \nu$	2.7 ± 0.7	2.7 ± 0.7

Comparison of 2002 and 2003 Particle Data Group world averages. † - see Particle Data Group (PDG) 2003 archives at http://pdg.lbl.gov